Gas Hydrate Growth Promotion

Jonathan Verrett

Department of Chemical Engineering, McGill University, Montreal

December 2015

A thesis submitted to McGill University in partial fulfillment of the requirements of the degree of Doctor of Philosophy

People are like clay, moulded by the influence of those around them. No one develops alone

Abstract

A variety of applications have emerged for gas hydrates in industrial processes. However, to implement hydrate technologies, a fundamental understanding of their formation is required. This thesis investigates gas hydrate growth using low-dosage kinetic promoters as well as thermodynamic promoters. Two model surfactants are investigated to study the effect of kinetic promoters. Sodium dodecyl sulphate is used as a model anionic conventional surfactant and DOWFAX 8390 is used as a model anionic gemini surfactant. Results from this study show that surfactants do not significantly affect thermodynamic equilibrium and hydrate former solubility in methane hydrate systems. The promotion effect of both surfactants is studied over a range of concentrations and shows a sigmoid trend. Surfactants are found to significantly increase the gas hydrate former mole fraction during hydrate growth and are estimated to account for half of the increase in growth rate. The remainder of the growth increase is attributed to changes in the hydrate particle area. Thermodynamic promoters are investigated using semi-clathrate systems consisting of tetra-n-butylammonium bromide and water with a guest gas of either carbon dioxide or methane. Equilibrium temperature, pressure and solubility of all components are evaluated for these systems at hydrate-liquid-vapour equilibrium. These data are then used to develop and apply a kinetic model to estimate the intrinsic reaction rate constant of the carbon dioxide semi-clathrate system.

Résumé

Les hydrates de gaz possèdent une grande variété d'applications dans les procédés industriels. Une compréhension de la croissance des hydrates est nécessaire afin de réaliser ces procédés. L'objet de cette thèse est d'examiner l'effet des promoteurs cinétiques et thermodynamiques sur la croissance des hydrates de gaz. L'enquête sur les promoteurs cinétiques se concentre sur deux tensioactifs typiques : le tensioactif conventionnel dodécylsulfate de sodium et le tensioactif gémeaux DOWFAX 8390. Les effets de ces tensioactifs sur les hydrates de méthane sont examinés. Les résultats indiquent que les tensioactifs n'affectent pas l'équilibre thermodynamique ou la solubilité du gaz qui forme l'hydrate. L'observation du taux de croissance des hydrates avec le changement de concentration de tensioactif démontre une tendance sigmoïdale. La présence des tensioactifs augmente la concentration du gaz dans le liquide durant la croissance des cristaux. Cette augmentation de concentration est estimée être responsable pour la moitié de l'augmentation du taux de croissance. Le reste de l'augmentation est attribué aux changements de la superficie des particules d'hydrates. L'étude des promoteurs thermodynamiques se concentre sur l'effet du bromure de tétra-n-butylammonium pendant la formation des hydrates de dioxyde de carbone et de méthane. La température, pression et solubilité de tous les constituants sont mesurées à l'équilibre hydrate-liquide-vapeur. Les données sont ensuite comptabilisées afin de développer un modèle cinétique utilisé pour estimer la constante de vitesse de réaction des semi-clathrates formés avec le dioxyde de carbone.

Acknowledgements

The saying at the start of the start of the thesis is the theme for this acknowledgment section. Indeed, I could write an acknowledgement the size of this work and many times over about those who have shaped my life thus far. They have allowed me to dedicate myself to the work contained in this thesis and, more importantly, develop into what I hope is a compassionate human being.

First I would like to thank my mother and father, June and Robert Verrett. Without their steadfast love, understanding and support I would not have developed into the person I am today. Special thanks go out to my mom for reading and providing critical feedback on all of my works.

I would like to also thank my supervisor Phillip Servio, whose understanding and support over the past five years have been invaluable for the completion of this work. You have given me the space to grow and learn as well as providing guidance and friendship.

I will never forget the experiences with my colleagues who started this journey with me, Jason Ivall, Francis Lang and James Pasieka. as well as my office mate Jean-Sébastien Renault-Crispo. You were all invaluable in providing great conversation, good ideas, and pleasant distractions.

I am also thankful for those that I have supervised in the lab and have taught me so much about research and leadership including Spencer Brennan, Makoto Mitarai, Will Chen, Philippe Assaad and Marion Offenstein.

Like many things at McGill, this thesis wouldn't have been possible without the departmental technical and administrative staff. Lou, Gerry, Lisa, Melanie, Ranjan, Andrew, Louise, Marcia and Emily all made it much more fun to be in the building. I would especially like to thank Jo-Ann Gadbsy for always being happy to see me, even with a bunch of paperwork. Finally, who could forget Frank Caporuscio, thanks for repairing my machines and making time to answer all my questions.

I would like to thank my friends and colleagues outside the scope of the thesis, notably Edwin Ling, Faraz Rajput, Selina Liu and Bradley Marr. You have kept me in great spirits and picked me up when times were rough.

Finally I would like to thank those organizations who funded my thesis including the National Sciences and Engineering Research Council and the donors who gave to the McGill Engineering Doctoral Award fund.

It would not be hard to go on, but I will leave room for the thesis. Needless to say I have been blessed with many great people in my life. You are all the reason I strive so hard to help make a better tomorrow.

Contents

List of Figures

List of Tables

Contributions of Authors

The following is a manuscript-based document containing three published peer-reviewed articles and one article in preparation. The author of this thesis is the primary author for all works contained herein. The author is responsible for the experimental work, data analysis, and writing of all works. Co-author Posteraro trained and provided guidance throughout one of the experimental studies. Co-author Renault-Crispo performed some data collection and was responsible for the modelling included in the published article. The modelling sections from the published article have not been included in the current work and are the primary work of co-author Renault-Crispo. Co-author Servio funded and provided guidance in all the works.

— Verrett, J.; Posteraro, D. and Servio, P., 2012. Surfactant effects on methane solubility and mole fraction during hydrate growth. *Chemical Engineering Science*, **84**: 80-84.

— Verrett, J. and Servio, P., 2012. Evaluating surfactants and their effect on methane mole fraction during hydrate growth. *Industrial and Engineering Chemistry Research*, **51**: 13144-13149.

— Verrett, J.; Renault-Crispo, J.-S. and Servio, P., 2015. Phase equilibria, solubility and modeling study of CO2/CH4+tetra-n-butylammonium bromide aqueous semi-clathrate systems. *Fluid Phase Equilibria*, **388**: 160-168.

— Verrett, J. and Servio, P., 2015. Reaction rate constant of CO2+tetra-n-butylammounium bromide semi-clathrate formation, *private communication.*

Original Contributions

The following is a list of original contributions for the thesis:

— Investigating the effects of anionic surfactants on methane (CH_4) hydrate equilibrium temperature, pressure and hydrate former solubility. Model surfactants used for these studies were sodium dodecyl sulphate as a conventional surfactant and DOWFAX 8390 as a gemini surfactant.

— Profiling the relationship between hydrate growth rate and anionic surfactant concentration.

— Measuring the effect of anionic surfactants on CH_4 mole fraction during hydrate growth and extending the understanding of surfactant promotion mechanisms.

— Determining equilibrium temperature, pressure and liquid phase solubilities of CH_4, carbon dioxide (CO_2) and tetra-n-butylammonium bromide (TBAB) in CO_2—TBAB—H_2O and CH_4—TBAB—H_2O semi-clathrate systems.

— Characterizing the reaction rate constant of the CO_2—TBAB—H_2O system over a two-degree interval from 288 K to 290 K.

Chapter 1

Introduction

Interest is building in the commercial development of technologies involving clathrate hydrates, with the potential to impact many aspects of everyday life. One of the most notable of these is in the field of energy. Energy production and use is crucial to our society today, with a well-established link between energy use and development. Combine this with population growth and concerns over climate change and there is an impetus to move to less carbon-intensive forms of energy. The International Energy Agency predicts that this will be the century of natural gas. As a sign of the times, Ontario, Canada, has recently displaced coal-fired power plants in favour of natural gas, significantly reducing its carbon footprint. Extensive development of fracking has created a new supply of natural gas and upset the oil and gas market. Liquefied natural gas is now becoming the norm for much of Asia.

All of this is relevant to gas hydrates for a number of reasons. First, it is currently estimated that most of all carbon on earth is stored in methane gas hydrates, most of which are found in ocean beds and permafrost regions. This not only has implications for extraction, but also for the climate. Second, with the transport of natural gas by tanker increasing, there is a necessity to store natural gas, for which hydrates offer a unique solution. Finally, hydrates can act as a separation technology to capture and store carbon dioxide or purify water. Crucial to any application

of hydrates is an understanding of gas hydrate formation and growth, which is the focus of this work.

This thesis begins with a background section to provide the reader with a perspective on hydrate development as well as previous research into hydrate growth promotion. Chapters 3 and 4 investigate the effect of low-dosage kinetic promoters on hydrate growth. The first of these chapters investigates the effects of sodium dodecyl sulphate on hydrate thermodynamics and growth. Chapter 4 expands on this first study and looks at the effect of gemini surfactants. Chapters 5 and 6 investigate the effect of thermodynamic promoters on hydrate growth. These chapters focus on a system of recent interest, tetra-n-butylammonium bromide semi-clathrates. Chapter 5 focuses on the thermodynamics and specifically liquid solubilities of hydrate formers in semi-clathrate systems containing methane and carbon dioxide. Chapter 6 then uses this data to investigate and model growth kinetics in the carbon dioxide—tetra-n-butylammonium bromide semi-clathrate system. Chapter 7 offers a comprehensive conclusion to the work and suggests topics for further study. Finally, Chapter 8 provides a reference for all notation used in this study and is followed by a list of cited works.

Chapter 2

Background

2.1 Historical perspective

Clathrates are host-guest substances where the host compound forms a cavity structure to be occupied by the guest compound (Cotton *et al.*, 1976). When the host compound is water, these structures are referred to as clathrate hydrates or simply hydrates (Englezos, 1993). Many of these structures have guest compounds that are gaseous or volatile at atmospheric conditions and thus are also referred to as gas hydrates.

Initial observations of clathrate hydrates are credited to Joseph Priestly (1780) and Humphry Davy (1811) in the late 18th and early 19th century. Following this, hydrates remained solely an academic interest for well over a hundred years after their discovery (Sloan and Koh, 2008). Industrial interest in these compounds began in 1934 when Hammerschmidt published a paper citing their presence in natural gas pipelines. Research quickly began to focus on hydrate prevention, also referred to as flow assurance, and continues to this day (Sloan *et al.*, 2010).

The discovery of naturally occurring gas hydrates was another boon to hydrate research (Makogon, 1965). This sub-field, typically referred to as natural gas hydrates, investigates the location, formation and stability of gas hydrate deposits (Katz, 1971). Ocean beds and permafrost regions are some of the more common areas where such deposits are found, and in recent years there has been a growing number of economically recoverable deposits, as estimated by the United States Geological Survey (Boswell and Collett, 2011).

Much of the interest in hydrates revolves around the energy industry. Clathrates have been investigated as a storage method for natural gas (Gudmundsson *et al.*, 1994; Mimachi *et al.*, 2015). Others have suggested clathrate technologies can be useful in scrubbing carbon dioxide (CO_2) from waste gas streams (Aaron and Tsouris, 2005; Linga *et al.*, 2008). Hydrates have also been investigated as a thermal energy storage medium to provide cooling when electricity rates peak (Clain *et al.*, 2012).

Outside the energy industry, gas hydrates have also found a variety of uses. Due to their guest selectivity, hydrates can function as a gas separation technology (Eslamimanesh *et al.*, 2012). Since they are crystals and seek to exclude impurities, they can be applied to water purification processes such as desalination (Park *et al.*, 2011). Hydrates can also function as a storage and stabilization vehicle for reactive gases such as ozone (Muromachi *et al.*, 2010). With such a variety of applications, gas hydrates have impacted and continue to affect a number of academic and industrial fields.

2.2 Clathrate structure

Clathrate hydrates are nonstoichiometric crystalline compounds formed of water molecules and guest compounds (Jeffrey and McMullan, 2007). The water molecules form a cage structure and interact through hydrogen bonding (Englezos, 1993). This cage structure is not stable unless occupied by a guest compound. The guest interacts with the water molecules forming the cage through weak van der Waals forces (Sloan *et al.*, 2010). Guests, also referred to as hydrate formers, can range from

small gas molecules such as hydrogen or CO_2 to molecules as large as neohexane (Sloan, 2003). Hydrate crystals are composed of roughly of 85% water on a molar basis (Sloan and Koh, 2008). Cavity occupation depends on the thermodynamic conditions of the system (Holder *et al.*, 1980). Three common structures exist for pure clathrate hydrates: structure I (sI), structure II (sII) and structure H (sH).

The sI hydrate structure was confirmed by McMullan and Jeffrey (1965) using X-ray diffraction. These structures have a unit cell composed of 2 small cavities and 6 large cavities in a body-centred cubic structure with 46 water molecules. The small cavities are pentagonal dodecahedrons (5^{12}), a geometric shape with 12 faces of 5 sides. Large cavities consist of tetrakaidecahedrons composed of 12 faces of 5 sides and 2 faces of 6 sides ($5^{12}6^2$). Guest species that form sI cages typically have a small diameter (0.4-0.55 nm) and include methane (CH_4), CO_2 and hydrogen sulphide (Sloan and Koh, 2008). Such hydrates occur naturally and are abundant in permafrost and ocean bed sediments largely due to the presence of biogenic CH_4 (Sloan, 2003).

The sII hydrate structure was confirmed by X-ray diffraction by Mak and McMullan (1965). These structures have a unit cell composed of 16 small and 8 large cavities in a face-centred cubic framework with 136 water molecules. Small cavities are again pentagonal dodecahedrons (5^{12}) and large cavities consist of hexakaidecahedrons composed of 12 faces of 5 sides and 4 faces of 6 sides ($5^{12}6^4$). Guest species that form sII cages are typically in the range of 0.6 to 0.7 nm and include molecules such as propane, nitrogen and tetrahydrofuran (THF) (Sloan and Koh, 2008). sII hydrates are generally not naturally occuring (Sloan, 2003).

A more recently discovered hydrate structure is sH found by Ripmeester *et al.* (1987). They have unit cells made of 3 small and 2 medium cavities with 1 large cavity in a hexagonal framework with 34 water molecules. Small cavities are again pentagonal dodecahedrons (5^{12}). Medium cavities are dodecahedrons with 3 faces of 4 sides, 6 faces of 5 sides and 3 faces of 6 sides ($4^3 5^6 6^3$). Large cavities are icosahedrons composed of 12 faces of 5 sides and 8 faces of 6 sides ($5^{12}6^8$). sH hydrates must contain a mixture of small (0.4-0.55 nm diameter) and large (0.8-0.9 nm diameter) guests in order to be stable and can be found in natural and man-made environments (Sloan and Koh, 2008).

2.3 Phase equilibrium

Hydrates typically form at moderate temperatures either above or below the freezing point of water and pressures ranging from atmospheric to gigaPascals (Englezos, 1993). The conditions under which a clathrate will form are highly dependent on the guest compound in the structure (Sloan and Koh, 2008). A partial phase diagram for a hydrate system with a volatile hydrate former can be found in figure 2.1. Vapour, liquid and solid can coexist depending on system conditions and can include phases formed of a single compound such as ice or a liquefied hydrate former (Mullin, 1997). These additional phases are not shown in figure 2.1, which consists only of vapour-liquid and hydrate-liquid regions for simplicity.

Many systems in the vapour-liquid region are well characterized both experimentally and with models (Sloan and Koh, 2008). Equations of state such as the Peng-Robinson (1976) and Trebble-Bishnoi (1987) can be used to accurately describe thermodynamic properties in this region. Models have also been developed to predict the characteristics of complex fluid mixtures, such as the non-random two-liquid model (NRTL) (Renon and Prausnitz, 1968) or statistical associating fluid theory (SAFT) (Chapman *et al.*, 1989).

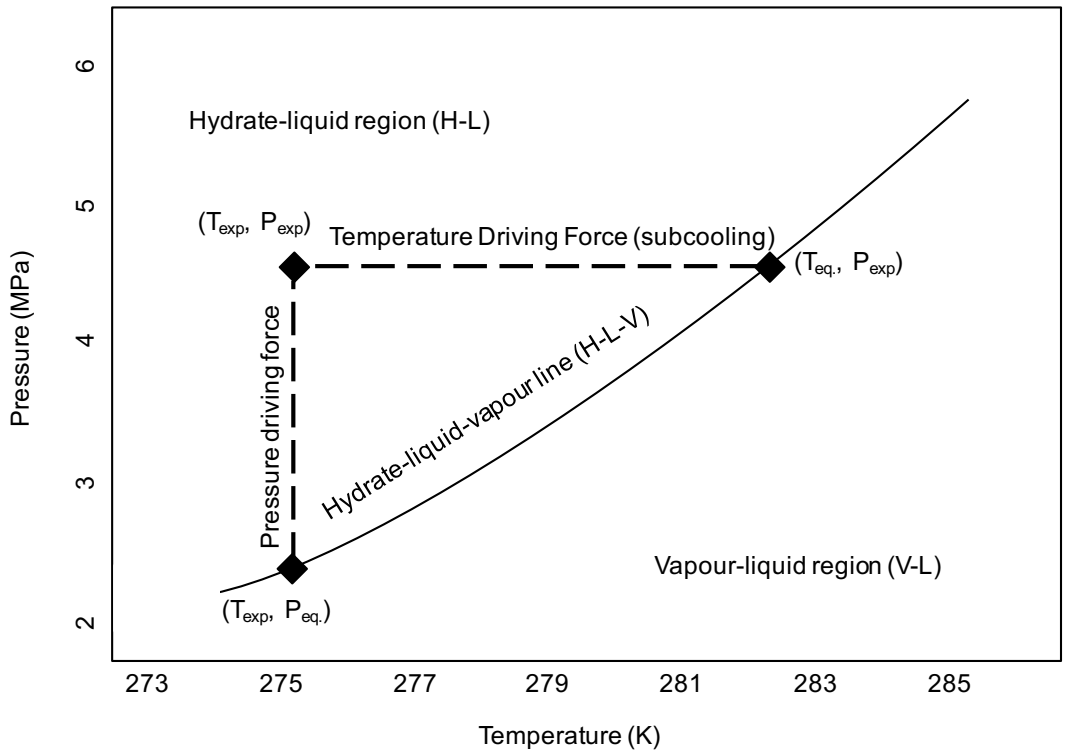

Figure 2.1 – Partial phase diagram for a system with a gaseous hydrate former, in this case a methane-water system

Hydrate phase models generally use a variant of the Van der Waals-Platteeuw model (1959). This model equates the fugacity of water in the hydrate phase to that in the corresponding liquid. It also requires the fugacities of the hydrate formers in order to assess the effect of their integration into the crystal structure.

Studies have recently begun to place a greater emphasis on the solubility of the gas hydrate former in the liquid-hydrate region and along the hydrate-liquid-vapour equilibrium line (Malegaonkar *et al.*, 1997; Servio and Englezos, 2002). Solubility values have been found to have an important influence on model results due to their impact on the calculation of hydrate former fugacity (Renault-Crispo *et al.*, 2014). Accurate solubility values and liquid phase modelling are thus critical to assess the thermodynamics of hydrate formation.

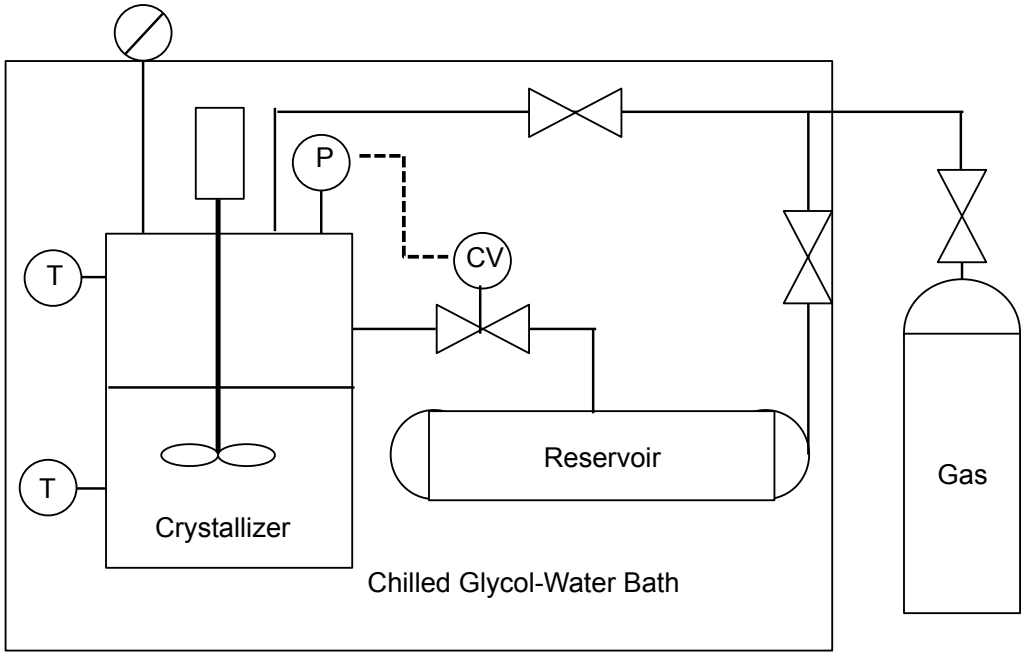

Figure 2.2 – Schematic of a stirred semi-batch crystallizer for studying hydrate formation with pressure transducers (P), temperature probes (T) and a control valve (CV)

2.4 Kinetics

To study hydrate kinetics with a gaseous hydrate former, a vapour-liquid system must be sufficiently chilled and pressurized to bring the system into the hydrate-liquid region (Mullin, 1997). This will elicit the formation of a hydrate phase, which will continue to grow until the system reaches equilibrium, either by consuming all gas, and thus eliminating the vapour phase, or reaching the three-phase vapour-liquid-hydrate equilibrium (Mullin, 1997).

Hydrate growth can be studied in chilled high-pressure crystallizers, with a variety of constructions based on experimental needs (Vysniauskas and Bishnoi, 1983; Heneghan *et al.*, 2001; Yang and Tohidi, 2011). Options include stirred or quiescent systems, windows for visual observation and a variety of sensors for measuring everything from temperature and pressure to cage occupancy and crystal size (Herri *et al.*, 1999; Tulk *et al.*, 2000). Within this work, stirred semi-batch crystallizers such as the one shown in figure 2.2 were used. These systems are kept at a constant temperature using a glycol bath. Pressure is maintained by supplying gas through a control valve with gas consumption measured by calculating the amount of gas supplied by the reservoir. A typical gas consumption curve obtained using one of these setups can be seen in figure 2.3. These curves have three distinct regions: dissolution, induction and growth.

The dissolution region shows the gas dissolving up to the point of saturating the liquid (Mullin, 1997). The liquid is then at the three-phase equilibrium and further dissolution of the hydrate former pushes the system into the hydrate-liquid region. This is followed by the induction period where the system is supersaturated (Sloan and Koh, 2008). In this region the hydrate former continues to dissolve and increases the driving force for the creation of a new phase.

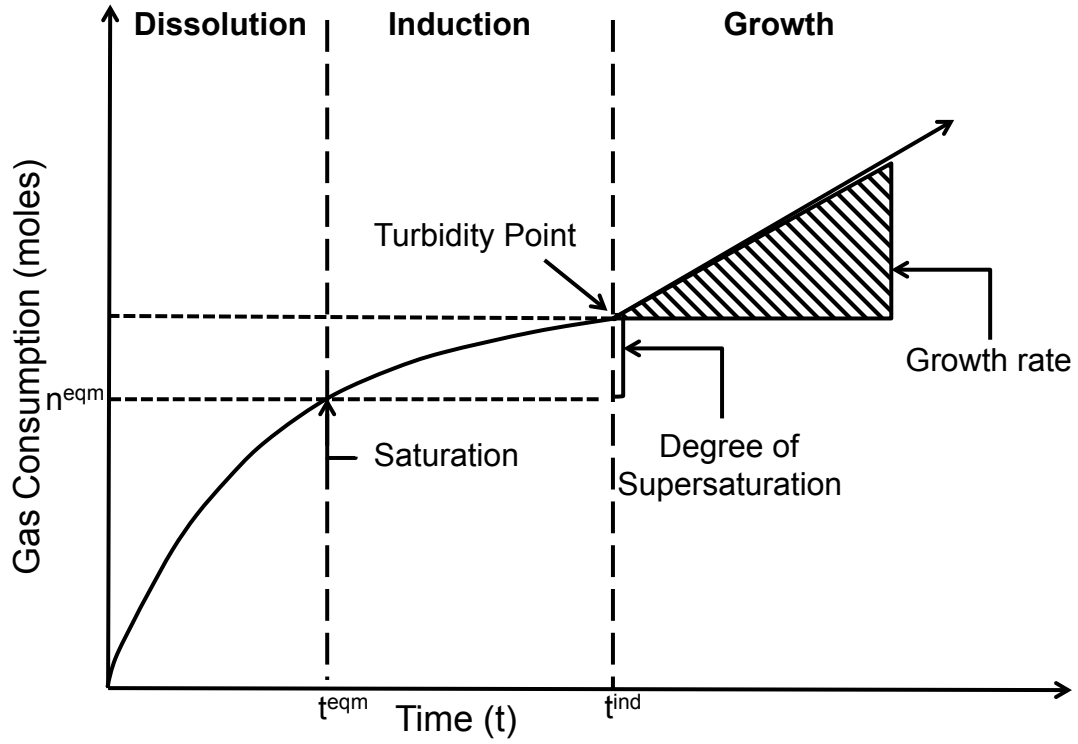

Figure 2.3 – Typical gas consumption curve measured during a hydrate formation experiment

2.4.1 Nucleation

When the system is supersaturated it has the potential to create a new phase (Mullin, 1997). To do this, the energy released by the formation of nuclei of this new phase must be equal to or greater than the energy required to create a new interface (Callister and Rethwisch, 2007). If a nuclei is thought of as a sphere or cube, its surface-to-volume ratio will decrease as it increases in size. Since the volume is proportional to the energy released and the surface is proportional to the energy required, the critical size of nuclei can be determined from equating these energy parameters.

Two types of nucleation are commonly discussed: homogeneous and heterogeneous (Mullin, 1997). Homogeneous nucleation occurs in the bulk of a phase whereas heterogeneous nucleation occurs at sites on a surface in contact with the bulk. This contact can reduce the energy barrier for crystal formation by diminishing the surface area of a new interface (Callister and Rethwisch, 2007). Heterogeneous nucleation is almost exclusively found in macroscopic-scale systems, like those used in this study (Kashchiev and Firoozabadi, 2002). Nucleation is generally thought to occur either on the stainless steel reactor surface or on impurities in the water (Long and Sloan, 1996). One commonly discussed phenomena with hydrate systems is the memory effect (Wilson and Haymet, 2010). Studies have reported a significantly reduced induction time with a liquid sample where hydrates have previously been formed (Makogon, 1974; May *et al.*, 2014). One theory for this occurrence is that the structure of system impurities is modified to conform to the crystal structure. As such, the next time hydrates are formed in the system, they have a template for their crystal structure.

The turbidity point, shown in figure 2.3, indicates the stable formation of a hydrate phase and is generally accompanied by a spike in temperature due to the exothermic nature of crystal growth (Sloan and Koh, 2008).

2.4.2 Growth

Following hydrate formation, gas consumption will increase as hydrate growth occurs in the system. During this time, gas is being transferred from the vapour to the liquid and then correspondingly from the liquid to the hydrate, as shown in figure 2.4 (Herri *et al.*, 1999). This transfer across two interfaces involves four resistances. The vapour-liquid interface (IF^{V-L}) consists of resistances to mass transfer on the vapour side (r_V^{V-L}) as well as on the liquid side (r_L^{V-L}). Performing a scaling analysis shows that the resistance on the vapour side is negligible compared to the resistance on the liquid side (Deen, 1998). The hydrate-liquid interface (IF^{H-L}) consists of resistances to mass transfer on the liquid side (r_L^{H-L}) as well as a re-

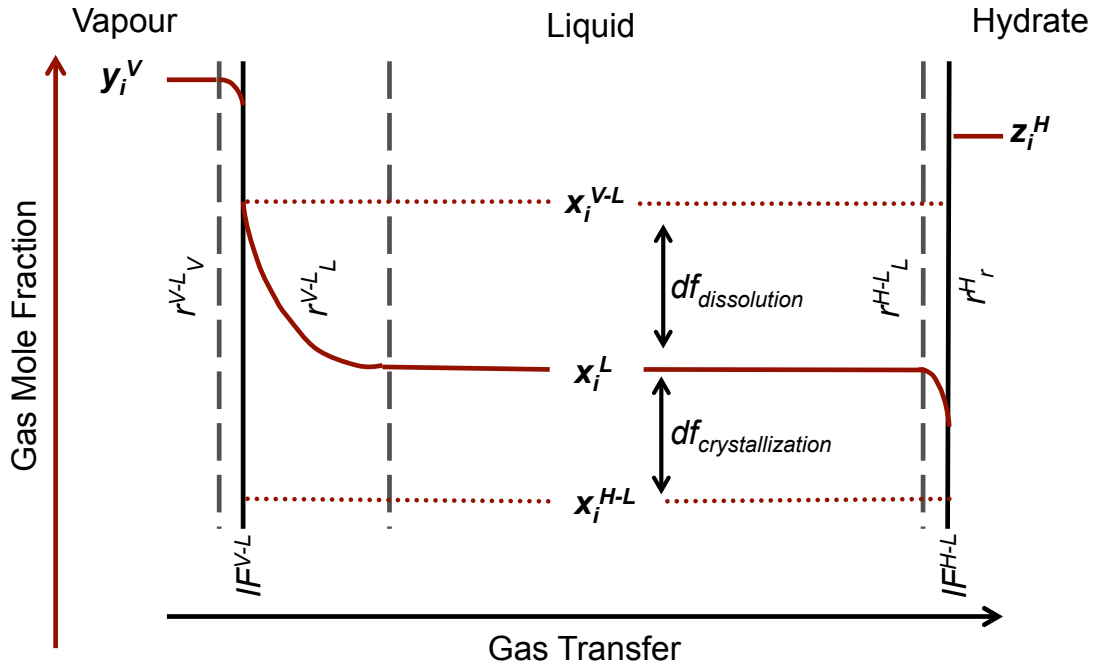

Figure 2.4 – Schematic of gas transfer during hydrate growth

sistance to enclathration, typically denoted as a reaction resistance (r_r^{H-L}). Scaling analysis at the hydrate-liquid interface indicates that the resistance to mass transfer is negligible compared to the reaction resistance for CO_2 (Bergeron and Servio, 2008) and CH_4 systems (Bergeron *et al.*, 2009).

Development of kinetic models to predict hydrate growth originated with the model proposed by Glew and Hagget (1968a; 1968b). Their model was based on the relation between hydrate formation rate and the temperature difference between the reactor and cooling bath. Following this model, a variety of hydrate growth models have been developed (Ribeiro Jr. and Lage, 2008). Driving forces for such models include temperature, fugacity (Englezos *et al.*, 1987b) and concentration (Skovborg and Rasmussen, 1994). Many of these kinetic transfer models attempt to characterize mass transfer across the vapour-liquid interface with notable difficulty. In response, Bergeron and Servio measured the concentration of gas hydrate former

in the liquid bulk and developed a corresponding model (2009).

$$\frac{dn_i}{dt} = \frac{V_L \rho_w}{MW_w} \frac{(x_i^l - x_i^{H-L})}{1/(\pi \mu_2(t) k_r)} \tag{2.1}$$

The model developed, represented by equation 2.1, relates gas consumption ($\frac{dn_i}{dt}$) to a concentration driving force. This driving force is the difference between the bulk liquid mole fraction of the hydrate former (x_i^l) and the hydrate former solubility under hydrate-liquid equilibrium at the experimental temperature and pressure (x_i^{H-L}). The reaction resistance is represented by the term below the driving force and consists of a term for the intrinsic reaction rate, k_r. Particles are assumed to be spherical with particle area represented by the second moment of particle size distribution ($\mu_2(t)$). The equation also includes constants representing the initial liquid volume (V_L), density of water (ρ_w) and molecular weight of water (MW_w). The model has been sucessfully applied to characterize hydrate kinetics for CO_2 (Bergeron and Servio, 2008) and CH_4 systems (Bergeron *et al.*, 2009).

2.5 Additives affecting hydrate formation

A variety of additives can affect gas hydrate thermodynamics and kinetics. These compounds are typically split into the two categories: inhibitors and promoters, with inhibitors suppressing hydrate formation (Kelland, 2006) and promoters enhancing hydrate formation (Eslamimanesh *et al.*, 2012). Inhbitors are further subdivided into thermodynamic, kinetic and anti-agglomerants (Perrin *et al.*, 2013) whereas promoters can be subdivided into thermodynamic and kinetic.

The addition of thermodynamic promoters or inhibitors will significantly influence the chemical energy of a system, generally due to their addition at high mass fractions (Perrin *et al.*, 2013). This is shown by the additives' effect on formation temperature and pressure (Kelland, 2006). A thermodynamic promoter will allow hydrates to form at higher temperatures and lower pressures (Eslamimanesh *et al.*, 2012). THF is one commonly used promoter that will occupy the large cages of an

sII crystal structure (Kang *et al.*, 2001). This leaves the smaller cages to be occupied by molecules such as CO_2 or CH_4 (Zhang and Wu, 2010).

Kinetic promoters or inhibitors are generally added in smaller concentrations than their thermodynamic counterparts and do not function by affecting the chemical energy of the system (Perrin *et al.*, 2013). There are many proposed mechanisms of action for these compounds, generally involving their effects at interfaces (Zhang *et al.*, 2008; Taylor *et al.*, 2007). Many of the kinetic promoters reported are surfactants, with one of the most researched being sodium dodecyl sulphate (SDS) (Karaaslan and Parlaktuna, 2000a; Zhong and Rogers, 2000).

Within these various categories, compounds have been found to act in multiple domains (Mitarai *et al.*, 2015). This multivalence may be due to chemical changes in the system, for example changing a hydrate former, or to changes in system conditions, for example pressure or temperature. Sodium dodecyl sulphate is a notable hydrate promoter with many hydrocarbons such as CH_4, but has a smaller effect on CO_2 clathrate formation. This is thought to be due to the competitive adsorption of carbonate ions at the hydrate surface (Zhang *et al.*, 2010). Surfactants are also known not to micellize below the Krafft temperature, and thus any compound relying on micellization to promote hydrate formation would be ineffective below this temperature (Di Profio *et al.*, 2005).

2.6 Semi-clathrates

Semi-clathrates differ from pure clathrates in that their host structure is not exclusively composed of water molecules (Davidson, 1973). Guest compounds will participate in the cage structure as well as occupy cages. Semi-clathrates can act as thermodynamic promoters and stabilize the crystal structure (Eslamimanesh *et al.*, 2012). There are a variety of compounds that can act in this manner, with some of the most researched being a category of compounds known as quaternary ammonium salts (Park *et al.*, 2013). Within this category, tetra-n-butylammonium bromide (TBAB) has garnered much attention due to its marked effects at stabilizing the

hydrate crystal lattice (Deschamps and Dalmazzone, 2009; Lipkowski *et al.*, 2002). The crystallography of such structures was studied by X-ray even before those of pure clathrates (McMullan and Jeffrey, 1959).

There are a variety of TBAB semi-clathrate structures reported in the literature. Hydrate crystal structures are commonly classified by their hydration number, the number of water molecules per molecule of hydrate former, which in this case is taken to be TBAB (Sloan and Koh, 2008). There are five commonly documented crystal structures of the TBAB semi-clathrate in systems under 60 wt% TBAB, with hydration numbers of 24, 26, 32, 36 and 38 (Shimada *et al.*, 2005; Gaponenko *et al.*, 1984; Lipkowski *et al.*, 2002). These structures will be denoted 1:24, 1:26, 1:32, 1:36 and 1:38 respectively in this report. Studies investigating these structures have found that each are stable at different weight fractions of TBAB (Shimada *et al.*, 2005; Lipkowski *et al.*, 2002).

The structures for 1:36 and 1:38 reported in the literature appear have similar cell parameters and an orthorhombic structure based on X-ray diffraction results (Shimada *et al.*, 2005; Gaponenko *et al.*, 1984). One possibility is that these are the same structure, but reported with slightly different hydration numbers. The report by Gaponenko *et al.* (1984), further suggests that the 1:36 structure with TBAB is isostructural with a 1:38 structure formed with another quaternary ammonium salt. Whether or not these are the same structure, the cages present in the 1:36 unit cell has not been outlined in literature as far as the author is aware. The report by Shimada et al. (2005) outlined the crystal structure for 1:38 with a unit cell of 8 large cages consisting of 4 pentakaidecahedrons and 4 tetrakaidecahedrons as well as 6 small dodecahedral (5^{12}) cages. Two TBAB molecules occupy the 8 large cages with a butyl group in each cage. The bromide and ammonium ions participate in the cage structure by dipole-dipole interactions with surrounding water molecules. This crystal structure is stable with solely TBAB and water; however, small gas molecules such as CH_4 and CO_2 can occupy the 5^{12} cages. This unit cell contains 6 5^{12} cages for every 2 TBAB molecules, meaning it could potentially hold 6 CO_2 molecules (Shimada *et al.*, 2005). This matches well with experimental results measuring CO_2

semi-clathrates with a composition of 2.51 CO_2 molecules per TBAB molecule (Lin *et al.*, 2008), with the discrepancy in results attributed to some of the 5^{12} cages being left unoccupied.

X-ray work by McMullan and Jeffrey (1959) elucidated the structure for 1:32. This structure is further elaborated in the work of Davidson (1973) with a unit cell containing 20 large cages consisting of 4 pentakaidecahedrons and 16 tetrakaidecahedrons as well as 12 small 5^{12} cages. Similar to the 1:38 structure, each TBAB molecule occupies 4 large cages with the ions participating in the cage network. Two of the 12 5^{12} cages are occupied by water molecules with the other 10 left empty. This leads to a theoretical composition of 2 CO_2 molecules per TBAB molecule.

Crystallographic data for 1:24 and 1:26 can be found in the literature (Gaponenko *et al.*, 1984); however, the author could find no description of the cage structure of such compounds. Investigations of the 1:26 structure (Shimada *et al.*, 2005) have likened it to the 1:32 structures reported by Davidson (1973), but there are notable differences in the cell parameters reported by X-ray crystallography (Gaponenko *et al.*, 1984). The large variety of crystal structures reported for TBAB semi-clathrates may lead to confusion about which structures are forming. Since many crystallographic studies focus on semi-clathrates formed of solely TBAB and water, the introduction of guest compounds in the 5^{12} cages can further complicate understanding of the crystal structure. Given the large variety of possible structures, care should be taken when experimenting on TBAB semi-clathrate systems in order to characterize the structures present.

Chapter 3

Surfactant effects on methane solubility and mole fraction during hydrate growth [1]

3.1 Preface

As discussed in chapter 2, clathrate hydrates have a wide variety of applications prompting a need to promote their formation kinetics. Liquid solubility and mole fraction of gas hydrate formers has been recognized as increasingly important in the characterization of gas hydrate systems. With this in mind, the objective of this study was to assess the effect of anionic surfactants on hydrate former solubility and mole fraction. Methane hydrates promoted by sodium dodecyl sulphate were used as a model system.

1. Reproduced in part with permission from Verrett, J., Posteraro, D. and Servio, P., 2012. Surfactant effects on methane solubility and mole fraction during hydrate growth, *Chemical Engineering Science*, **84**: 80-84.

3.2 Abstract

Investigations are still ongoing to discover the mechanism by which surfactants promote hydrate growth. This paper investigates the effects of sodium dodecyl sulphate (SDS), a common surfactant for promoting hydrate growth, on methane solubility and mole fraction in the bulk liquid phase. Hydrates were formed in a stirred 600-cm^3 isobaric/isothermal reactor containing 343 cm^3 of liquid. Bulk solubility experiments under hydrate-liquid, liquid-vapour, and hydrate-liquid-vapour equilibria were performed at temperatures ranging from 275.1 K to 283.3 K and pressures ranging from 3.149 MPa to 6.600 MPa with pure water as well SDS solutions. Kinetic experiments were also performed with water and 360-ppm solutions of SDS at temperatures of 275.1 K, 277.1 K and 279.1 K and pressures of 4.645 MPa, 5.180 MPa and 6.180 MPa respectively. Measurements of the mole fraction of methane in the bulk liquid were taken at 0 s, 225 s and 450 s after hydrate nucleation. Experiments showed SDS has no effect on bulk methane solubility at concentrations that significantly promote hydrate growth. SDS was found to increase methane mole fraction in the bulk liquid during hydrate growth following nucleation. The increase in methane mole fraction is shown to be the major contributor to the increase in hydrate growth rate using the solubility model previously developed by Bergeron and Servio. It is estimated that other factors, such as changes in hydrate particle surface area, may also affect the growth rate and should be investigated further.

3.3 Introduction

Methane can form structure I crystalline gas hydrates when combined with water under suitable thermodynamic conditions (Sloan and Koh, 2008). These structures form naturally in ocean floors and permafrost regions and are estimated to represent an amount of organic carbon larger than all other sources on earth combined (fossil fuel, soil, peat and living organisms) (Suess *et al.*, 1999). Methane hydrates could prove to be very useful in a multitude of industrial applications; one of the most

notable is replacing liquefied natural gas transport in ocean tankers (Gudmundsson and Borrehaug, 1996).

The main challenge to using hydrates in industrial processes is their slow formation rates (Rogers and Zhong, 2000). Studies have shown surfactants, in particular sodium dodecyl sulphate (SDS), have a pronounced effect on hydrate formation (Kalogerakis *et al.*, 1993; Zhong and Rogers, 2000). There is now much interest in understanding and characterizing the mechanism by which surfactants promote hydrate growth (Okutani *et al.*, 2008). This information could help to guide the synthesis or selection of surfactants with properties better suited to promote hydrate growth.

The presence of surfactants in quiescent systems allows porous hydrate layers to form at the vapour-liquid interface instead of a nonporous film (Mel'nikov *et al.*, 1998; Kutergin *et al.*, 1992). This increases hydrate growth by allowing water to be drawn up for hydrate formation rather than blocking gas and water from mixing (Okutani *et al.*, 2008). In stirred systems, it was initially thought that surfactants formed micelles above a certain critical concentration (CMC) and thus increased the solubility of the dissolved guest molecule (Zhong and Rogers, 2000). However, multiple studies have shown that SDS micelles are not present during hydrate formation and cannot form at the temperatures that were tested (Di Profio *et al.*, 2005; Watanabe *et al.*, 2005; Zhang *et al.*, 2007). Studies have also been performed on compounds that can form micelles under hydrate forming conditions and they have been shown to inhibit, or have little effect on, hydrate growth beyond the CMC (Di Profio *et al.*, 2007). Studies have shifted to examining surfactant adsorption onto hydrates and the effects this may have on growth (Del and Kelland, 2009; Zhang *et al.*, 2008). Two of the current theories for hydrate growth promotion include the formation of hydrophobic micro-domains near the hydrate surface that increase methane concentration, or a reduction in adhesion forces among hydrate molecules allowing for a larger particle surface area for hydrate growth (Lo *et al.*, 2010).

Despite knowledge of these mechanisms by which surfactants may promote growth, it is still unclear as to which mechanism is most prominent in stirred systems. Bergeron and Servio recently developed and used a model for hydrate growth in stirred systems that focuses on the liquid phase, found as equation 3.1 (Bergeron and Servio, 2009; Bergeron *et al.*, 2009; Bergeron and Servio, 2008).

$$\frac{dn}{dt} = \frac{V_L \rho_w}{MW_w} \frac{(x_i^l - x_i^{H-L})}{1/(\pi \mu_2 k_r)} \tag{3.1}$$

The driving force for this model is the difference between the mole fraction of the hydrate former in the bulk liquid (x_i^l) and its solubility under hydrate liquid equilibrium (x_i^{H-L}). Apart from this driving force, the model also relies on hydrate particle surface area, represented by the second moment (μ_2), as well as an intrinsic reaction rate constant to predict growth rates of hydrate particles in solution (k_r). This model could effectively describe many predicted mechanisms of hydrate growth promotion, such as an increase in the gas mole fraction in the bulk and/or at the hydrate-liquid interface or a change in solubility, all of which would affect the driving force. The area term could account for increases in hydrate interfacial area due to decreased adhesion forces between particles. Finally, any changes to the reaction mechanism would be represented by the intrinsic reaction kinetics term.

The purpose of this study was to understand whether the bulk solubility of the hydrate former (methane in this case) changes with the addition of surfactants, and to investigate the effect of surfactants on mole fraction of the hydrate former during growth in a semi-batch stirred crystallizer. This will help clarify the main mechanism or mechanisms by which surfactants promote hydrate growth in stirred systems.

3.4 Experimental Apparatus

3.4.1 Experimental setup

A simplified diagram of the experimental setup containing an isothermal/isobaric semi-batch stirred tank crystallizer is shown in figure 3.1. Hydrates are formed in a 316 stainless steel crystallizer with a 20-MPa pressure rating and an internal volume of 600 cm^3. The crystallizer has two polycarbonate windows for visual inspection and is equipped with a MM-D06 magnetic stirrer from Pressure Product Industries. A Baumann 51000 control valve connects the stirrer to the reservoir to supply gas and maintain a constant pressure during hydrate formation. Reservoir and reactor biases are used to increase the accuracy of the pressure readings. To control temperature, the system is immersed in a temperature-controlled 20% ethylene glycol/water bath. Temperature is monitored using general purpose resistance temperature probes from Omega with an accuracy of ±0.1 K. Pressure is monitored using Rosemount pressure transducers configured to a span of 0-14 MPa and differential pressure transducers configured to a span of 0-2 MPa, with an accuracy of ±0.065% of the given span. A National Instruments NI-DAQ 7 data acquisition system coupled with LabVIEW software is used to record all readings. The LabVIEW interface is set up to record the gas reservoir pressure and temperature, and uses the Trebble-Bishnoi equation of state to calculate the number of moles consumed at any given time. All materials are used as received from the suppliers. SDS is obtained from Sigma-Aldrich as a 99% pure A.C.S. reagent grade solid. Methane is obtained from MEGS Inc as 99.99% ultra high purity grade. Deionized water is obtained in house.

3.4.2 Procedure for measuring methane mole fraction during kinetic experiments

A more detailed procedure for solubility measurements during kinetic experiments can be found in a previous paper (Bergeron and Servio, 2009). Prior to injecting a new sample for experimentation, the reactor is washed six times with

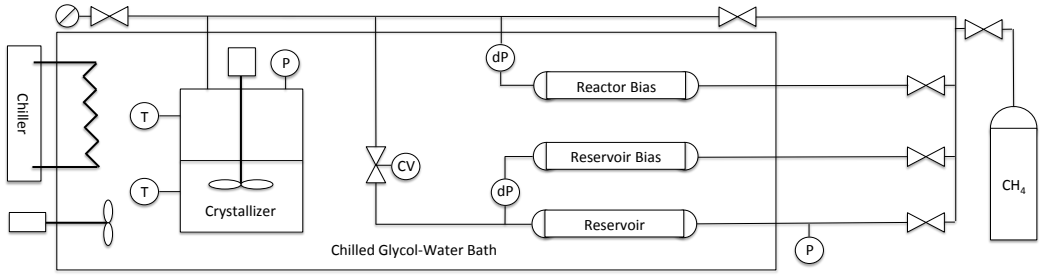

Figure 3.1 – Simplified schematic of the experimental setup

360 cm^3 of deionized water. Following this, 300 cm^3 of the desired solution of either deionized water or SDS is injected into the reactor, accounting for the 43-cm^3 holdup volume of water to get the desired concentration. After sample injection, the reactor gas is purged three times using methane by pressurizing to 1.100 MPa and depressurizing to 0.150 MPa. Once thermal equilibrium is reached at the desired temperature, the crystallizer is pressurized to 1.500 MPa above the three-phase equilibrium pressure (Frost and Deaton, 1946). The reactor temperature is allowed time to stabilize and then the reservoir control valve is set, the data acquisition system switched on, and the stirrer started at 750 rpm. The onset of hydrate growth is characterized by a sudden jump in the reactor liquid temperature. Following this, hydrates are allowed to grow for the desired time (0 s, 225 s or 450 s). Then the measurement system is stopped and the control valve and stirrer are shut off. Measurements of the solubility of the hydrate former are then taken by extracting a bulk liquid sample into a sample bomb. Prior to sample collection the sample bomb is evacuated, weighed and chilled to the experimental temperature. The line used for sampling is fitted with a filter from Norman Filter Company with a 20-nm nominal rating to remove hydrate particles. The final weight of the bomb is measured after sampling. The gas volume in the bomb is then measured by reducing the pressure to atmospheric using a Chandler gasometer. The total amount of methane gas and liquid water in the sample is calculated and this is used to find the solubility of the gas in the liquid (Bergeron and Servio, 2009). The bomb is then cleaned using deionized water. The reactor system is subsequently brought down to 0.600

MPa and sufficient time is given for the hydrates to dissociate. Once all hydrates have dissociated, the reactor is cleaned and the procedure is repeated for the next solution.

3.4.3 Procedure for measuring methane solubility

A detailed procedure for measuring hydrate former solubility can be found in a previous report (Servio and Englezos, 2002). In this study, hydrates were formed in the crystallizer using the procedure in section 3.4.2. Depending on the temperature and pressure combinations, vapour-liquid, hydrate-liquid or hydrate-liquid-vapour equilibrium may be studied. Hydrate-liquid studies require the reactor vapour phase to be displaced by water while maintaining pressure to ensure hydrates remain in the mixture. After reaching the desired conditions, the apparatus is allowed time to equilibrate under stirring. Bulk liquid samples are then extracted and the solubility of the hydrate former is measured as outlined in section 3.4.2. Experiments were performed using a liquid phase initially containing deionized water, 253-ppm or 360-ppm SDS.

3.5 Results and discussion

3.5.1 Effects of surfactants on methane solubility in water

Methane solubility measurements, shown in table 3.1, were performed with deionized water or 253-ppm SDS at various temperature and pressure conditions corresponding to previous experiments performed by Servio and Englezos (2002). Three solubility replicates were collected for each condition tested. The absolute average deviation (A.A.D.) between the three replicates as well as the A.A.D. between the results presented here and those previously reported by Servio and Englezos (2002) were calculated using equation refeq:3.10. Experiments 1 and 2, using only water, have low external A.A.D.s, showing the results from the two studies,

as expected, are identical. Experiments 3 to 5 had relatively low external A.A.D.s, especially considering slight differences in average temperature and pressure. This indicates that methane solubility in water did not increase due to the presence of surfactants at concentrations that promote hydrate growth.

$$A.A.D. = \sum_{i=0}^{n} \frac{\bar{b} - b_i}{q} \tag{3.2}$$

Table 3.1 – Solubility of methane ($x_{CH_4}^{eqm}$) at various temperatures and pressures in deionized water and SDS solutions as compared to the results of Servio and Englezos (2002)

Exp. #	$T^{avg.}$ (K)	$P^{avg.}$ (MPa)	c_{SDS} (ppm)	$x_{CH_4}^{eqm}$ [$\times 10^3$]	A.A.D. w.r.t. reps.	A.A.D. w.r.t. Servio	Phases Present
1	281.5	5.100	0	1.53	1.7	0.13	$L_w - V$
2	283.3	6.600	0	1.73	1.2	0.70	$L_w - V$
3	282.2	6.600	253	1.85	2.3	0.20	$H - L_w - V$
4	280.3	6.600	253	1.64	4.7	4.5	$H - L_w$
5	277.3	5.100	253	1.34	3.9	2.9	$H - L_w$

To further demonstrate this, experiments with water and 360-ppm SDS were also performed at three-phase equilibrium conditions ranging from 275.1 K to 279.1 K. Results from these measurements may be seen in table 3.2. The results again show no difference between methane solubility with or without surfactants. These observations reinforce previous results showing that SDS does not affect hydrate equilibrium conditions (Kalogerakis *et al.*, 1993; Di Profio *et al.*, 2005). This does not discount the hypothesis by Lo *et al.* (2010) that SDS and other surfactants may still concentrate the gas hydrate former near the surface of the hydrate particle in order to promote growth; however, there is no significant effect on the bulk liquid solubility.

Table 3.2 – Solubility of methane ($x_{CH_4}^{H-L-V}$) at various temperatures and pressures under hydrate-liquid-vapour equilibrium in deionized water and SDS solutions

Exp. #	$T^{avg.}$ (K)	$P^{avg.}$ (MPa)	c_{SDS} (ppm)	$x_{CH_4}^{eqm}$ [$\times 10^3$]	A.A.D w.r.t. reps.
6	275.1	3.149	0	1.19	3.2
7	277.1	3.769	0	1.28	3.7
8	279.1	4.660	0	1.52	2.0
9	275.1	3.153	360	1.19	3.2
10	277.1	3.767	360	1.28	2.8
11	279.1	4.670	360	1.52	3.9

3.5.2 Effect of surfactants on hydrate former mole fraction during growth

Hydrate growth rate experiments were performed for both water and 360-ppm SDS solutions at temperatures of 275.1 K, 277.1 K and 279.1 K with pressures at 4.645 MPa, 5.280 MPa and 6.180 MPa respectively. Mole fraction measurements were taken at 0 s (nucleation), 225 s and 450 s and the growth rate was also calculated from the gas consumption using the 450-s run. A sample of a typical growth curve from a 450-s experiment may be found in figure 3.2. The results of the mole fraction measurements may be seen in figure 3.3, with the exact data found in table 3.3. The data indicates that nucleation occurs at a similar mole fraction for both water and SDS solutions at a given temperature, which is to be expected since the addition of surfactants does not affect the system equilibrium. The water solutions tend to stay at roughly the same mole fraction throughout the first 450 s of growth and are consistent with those found previously (Bergeron and Servio, 2009). The mole fraction in SDS solutions is seen to increase between 0 s and 225 s and remains constant between 225 s and 450 s. The increase in mole fraction of the hydrate former may explain the increase in growth rate. The Bergeron and Servio model consists of a driving force which is the difference between the hydrate former mole fraction and solubility. This model can be used to calculate the difference in driving force between the water and SDS systems. Using the solubilities reported

in section 3.5.1, the relative change in driving force (df^{rel}) for the water versus the SDS can be calculated using equation 3.3.

$$df^{rel} = \frac{x^{l}_{CH_4-SDS}(T^{exp}, P^{exp}) - x^{H-L}_{CH_4} - (T^{exp})}{x^{l}_{CH_4-w}(T^{exp}, P^{exp}) - x^{H-L}_{CH_4}(T^{exp})} \tag{3.3}$$

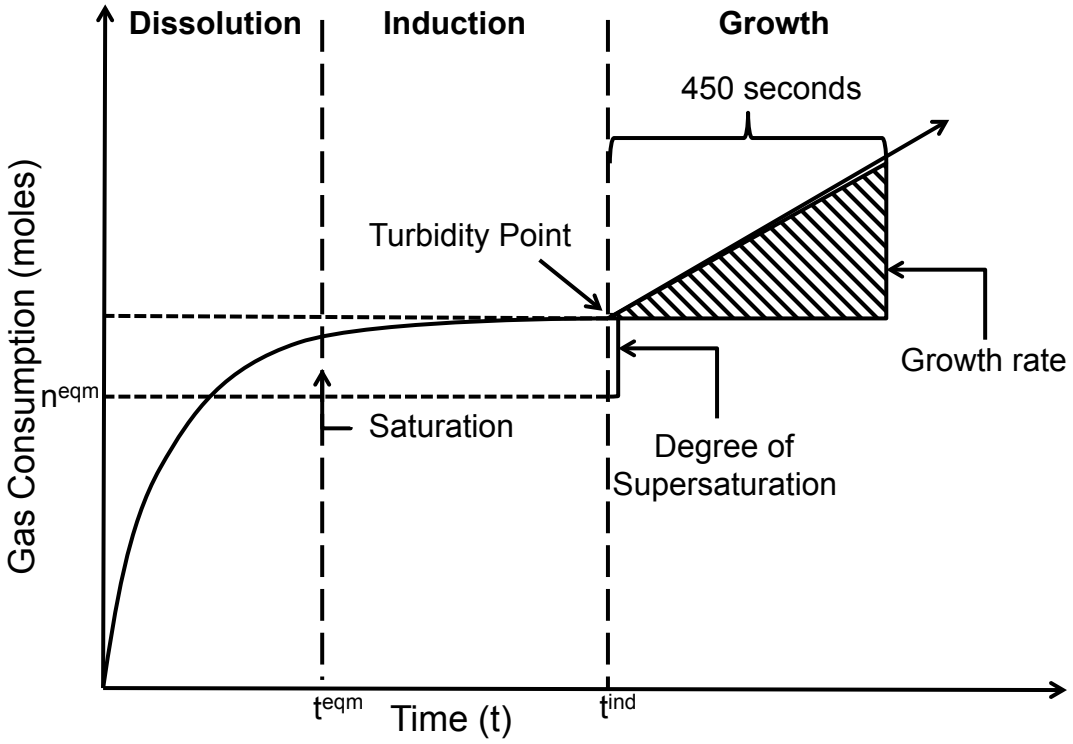

Figure 3.2 – Simplified growth curve of gas consumption during hydrate growth in a stirred crystallizer

The relative driving force has been reported for each temperature in table 3.4. The increase in growth rate (g^{rel}) between water and SDS was calculated with equation 3.4.

$$g^{rel} = \frac{g_w}{g_{SDS}} \tag{3.4}$$

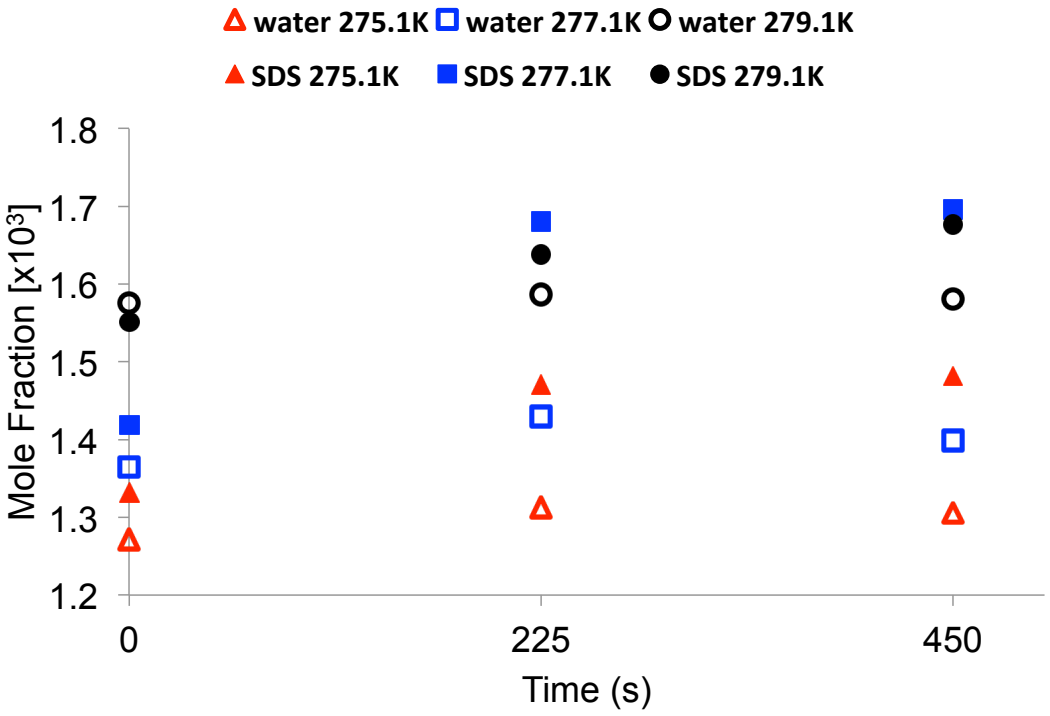

Figure 3.3 – Mole fraction of methane in the bulk liquid taken at various times after the onset of hydrate growth

The growth rates for water and SDS, as well as the relative growth rates, are listed in table 3.4. At 275.1 K, the driving force for hydrate formation in the SDS solution is 2.44 times that of a water solution, while the hydrate growth rate for the SDS solution is 4.69 times that of water. Thus the increase in driving force represents 52% of the increase in growth rate for the SDS solution in comparison to pure water. For the other two temperatures studied, the increase in driving force represents a higher amount of the increase in growth rate. Using the Bergeron and Servio model, the data thus shows that a large part of the increase in growth rate is due to the increase in hydrate former mole fraction. Surfactants could achieve an increase in hydrate former mole fraction by reducing the interphase mass transfer resistance at the vapour-liquid interphase (Watanabe *et al.*, 2005). Previous studies

Table 3.3 – Mole fraction of methane ($x^l_{CH_4}$) in the bulk liquid at various times following hydrate nucleation

T (K)	P (MPa)	c_{SDS} (ppm)	$x^l_{CH_4-0s}$ [$\times 10^3$]	$x^l_{CH_4-225s}$ [$\times 10^3$]	$x^l_{CH_4-450s}$ [$\times 10^3$]
275.1	4.645	0	1.27	1.31	1.31
275.1	4.645	360	1.33	1.47	1.48
277.1	5.280	0	1.36	1.43	1.40
277.1	5.280	360	1.42	1.68	1.70
279.1	6.180	0	1.58	1.59	1.58
279.1	6.180	360	1.55	1.64	1.68

indicate that increased stirring rates achieve higher gas hydrate growth rates by a similar mechanism (Vysniauskas and Bishnoi, 1983). Since the increases in driving force do not fully explain the increases in hydrate growth rate, surfactants should also be acting by other mechanisms. Decreased adhesion forces between hydrate particles or hydrophobic micro-domains at the hydrate-liquid interface are other possible mechanisms that need to be explored further (Lo *et al.*, 2010). Studies with particle size analysis or another method to evaluate the second moment should be performed to explore whether particle adhesion forces play a role in hydrate growth promotion by surfactants.

Table 3.4 – Comparison of average change in driving force (df^{rel}) to average change in hydrate growth rate (g^{rel})

T (K)	P (MPa)	$x^{avg.}_{CH_4-w}$ [$\times 10^3$]	$x^{avg.}_{CH_4-SDS}$ [$\times 10^3$]	df^{rel}	g_w (mol/s) [$\times 10^5$]	g_{SDS} (mol/s) [$\times 10^{-5}$]	g^{rel}
275.1	4.645	1.31	1.48	2.44	1.50	7.04	4.69
277.1	5.280	1.41	1.69	3.11	1.48	5.51	3.73
279.1	6.180	1.58	1.66	2.00	1.10	3.96	2.70

3.6 Conclusion

The effect of SDS on methane solubility and mole fraction during hydrate growth in a isobaric/isothermal stirred crystallizer were measured experimentally. Results from solubility experiments show that SDS has no effect on bulk methane solubility, but does have an effect on the methane mole fraction in the bulk liquid during hydrate growth. The increase in hydrate growth rate, measured through gas consumption, was then compared to the increase in driving force for hydrate formation using the Bergeron and Servio model. This comparison showed that a significant amount of the increase in hydrate growth rate can be explained by the increase in driving force. Further studies are required to investigate whether other promotion mechanisms, such as a reduction in adhesion forces between hydrate particles, are affecting hydrate growth.

3.7 Acknowledgements

The authors are grateful to the Natural Sciences and Engineering Research Council of Canada (NSERC), McGill University, le Fonds Québécois de la Recherche sur la Nature et les Technologies (FQRNT), the Canada Research Chair Program (CRC) and the Eugene Ulmer Lamothe Fund (EUL) in the McGill Department of Chemical Engineering for funding and support.

Chapter 4

Experimental insights into hydrate growth promotion by surfactants: a model to evaluate surfactants [1]

4.1 Preface

Chapter 3 showed that low-dosage promoters such as surfactants do not affect hydrate former solubility but can have a significant influence on mole fraction during hydrate growth. To broaden the understanding of the effect of surfactants on hydrate growth, our next study focused on the effect of surfactant concentration. The study was also expanded to include gemini surfactants to test their effectiveness promoting hydrate growth as compared to conventional surfactants. Attempts were initially made to synthesize a gemini surfactant, but low yields and purification challenges led to the use of the commercial surfactant DOWFAX 8390.

1. Reproduced in part with permission from Verrett, J. and Servio, P., 2012. Evaluating surfactants and their effect on methane mole fraction during hydrate growth, *Industrial and Engineering Chemistry Research*, **51**: 13144-13149.

4.2 Abstract

Little work has been done to characterize the effects of surfactant concentration on hydrate growth. The focus of this study is to investigate the effects of gemini and conventional surfactants on hydrate growth and evaluate growth promotion of a variety of surfactants in a consistent manner. The effects of sodium dodecyl sulphate (SDS) and DOWFAX 8390 surfactants on methane hydrates formed in a stirred 600-cm^3 reactor containing 343 cm^3 of liquid were investigated. Solubility experiments under hydrate-liquid-vapour equilibria were conducted at 275.1 K with pure water and solutions of each surfactant. Kinetic experiments were performed at 275.1 K and 4.645 MPa with surfactant concentrations ranging from 0 to 1150 ppm for SDS and 0 to 200 ppm for DOWFAX 8390. Methane mole fraction measurements were taken at various times throughout the kinetic experiments. Both surfactants were found to have no effect on methane solubility in a hydrate-liquid-vapour system at equilibrium. The surfactants did, however, have a pronounced effect on bulk methane mole fraction during kinetic experiments at surfactant concentrations that significantly promoted hydrate growth. The average hydrate growth rate was measured at various surfactant concentrations and a sigmoid trend was observed for both surfactants. The data showed a smooth, rather than instantaneous, increase in growth rate. A mathematical model is proposed and applied to compare the effectiveness of both surfactants at promoting hydrate growth. DOWFAX 8390 and SDS solutions both promote growth more than 4.5 times that of water samples, but DOWFAX 8390 achieves this promotion at 1/4 the concentration of SDS and has a larger increase in promotion per unit mass of surfactant added. The role of surfactants at the hydrate-liquid and vapour-liquid interfaces are discussed.

4.3 Introduction

Gas hydrates are formed when a suitable guest molecule is enclosed in a network of water molecules held together through hydrogen bonding. Hydrates are crystalline solids where the guest molecule stabilizes the water lattice structure through weak van der Waals forces (Sloan and Koh, 2008). There are many potential applications for these compounds such as liquefied natural gas transport, gas separation and water desalination, to name a few (Gudmundsson and Borrehaug, 1996).

Interest was sparked in hydrate growth promotion using surfactants in 1993 when Kalogerakis *et. al.* found that certain surfactants would promote hydrate growth. Subsequently in 2000, Zhong and Rogers added 242 ppm of SDS to a quiescent hydrate system and noted an increase in hydrate growth by over 700 times compared to pure water. Karaaslan and Parlaktuna (2000a) tested anionic, cationic and nonionic surfactants in a stirred system and found that anionic surfactants were the best promoters. Further studies also indicated that anionic surfactants exhibit faster hydrate growth rates compared to nonionics or cationics; however, results vary based on surfactant structure (Sun *et al.*, 2003; Karaaslan and Parlaktuna, 2000b). Surfactants have also been found to increase gas storage capacity, within a specified timeframe, by converting more of the available water within a sample into hydrates (Sun *et al.*, 2003).

Recently there has been much interest in the application of gemini surfactants (Sekhon, 2004; Fisicaro *et al.*, 1997; Tyagi and Tyagi, 2009). These surfactants contain two (or more) single-chain surfactant structures attached near the hydrophilic end (Tyagi and Tyagi, 2009). One of their many interesting properties is that their critical micelle concentrations are one or two orders of magnitude lower than conventional surfactants (Zana and Xia, 2004). These compounds have been found to increase the rate of hydrate growth in a stirred reactor, but not to the same extent as SDS (Kwon *et al.*, 2011).

Though there is an abundance of data on surfactant promotion, very little is known about the mechanism by which surfactants promote hydrate growth. It has

been observed that the presence of surfactants in quiescent systems allows porous hydrate layers to form at the vapour-liquid interface rather than a nonporous film (Mel'nikov *et al.*, 1998; Kutergin *et al.*, 1992). This permits water to be drawn up for hydrate formation rather than blocking gas and water from mixing (Okutani *et al.*, 2008). It was also thought that surfactants would form micelles above a certain critical concentration and thus increase the solubility of the dissolved guest molecule (Zhong and Rogers, 2000). However, multiple studies have shown that SDS micelles are not present during hydrate formation and cannot form at the temperatures that were tested (Di Profio *et al.*, 2005; Watanabe *et al.*, 2005; Zhang *et al.*, 2007). Studies have also been performed on compounds that can form micelles under hydrate forming conditions and these compounds have been shown to inhibit or have no effect on hydrate growth when micelles are formed (Di Profio *et al.*, 2007). Interest has recently turned to examining surfactant adsorption onto hydrates and the effects this may have on growth (Del and Kelland, 2009; Zhang *et al.*, 2008). Two of the current theories for hydrate growth promotion include the formation of hydrophobic micro-domains near the hydrate surface that increase methane concentration, or a reduction in adhesion forces among hydrate molecules allowing for a larger particle surface area for hydrate growth (Lo *et al.*, 2010).

Despite knowledge of these mechanisms by which surfactants may promote growth, it is still unclear as to which mechanism is most prominent in stirred and unstirred systems. Bergeron and Servio recently developed and used a model for hydrate growth in stirred systems focusing on the liquid phase. This model eliminates the need to approximate the resistance at the vapour-liquid interface and can be described by Equation 4.1 (Bergeron and Servio, 2009).

$$\frac{dn}{dt} = \frac{V_L \rho_w}{MW_w} \frac{(x_i^l - x_i^{H-L})}{1/(\pi \mu_2 k_r)} \tag{4.1}$$

The driving force for this model is the difference between the mole fraction of the hydrate former in the bulk liquid (x_i^l) and its solubility under hydrate-liquid equilibrium (x_i^{H-L}) (Bergeron *et al.*, 2009; Bergeron and Servio, 2008). Apart from

this driving force, the model also relies on hydrate particle surface area, represented by the second moment (μ_2), as well as an intrinsic reaction rate constant (k_r) to predict growth rates of hydrate particles in solution. This model could effectively encapsulate many mechanisms of hydrate growth promotion, most notably an increase in mole fraction in the bulk, x_i^l (the driving force), or an increase in hydrate interfacial area, μ_2, due to decreased adhesion forces between particles. With these factors in mind, the purpose of the current study was threefold: (1) Measure to what extent surfactants affect the equilibrium solubility and bulk mole fraction of the hydrate former (2) Investigate the mechanism by which surfactants promote hydrate growth in a stirred system and (3) Compare the effects of gemini and conventional surfactants on hydrate growth.

4.4 Experimental apparatus

4.4.1 Experimental setup

A simplified diagram of the experimental setup containing an isothermal/isobaric semi-batch stirred tank crystallizer is shown in figure 4.1. Hydrates are formed in a 316 stainless steel crystallizer with a 20-MPa pressure rating and an internal volume of 600 cm^3. The crystallizer has two polycarbonate windows for visual inspection and is equipped with a MM-D06 magnetic stirrer from Pressure Product Industries. A Baumann 51000 control valve connects the stirrer to the reservoir to supply gas and maintain a constant pressure during hydrate formation. Reservoir and reactor biases are used to increase the accuracy of the pressure readings. To control temperature, the system is immersed in a temperature controlled 20% ethylene glycol/water bath. Temperature is monitored using general purpose resistance temperature probes from Omega with an accuracy of ±0.1 K. Pressure is monitored using Rosemount pressure transducers configured to a span of 0-14 MPa and differential pressure transducers configured to a span of 0-2 MPa, with an accuracy of ±0.065% of the given span. A National Instruments NI-DAQ 7 data acquisition system coupled with LabVIEW

software is used to record all readings. The LabVIEW interface is set up to record the gas reservoir pressure and temperature, and uses the Trebble-Bishnoi equation of state to calculate the number of moles consumed at any given time.

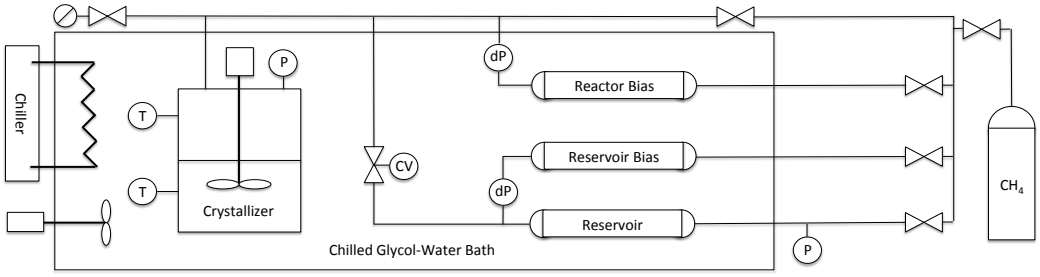

Figure 4.1 – Simplified schematic of the experimental setup

4.4.2 Materials

All materials are used as received from the suppliers. SDS is obtained from Sigma-Aldrich as a 99% pure A.C.S. reagent grade solid. DOWFAX 8390 (DOWFAX) is obtained from Dow Chemicals in a solution containing 35.6% active ingredients, 0.6% sodium sulphate and 0.1% sodium chloride with the remainder as water. The active ingredients are a mixture consisting of roughly 75% disodium hexadecyldiphenyloxide disulfonate (monoalkyl disulfonate surfactant) and 25% disodium dihexadecyldiphenyloxide disulfonate (gemini surfactant). The structures of these molecules are found in figure 4.2. Methane is obtained from MEGS Inc. as 99.99% ultra high purity grade. Deionized water is obtained in house.

4.4.3 Procedure for kinetic experiments

Prior to injecting a new sample for experimentation, the reactor is washed six times with 360 cm^3 of deionized water. A 300-cm^3 quantity of the desired solution of either deionized water, SDS or DOWFAX is then injected into the reactor, accounting for the 43-cm^3 holdup volume of water to get the desired concentration.

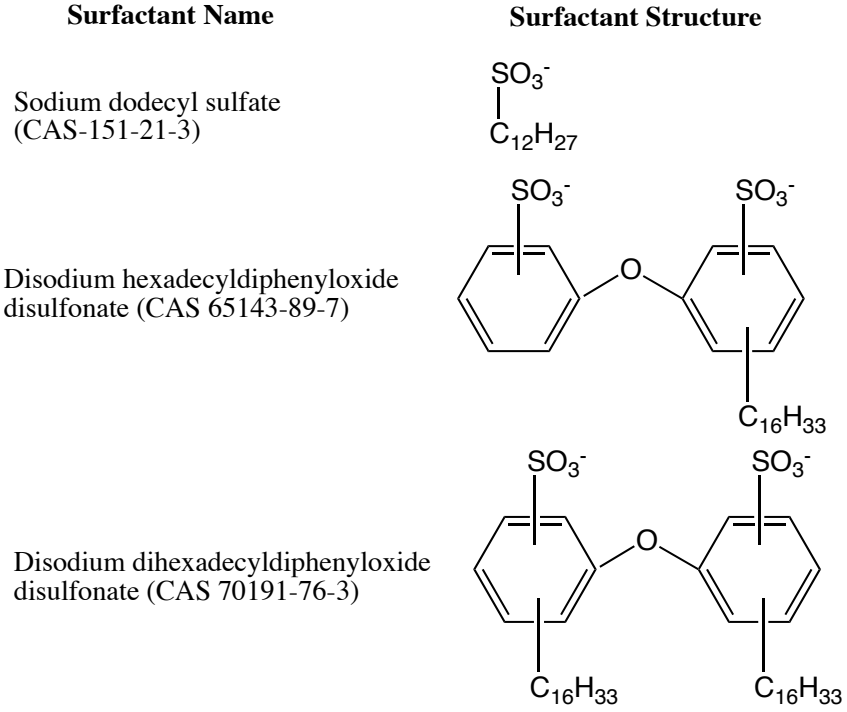

Figure 4.2 – Structures of each of the surfactants used in the experiments

Following sample injection, the reactor is then purged three times using methane by pressurizing to 1.100 MPa and then depressurizing to 0.150 MPa. Once thermal equilibrium is reached at 275.1 K, the crystallizer is pressurized to 1.500 MPa above the three-phase equilibrium pressure of 3.145 MPa at 275.1 K (Frost and Deaton, 1946). When the temperature is stabilized in the crystallizer and reservoir, the control valve is set, the data acquisition system switched on and the stirrer started at 750 rpm. The onset of hydrate growth is characterized by a sudden jump in the reactor liquid temperature. Following this, hydrates are allowed to grow for 450 s and then the measurement is stopped and the control valve is shut off. The system is subsequently brought down to 0.600 MPa and sufficient time is given for the hydrates to dissociate. Once all hydrates have dissociated, a second run with the same sample is performed by repressurizing the reactor and repeating the procedure.

4.4.4 Procedure for measuring methane solubility and mole fraction

A detailed procedure for measuring hydrate former solubility can be found in a previous report (Servio and Englezos, 2002). Briefly, hydrates are formed at 275.1 K with the desired solution using the kinetic experiment procedure. Once hydrates are formed, the mixture is depressurized to near equilibrium pressure (3.145 MPa) and left for sufficient time until pressure stabilizes. Measurements of the solubility of the hydrate former are then taken by turning off the stirrer and extracting a bulk liquid sample into a sample bomb. The sample bomb is evacuated and chilled to the desired temperature prior to the experiment and weighed both before and after the sample is collected.The sample is taken through a line with a filter, with a nominal rating of 20 nm, to remove any entrained hydrate particles. The gas content in the bomb is measured by reducing the pressure to atmospheric using a Chandler gasometer. The total amount of methane gas in the sample is then calculated and this is used to find the solubility of the gas in the liquid. Experiments were first done using deionized water to ensure consistency with previous results (Servio and Englezos, 2002).

Mole fraction measurements are taken at 0 s, 225 s, and 450 s during kinetic experiments. The procedure from the kinetic experiments is used to form hydrates and they are allowed to grow for the desired time. The stirrer is then stopped, control valve shut off and a liquid sample is taken using a sample bomb. The same procedure for sampling gas content during solubility measurements is used for mole fraction measurements.

4.5 Results and Discussion

4.5.1 Effect of surfactant concentration on hydrate growth rate

Hydrate growth rate experiments were performed for a variety of concentrations of SDS and DOWFAX at 275.1 K with a driving force of 1.500 MPa above the three-phase equilibrium pressure of 3.145 MPa (Frost and Deaton, 1946). As shown in the general growth curve in figure 4.3, the growth rate was then calculated from the gas consumption in the first 450 s in the growth region. The overall growth rate at a given surfactant concentration was taken as the average of the growth rates from two separate runs at that concentration. The average growth rates, along with 95% confidence intervals, and the water growth rate baseline were then plotted against surfactant concentration and can be found in figure 4.4. Previous studies have suggested that the hydrate growth rate will suddenly increase at a specific surfactant concentration (Zhong and Rogers, 2000; Watanabe *et al.*, 2005). As shown by the growth rate curve, though the increase in growth rate can be drastic, it is not an instantaneous jump but a continuous increase over a concentration range. The data for SDS show that the surfactant begins to have a significant effect on the hydrate growth rate above 150 ppm and reaches a maximum of 70.4 μmol/s at 575 ppm. DOWFAX has a significant effect on the hydrate growth rate at under 10 ppm, with a maximum growth rate of 59.6 μmol/s at 200 ppm. The trend for both compounds show that there is an appreciable concentration range over which hydrate growth rate increases with surfactant concentration. The promotion effect of both compounds is similar, with DOWFAX having a slightly lower maximum and promoting over a lower concentration range. The DOWFAX mixture contains gemini surfactants, which are known to have similar properties to conventional surfactants at lower concentrations, and this trend appears to hold in this case (Zana and Xia, 2004).

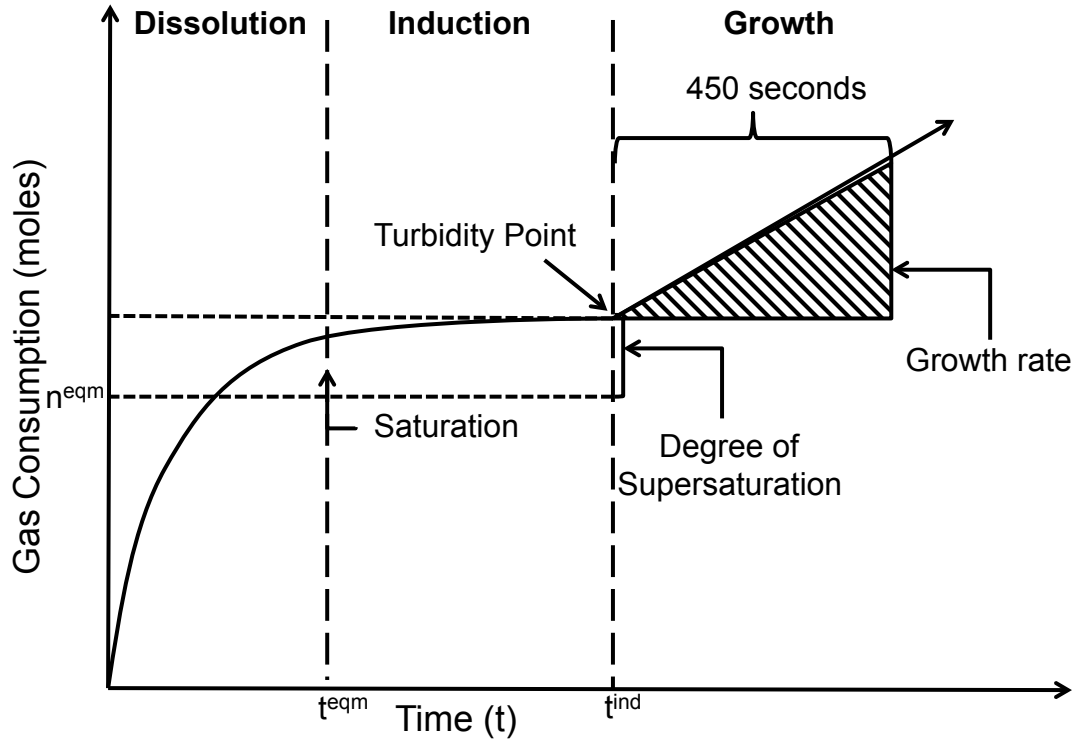

Figure 4.3 – Simplified growth curve of gas consumption during hydrate growth in a stirred crystallizer

4.5.2 Methane solubility and mole fraction measurements

Methane solubility measurements, shown in table 4.1, were performed under hydrate-liquid-vapour equilibrium at 275.1 K and 3.145 MPa. Pure water, as well as surfactant solutions of 575-ppm SDS and 200-ppm DOWFAX were used because they maximized growth promotion. The solubility values shown are the average of three replicates. As found in previous reports, methane solubility does not change with the addition of surfactants at these low concentrations, and was constant at roughly 1.19 mmol methane per mol water (Verrett *et al.*, 2012).

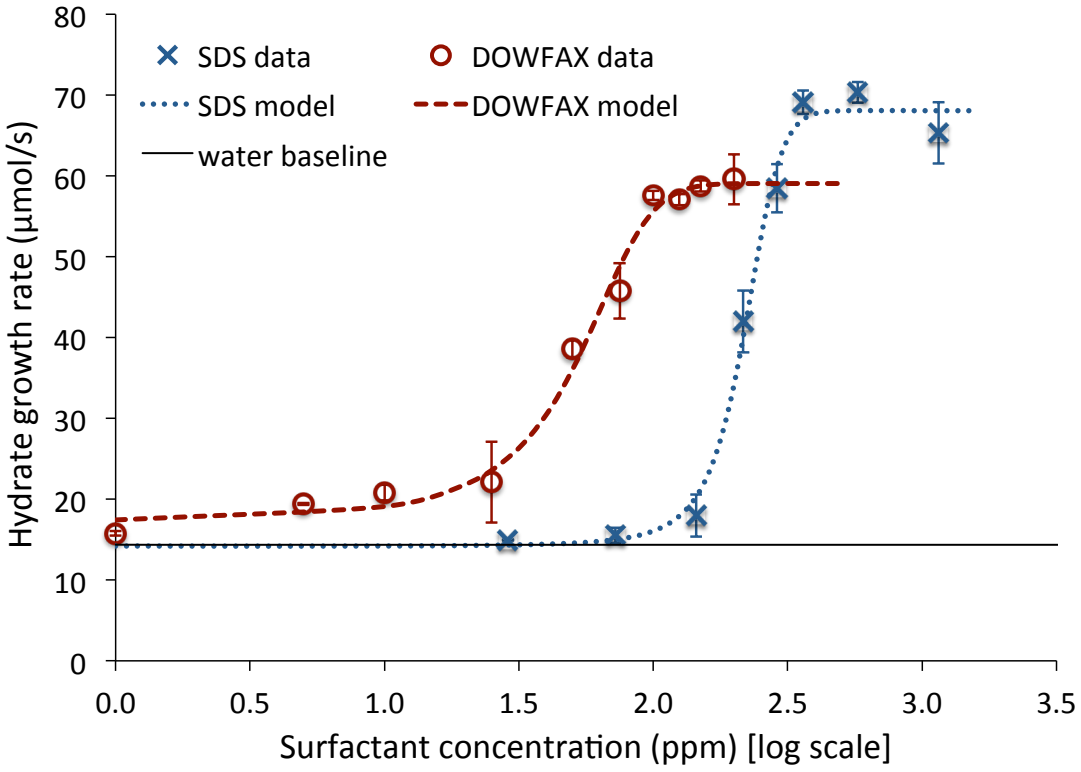

Figure 4.4 – Hydrate growth rate at various surfactant concentrations with 95% confidence intervals and the fitted mathematical model

Mole fraction measurements were performed with solutions of water, 575-ppm SDS and 200-ppm DOWFAX at 275.1 K and 4.645 MPa. Measurements were taken at 0 s (nucleation), 225 s and 450 s. The results of the mole fraction measurements may be found in figure 4.5. At nucleation, all solutions have a mole fraction that is lower than the measurements taken at later times. The mole fraction measurements at 225 s and 450 s appear to be the same for all solutions tested, indicating a constant mole fraction following nucleation. A constant mole fraction has also has been observed in previous studies (Bergeron and Servio, 2009; Verrett *et al.*, 2012). The Bergeron and Servio model can be used to calculate the change in driving force between the water system and the surfactant systems. The relative change in driving

Table 4.1 – Comparison of average change in driving force (df^{rel}) to average change in hydrate growth rate (g^{rel})

Solution	$x^{sol}_{CH_4}$ [$\times 10^{-3}$]	$x^{l-avg}_{CH_4}$ [$\times 10^{-3}$]	df^{rel}	g (μmol/s)	g^{rel}
pure water	1.19	1.31	1.00	14.4	1.00
575 ppm SDS	1.19	1.48	2.44	70.4	4.89
200 ppm DOWFAX	1.20	1.47	2.38	59.6	4.14

force (df^{rel}) for any solution in comparison to pure water can be calculated using equation 4.2.

$$df^{rel} = \frac{x^{l}_{CH_4-s}(T^{exp}, P^{exp}) - x^{H-L}_{CH_4}(T^{exp})}{x^{l}_{CH_4-w}(T^{exp}, P^{exp}) - x^{H-L}_{CH_4}(T^{exp})} \tag{4.2}$$

The relative driving force has been reported for each solution in table 4.1. Using the growth rate measurements at these conditions, the relative growth rate (g^{rel}) between water and each solution was calculated with equation 3.4.

$$g^{rel} = \frac{g_s}{g_w} \tag{4.3}$$

The growth rates and relative growth rates calculated are listed in table 4.1. The driving forces for hydrate growth with both SDS and DOWFAX solutions are roughly 2.4 times higher than the driving force for hydrate formation in water. The increase in driving force represents roughly 50% of the increase in growth rate for the surfactants. Since both surfactants have very similar values, it is likely that they promote by the same mechanisms. One theory to explain these results is that the surfactants decrease the resistance at the vapour-liquid interface, leading to a higher methane mole fraction during growth. Figure 4.6 shows this effect surfactants have on the bulk methane concentration and driving force. This is similar to what has been observed previously with higher hydrate growth rates as stirring is increased (Vysniauskas and Bishnoi, 1983). Given that the driving force accounts for only

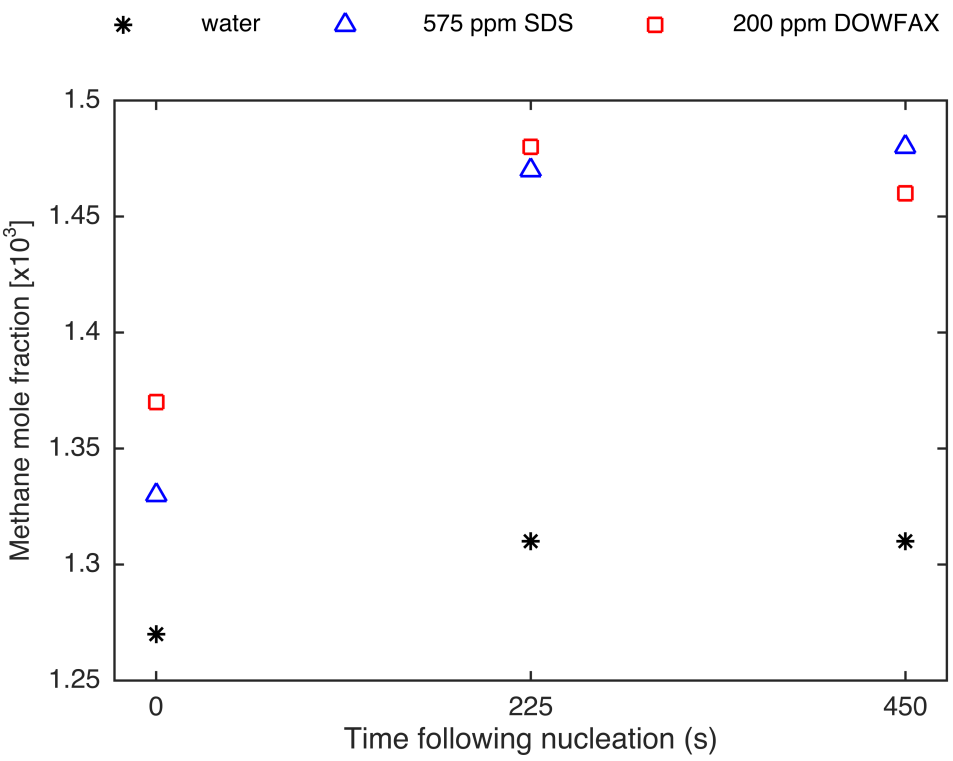

Figure 4.5 – Mole fraction of methane in the bulk liquid taken at various times after the onset of hydrate growth at 275.1 K and 4.645 MPa

half of the increases in hydrate growth, surfactants must be affecting growth by multiple mechanisms. Studies on hydrate formation in unstirred systems have shown that the presence of hydrates can cause significant morphological changes to crystal structure (Mel'nikov *et al.*, 1998; Kutergin *et al.*, 1992). Based on these results, changes in the second moment, perhaps by adsorption of surfactants at the hydrate-liquid interface, are another possible mechanism of hydrate promotion (Lo *et al.*, 2010). Further investigation using particle size analysis will be needed to evaluate the second moment. Interestingly both these mechanisms involve surfactants at interfaces. Understanding surfactant interactions at these interfaces may be the key to finding better hydrate growth promoters.

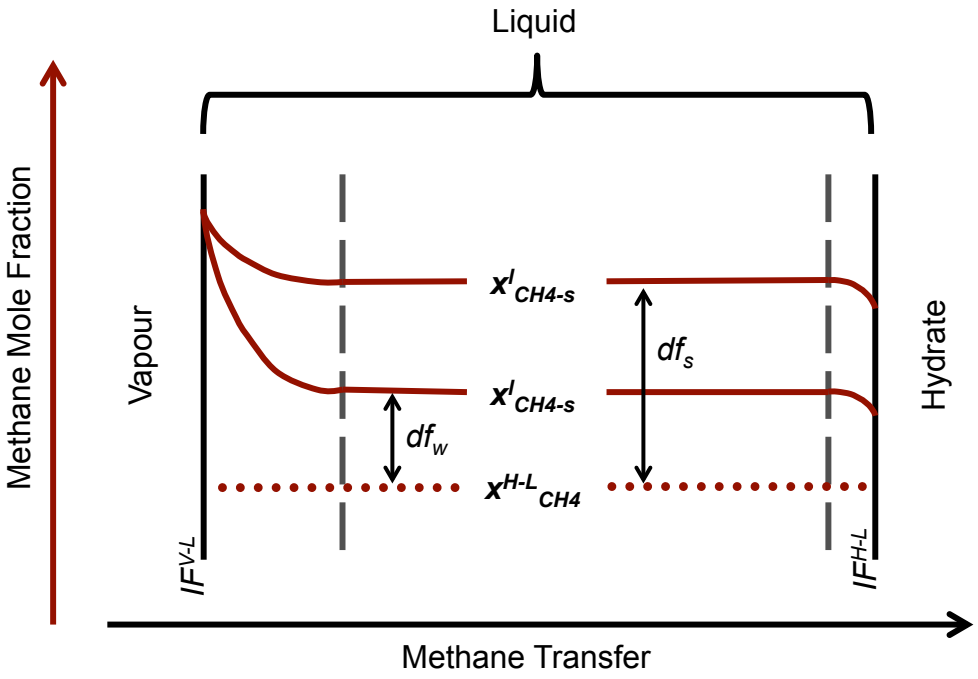

Figure 4.6 – Diagram showing the methane mole fraction profile in the liquid phase where $x^{H-L}_{CH_4}$ is the solubility at equilibrium, $x^{l}_{CH_4-w}$ is the mole fraction with pure water and $x^{l}_{CH_4-s}$ is the mole fraction with surfactants present

4.5.3 Evaluating surfactants

Both growth plots show a sigmoid type structure, starting with no promotion at low concentrations, increasing to higher promotion over a relatively small concentration range, and then stagnating again. The SDS data show a drop in promotion beyond its maximum that is consistent with results from a previous study (Karaaslan and Parlaktuna, 2000b). This sigmoid curve shape may be common for surfactant promotion and can be split into three main regions as shown in 4.7. Within the first region there is not enough surfactant in the solution to affect the interfaces. In the second region, which we will call the growth promotion region, enough surfactant is

present to significantly affect both the hydrate-liquid and vapour-liquid interfaces. In the third region, the interfaces become saturated with surfactants, and thus there is no further increase in hydrate growth rate.

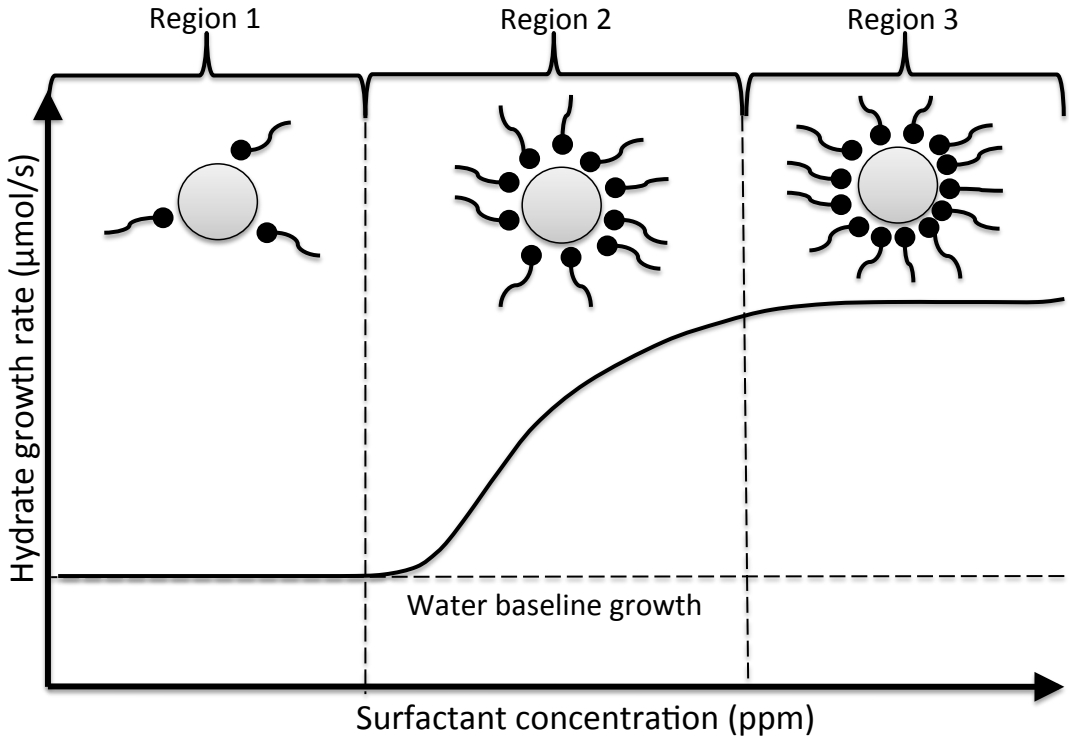

Figure 4.7 – Schematic of surfactant interactions at the hydrate-liquid interface and their effects on growth rate

It is our hypothesis that the sigmoid curve shape is common when plotting growth rate against surfactant concentration. We propose that a standard model, with physically relevant parameters, be used to fit the data and compare surfactant performance for hydrate promotion. A simple sigmoid curve, seen as equation 4.4, can be used for this purpose.

$$\frac{dn}{dt} = g_0 + \Delta g/(1 + exp[-\frac{c - c_{50}}{s}]) \tag{4.4}$$

where $\frac{dn}{dt}$ is the growth rate, g_0 is the initial growth rate without surfactant, Δg is the maximum increase in growth rate, c is the surfactant concentration, and c_{50} is the concentration such that growth has increased by half of Δg. s represents the surfactant effectiveness and is inversely related to the slope of the curve; a smaller s value indicates a smaller change in surfactant concentration is required to increase the growth rate. All model parameters were fitted using the non-linear regression function in MATLAB. Parameter values for each surfactant may be found in table 4.2. Because DOWFAX promoted at extremely low concentration, the g_0 value was assigned to be the growth rate of hydrates in pure water rather than leaving it as a fitted parameter. Both curves may be seen with the experimental data in figure 4.4. As shown by their respective correlation coefficients (r^2), both curves fit the data extremely well. The maximum increases in growth rate (Δg) are similar and a comparison of the c_{50} values show that similar promotion using DOWFAX can be obtained at roughly 1/4 the concentration of SDS. Considering that the DOWFAX mixture contains both gemini surfactant (~25%) and monoalkyl disulfonate surfactant (~75%), these results are consistent with previous results found using pure gemini surfactants (Kwon *et al.*, 2011). It is also important to note that the s value for DOWFAX is lower than that for SDS, indicating a larger increase in growth rate for each mole of DOWFAX added. However, the s value is not as low as might be expected considering the difference in properties between gemini surfactants and conventional surfactants. Further testing should be done on a variety of anionic surfactants to test whether the s value will remain within the same range and whether it is characteristic for specific types of surfactants.

Table 4.2 – Sigmoid model parameters and fit for each surfactant

compound	r^2	g_0 (μmol/s)	Δg (μmol/s)	c_{50} (ppm)	s (ppm)
SDS	0.993	14.0	54.1	219	36.7
DOWFAX	0.986	14.4	45.0	51.0	19.7

4.6 Conclusion

The growth promotion effects of SDS and DOWFAX 8390 surfactants on methane hydrate were experimentally analyzed. Both surfactants were found to have no effect on methane solubility at equilibrium, but did have a pronounced effect on bulk methane mole fraction at surfactant concentrations that significantly promoted hydrate growth. Using the Bergeron and Servio growth model, the change in mole fraction leads to an increase in the driving force for hydrate growth and explains roughly half of the increase in growth. Further investigation into the effects of surfactants at the vapour-liquid and hydrate-liquid interfaces should be performed to understand their role in hydrate growth promotion. Hydrate growth rate was plotted against surfactant concentration for both surfactants tested and showed similar sigmoid trends. These curves are believed to be characteristic of hydrate growth promotion by surfactants, and indicate a smooth increase in hydrate growth promotion, rather than a sudden increase beyond a specific surfactant concentration. A sigmoid model has been proposed to facilitate the comparison of various surfactants at promoting gas hydrate growth. Both surfactants promote hydrate growth at a rate 4.5 times that of pure water; however, DOWFAX 8390 can achieve this promotion at 1/4 the concentration of SDS and has a larger increase in promotion per unit mass of surfactant added.

4.7 Acknowledgements

The authors are grateful to the Natural Sciences and Engineering Research Council of Canada (NSERC), McGill University, le Fonds Québécois de la Recherche sur la Nature et les Technologies (FQRNT), the Canada Research Chair Program (CRC) and the Eugene Ulmer Lamothe Fund (EUL) in the McGill Department of Chemical Engineering for funding and support.

Chapter 5

Phase equilibria and solubility in CO_2/CH_4—tetra-n-butylammounium bromide aqueous semi-clathrate systems [1]

5.1 Preface

As outlined in chapter 4, future work evaluating the promotion mechanism of surfactants should involve particle size analysis. Experiments were undertaken using methane, propane and carbon dioxide hydrates with surfactants. Methane and propane hydrate crystals were too large for particle size analysis measurement using the available setup. Carbon dioxide clathrate crystals were in range for particle size analysis but surfactants were ineffective at promoting growth. This is likely due to the presence of carbonate and bicarbonate ions displacing the surfactants from the hydrate surface. Due to these difficulties, no further experiments were undertaken

1. Reproduced in part with permission from Verrett, J., Renault-Crispo, J.-S. and Servio, P., 2015. Phase equilibria, solubility and modeling study of CO2/CH4+tetra-n-butylammonium bromide aqueous semi-clathrate systems, *Fluid Phase Equilibria*, **388**: 160-168.

to characterize hydrate promotion by surfactants. Attention was shifted to tetra-n-butylammonium bromide (TBAB) as an additive due to it's promising promotion properties and need for further characterization in literature. Semi-clathrates formed with TBAB showed promising results for particle size analysis; however, before hydrate kinetics could be evaluated, a greater understanding of system thermodynamics was required. The addition of another component (TBAB) made the system more thermodynamically complex to analyze. A procedure was thus developed to characterize the solubility of the carbon dioxide and methane as well as the mole fraction of TBAB in the liquid.

5.2 Abstract

Interest has grown in tetra-n-butylammonium bromide (TBAB) semi-clathrates due to their formation at lower pressures and higher temperatures than conventional gas hydrates. This study focuses on TBAB semi-clathrates formed with carbon dioxide and methane and is, to our knowledge, the first study to report and model semi-clathrate former solubility under hydrate-liquid-vapour equilibrium conditions. Equilibrium conditions were measured over the temperature range of 281 K to 294 K, pressure range of 0.377 MPa to 11.000 MPa and TBAB composition range of 5 wt% to 40 wt%. The current study is the first known to report the solubility of guest gas compounds in semi-clathrate systems and presents a basis for future research into hydrate former solubility in semi-clathrate systems.

5.3 Introduction

Clathrate hydrates are non-stoichiometric crystalline compounds composed of a water lattice held together through hydrogen bonding that is further stabilized by guest molecules occupying cavities in the lattice structure (Sloan and Koh, 2008). Clathrates typically form at moderate temperatures (<300 K) and high pressures

(>1 MPa), although formation conditions vary greatly based on the guest species. Industrial interest in gas hydrates was initially spurred on in the 1930's following a report by Hammerschmidt (1934) citing hydrate formation as the reason for blockages in natural gas pipelines. Since this time, many applications have been proposed for these compounds such as gas transport, storage and separation as well as water desalination and food processing (Eslamimanesh *et al.*, 2012). Though energetically favorable for use in many applications, slow formation kinetics as well as a lack of economic and scalability studies have prevented larger scale use of hydrate technologies (Eslamimanesh *et al.*, 2012).

To address the slow kinetics of formation of gas hydrates, research has been undertaken to promote growth using a variety of means. One method uses chemical promoters added to the solution to increase the rate of hydrate formation. These can be separated into two broad categories of either kinetic or thermodynamic promoters. Kinetic promotion involves substances that have been shown to significantly increase hydrate formation rates without affecting thermodynamic equilibrium. Commonly studied kinetic promoters are generally surfactants, the most notable of which is sodium dodecyl sulphate (Ricaurte *et al.*, 2013; Kumar *et al.*, 2013). Thermodynamic promotion involves the addition of another guest substance that makes hydrate formation more energetically favorable. This shifts equilibrium conditions and either reduces the pressure or correspondingly increases the temperature at which hydrates will form. Examples of these thermodynamic promoters include tetrahydrofuran (THF) and cyclopentane, which generally integrate into larger cages in the hydrate structure, and thus facilitate the storage of smaller gas molecules such as methane (CH_4) or carbon dioxide (CO_2) in the empty smaller cages (Torré *et al.*, 2012; Lirio *et al.*, 2013; Zhong *et al.*, 2013).

Promoter research has recently shifted to hydrate compounds known as semi-clathrates. The lattice structure of these compounds is different from those of conventional clathrates that contain only water and guest molecules. Semi-clathrates integrate organic salts into their crystal structure, thereby further stabilizing the crystal lattice and allowing formation at more moderate conditions (lower pressures

and/or higher temperatures) (Arjmandi *et al.*, 2007; Sun and Sun, 2010). Studies have focused on using a variety of halide salts as promoters to form semi-clathrates. One of the most extensively studied salts to date is TBAB, which has been very successful at forming hydrates at more moderate conditions (Mayoufi *et al.*, 2010).

There has been substantial research progress in the past decade on semi-clathrates; however, studies have not yet measured the solubility, being the liquid mole fraction at equilibrium, of guest gases in the liquid under hydrate forming conditions. Knowledge of liquid phase composition, most notably with respect to the guest gas, is essential for developing kinetic models for reactor design (Bergeron and Servio, 2009). The importance of accurate modelling of the liquid phase has been highlighted in the literature showing that equilibrium values obtained by thermodynamic models are much more sensitive to liquid parameters than to gas parameters (Renault-Crispo *et al.*, 2014). To enhance understanding of the semi-clathrate equilibrium, the current study investigates equilibrium pressure, temperature and liquid phase composition of TBAB hydrates formed with carbon dioxide or methane. To our knowledge, this is the first study to measure liquid solubility for a three-phase hydrate-liquid-vapour semi-clathrate system.

5.4 Experimental apparatus

5.4.1 Experimental setup

A detailed description of the experimental setup can be found in a previous report (Bruusgaard *et al.*, 2010). Briefly it consists of a 600-cm^3 stainless steel reactor with a mounted stirrer and viewing windows. The setup provides access to liquid and gas samples via three ports at the top, middle and bottom of the reactor. Reactor temperature is controlled through a glycol water bath. Pressure measurements are performed using a Rosemount transducer with a span of 0-14 MPa and an accuracy of ±0.065% of the span. Temperatures are monitored using Omega platinum resistance temperature device probes with an accuracy of ±0.1 K.

5.4.2 Materials

TBAB was purchased from Sigma Aldrich as a 50 wt% aqueous solution. All gases used were obtained from MEGS Inc. and included ultra-high purity CH_4 gas (99.99%) and CO_2 gas (99.99%). Deoinized water was produced in house.

5.4.3 Procedure for equilibrium experiments

The reactor contains a holdup volume of roughly 40 mL and was cleaned by washing three times with 360 mL of the desired TBAB solution. Following this, 360 mL of the test solution was loaded into the reactor. The reactor gas was purged and replaced with the desired gas by pressurizing to 1.100 MPa, allowing time to mix, and then depressurizing to 0.150 MPa. This procedure to replace the gas was repeated three times, following which the pressure was brought to a level greater than the estimated equilibrium pressure from previous literature data (Arjmandi *et al.*, 2007; Sun and Sun, 2010; Mohammadi *et al.*, 2011; Li *et al.*, 2007; Ye and Zhang, 2012; Deschamps and Dalmazzone, 2009). Stirring was started and once hydrates formed, the pressure was decreased to be near the estimated equilibrium pressure. The system was then left to equilibrate under stirring for a minimum of 12 hours (h). During this time, pressure was monitored and changes of no more than 0.001 MPa were observed within the hour before measurement.

At the time of measurement, the pressure and temperature were recorded and the stirring was turned off. Hydrates would agglomerate and float or sink based on their guest compound. Five liquid samples of roughly 10 mL were then drawn into sample bombs through a high-pressure inline filter with a 20-nm nominal rating (Norman Filters). The sample bombs used had been weighed, vacuum pumped and put to chill in the reactor bath before sampling to ensure thermal consistency. The first liquid sample taken was used to clear the sample line and was then discarded, while the other four samples were used for analysis. A schematic showing the analysis of each sample bomb can be seen in figure 5.1. This consisted of first weighing of the bombs following sample loading. A gasometer was then used to depressurize

the sample bombs, which were left for 2 h to equilibrate. Gas volume, temperature, and atmospheric pressure were noted. The liquid was then taken out of the sample bombs, weighed, and placed on a hotplate to evaporate the water and leave only the TBAB salt. Following 2 h at 80 °C, the water had completely evaporated leaving only the solid TBAB to be weighed. The samples bombs were then washed and the process repeated at the next measurement condition.

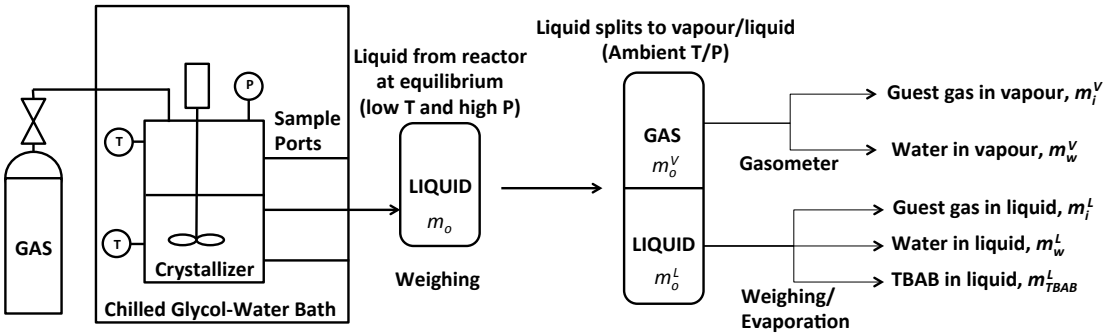

Figure 5.1 – A schematic of the procedure for determining the composition of the liquid samples taken from the crystallizer

5.5 Results and Discussion

5.5.1 Solubility Calculations

The solubility calculations performed are similar to those done on previous hydrate systems with a slight modification to determine the TBAB content in the liquid (Servio and Englezos, 2002). As shown by the measurement procedure in figure 5.1, it was assumed that the gas recovered in the gasometer contained only water vapour and guest gas (either carbon dioxide or methane). Gas species were assumed to be ideal at ambient conditions, and the mass of each species, i, was calculated using equation 5.1. Water pressure was assumed to be the vapour pressure at the ambient temperature and was calculated using the Antoine parameters found in the NIST webbook (Chase *et al.*, 1985). Guest gas pressure was then calculated using the ambient pressure as total pressure and subtracting the water vapour pressure.

$$m_i^v = \frac{P_i V_{gasometer} MW_i}{RT_{ambient}} \tag{5.1}$$

The weight of the liquid following depressurization was computed taking into account the mass of guest and water in the vapour using equation 5.2.

$$m_o^l = m_o - m_i^v - m_w^v \tag{5.2}$$

The fraction of TBAB in the liquid phase was computed using the measured weights of solution before and after drying. This was then used to find the TBAB and water mass fractions in the liquid as shown in equations 5.3 and 5.4.

$$m_{TBAB}^l = m_o^l * w_{TBAB} \tag{5.3}$$

and

$$m_w^l = m_o^l * (1 - w_{TBAB}) \tag{5.4}$$

The fraction of guest gas remaining in the liquid was computed using the ap-

propriate Henry's constants found in the NIST webbook (Chase *et al.*, 1985). This value represented less than 0.1% of the total number of moles of liquid water, and therefore was not taken into account in calculating the number of moles of liquid water. However it can represent up to 4% of the total number of moles of the guest gas and is thus important to include in calculating the total number of moles of guest gas in the sample. Standard uncertainties for temperature and pressure were estimated to be $u(T) = 0.1$ K and $u(P) = 0.009$ MPa respectively. Uncertainty values for mole fractions were obtained using equations 5.5 and 5.6 (Montgomery and Runger, 2007).

$$u = \frac{\sigma}{\sqrt{q}} \tag{5.5}$$

and

$$\sigma = \sqrt{\frac{\Sigma_{k=1}^{n}(b_k - \bar{b})}{q-1}} \tag{5.6}$$

where b is a general variable, with $\bar{b}$ being the average of a given set of q values of b, σ is the standard deviation and u is the standard uncertainty.

5.5.2 Equilibrium Measurements

Equilibrium pressure and temperature data for various TBAB loading concentrations can be found in figure 5.2 for carbon dioxide and figure 5.3 for methane. Previous literature values for temperature and pressure at equilibrium at similar TBAB concentrations are shown for comparison. The pressure values found in this study are similar or generally higher than those found elsewhere for the same temperature. This is likely due to previous literature studies measuring the point of hydrate dissociation using the isochoric search method to find the three-phase equilibrium. With this method, the amount of TBAB in the liquid phase is roughly equal to that of the loading composition. In this study, however, the hydrate phase was included during measurement. The TBAB loading concentrations used were gener-

ally lower than the stoichiometric amount of TBAB in the semi-clathrate structure, which is estimated to be near 40 wt%; however, this depends on the crystal structure (Gholinezhad *et al.*, 2011). The amount of TBAB in the liquid is therefore expected to be lower than the loading composition because a larger concentration of TBAB is stored in the solid hydrate phase. Indeed, liquid TBAB measurements, given in table 5.1, showed compositions slightly lower than the loading compositions. With less TBAB in the solution, the promotion effect is less pronounced, and it is expected that the equilibrium data would shift to higher pressures or lower temperatures. Liquid solubility measurements for carbon dioxide and methane systems can be found in figure 5.4 and figure 5.5 respectively. Exact values of temperature, pressure and liquid mole fractions can be found in table 5.1 for carbon dioxide and table 5.2 for methane. Note that the uncertainties for temperature and pressure are 0.1 K and 0.009 MPa respectively.

Table 5.1 – Experimental hydrate-liquid-vapour equilibrium data for temperature (T), pressure (P), carbon dioxide mole fraction ($x_{CO_2}^{H-L-V}$) and TBAB mole fraction (x_{TBAB}^{H-L-V}) with standard uncertainties $u(x_{CO_2}^{H-L-V})$ and $u(x_{TBAB}^{H-L-V})$ for the system CO_2—TBAB—H_2O at various TBAB loading compositions w_{TBAB}

w_{TBAB} (wt%)	T (K)	P (MPa)	$x_{CO_2}^{H-L-V}$ [$\times 10^3$]	$u(x_{CO_2}^{H-L-V})$ [$\times 10^3$]	x_{TBAB}^{H-L-V} [$\times 10^3$]	$u(x_{TBAB}^{H-L-V})$ [$\times 10^3$]
5	281.1	0.859	7.054	0.038	2.436	0.017
5	283.1	1.329	10.007	0.091	2.714	0.028
5	285.1	2.526	16.47	0.046	2.635	0.016
5	286.1	3.254	19.474	0.026	2.729	0.004
5	287.2	4.678	23.89	0.213	2.711	0.033
10	283.1	0.683	4.97	0.236	5.062	0.186
10	285.1	1.352	9.08	0.09	4.939	0.011
10	287.4	2.317	13.33	0.041	5.475	0.032
10	288.2	3.011	16.193	0.074	5.526	0.1
10	289.1	3.975	19.183	0.03	5.471	0.035
40	285.1	0.477	3.144	0.05	35.577	0.368
40	287.1	1.021	9.462	0.564	36.18	0.372
40	289.2	1.957	13.411	0.374	37.537	0.432
40	290.1	2.609	15.535	0.115	34.31	0.392
40	291.2	3.594	21.418	0.753	36.157	0.317

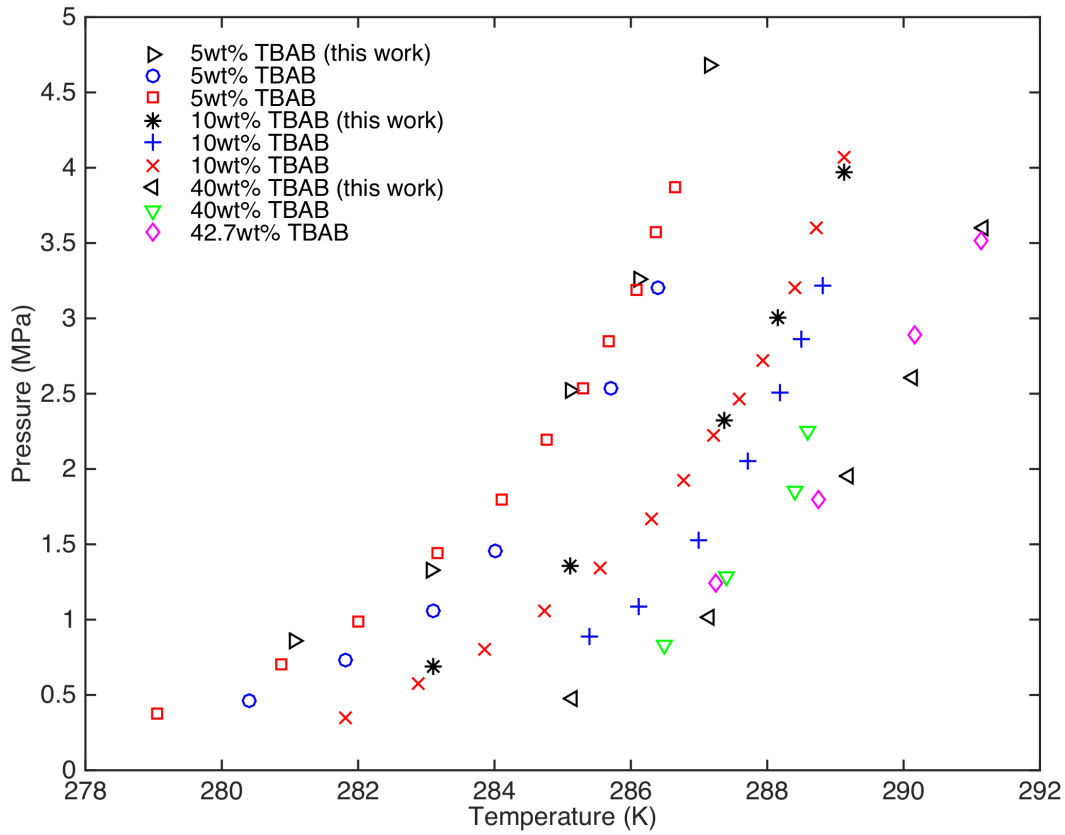

Figure 5.2 – Experimental hydrate-liquid-vapour equilibrium pressures at various temperatures and TBAB loading concentrations for the system CO_2—TBAB—H_2O. This work: ▷, 5 wt%; ⋆, 10 wt%; ◁, 40 wt%; Literature: ○, 5 wt% (Mohammadi *et al.*, 2011); □, 5 wt% (Ye and Zhang, 2012); +, 10 wt% (Mohammadi *et al.*, 2011); ×, 10 wt% (Ye and Zhang, 2012); ▽, 40 wt% (Deschamps and Dalmazzone, 2009); ◇, 42.7 wt% (Arjmandi *et al.*, 2007)

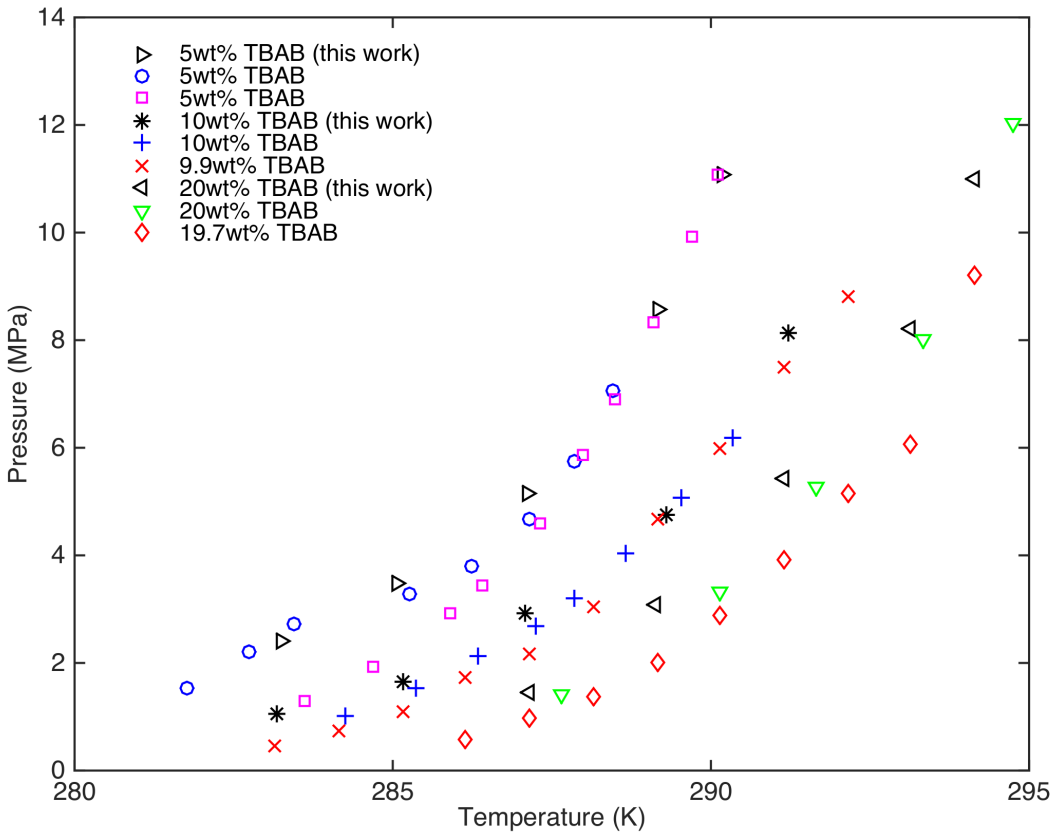

Figure 5.3 – Experimental hydrate-liquid-vapour equilibrium pressures at various temperatures and TBAB loading concentrations for the system CH_4—TBAB—H_2O. This work: ▷, 5 wt%; ⋆, 10 wt%; ◁, 20 wt%; Literature: ○, 5 wt% (Sun and Sun, 2010); □, 5 wt% (Mohammadi *et al.*, 2011); +, 10 wt% (Sun and Sun, 2010); ×, 9.9 wt% (Li *et al.*, 2007); ▽, 20 wt% (Arjmandi *et al.*, 2007); ◇,19.7 wt% (Li *et al.*, 2007)

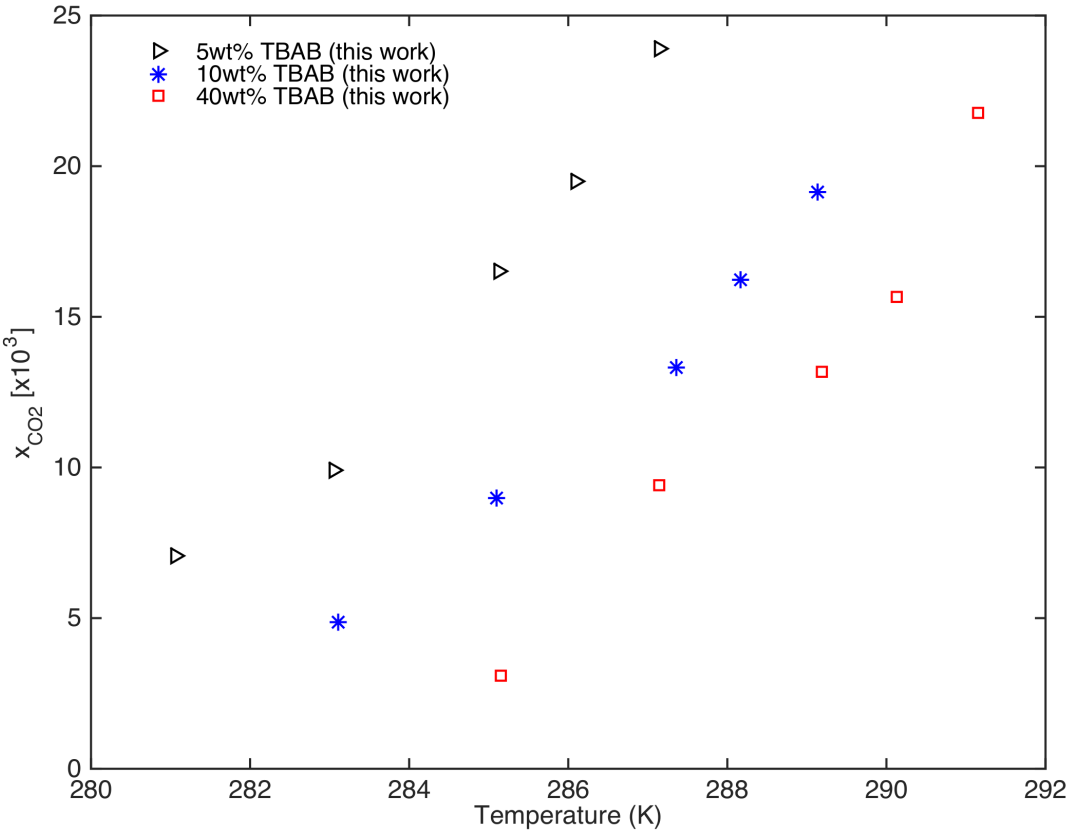

Figure 5.4 – Experimental hydrate-liquid-vapour equilibrium CO_2 solubilities at various temperatures and TBAB loading concentrations for the system CO_2—TBAB—H_2O. This work: ▷, 5 wt%; ∗, 10 wt%; □, 40 wt%

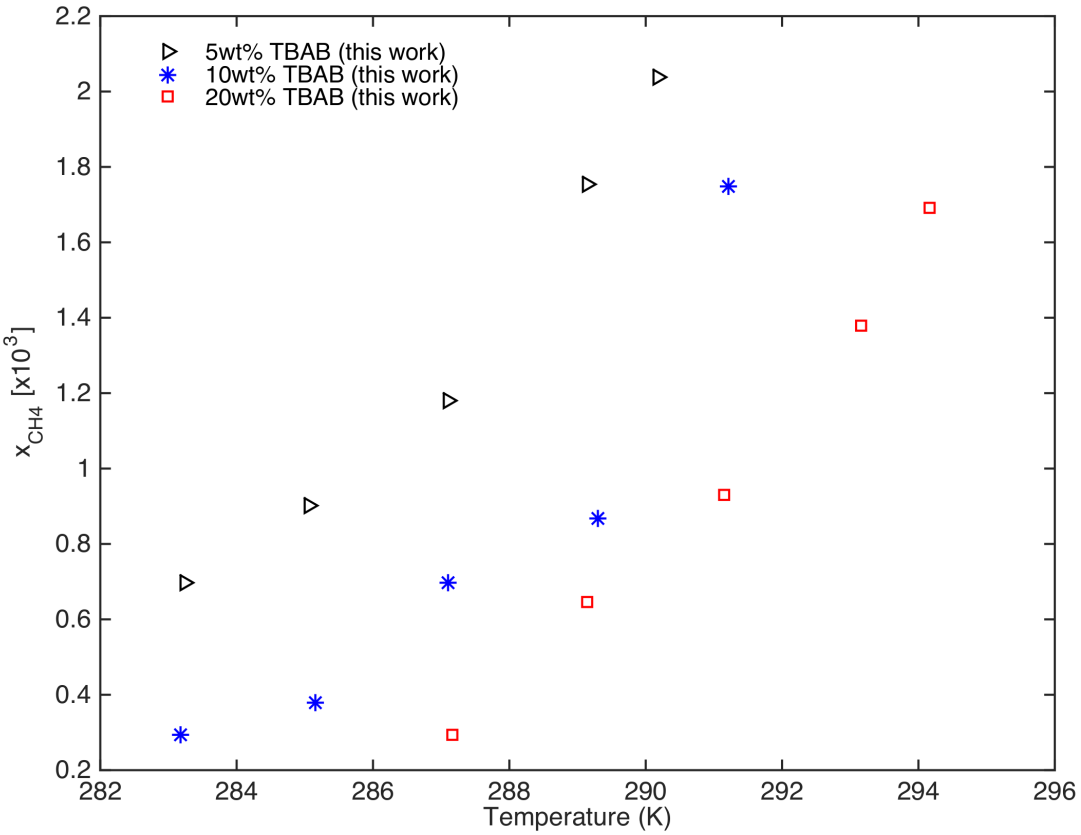

Figure 5.5 – Experimental hydrate-liquid-vapour equilibrium CH_4 solubilities at various temperatures and TBAB loading concentrations for the system CH_4—TBAB—H_2O. This work: $\triangleright$, 5 wt%; $*$, 10 wt%; $\square$, 20 wt%

Table 5.2 – Experimental hydrate-liquid-vapour equilibrium data for temperature (T), pressure (P), methane mole fraction ($x_{CH_4}^{H-L-V}$) and TBAB mole fraction (x_{TBAB}^{H-L-V}) with standard uncertainties $u(x_{CH_4}^{H-L-V})$ and $u(x_{TBAB}^{H-L-V})$ for the system CH_4—TBAB—H_2O at various TBAB loading compositions w_{TBAB}

w_{TBAB} (wt%)	T (K)	P (MPa)	$x_{CH_4}^{H-L-V}$ [$\times 10^3$]	$u(x_{CH_4}^{H-L-V})$ [$\times 10^3$]	x_{TBAB}^{H-L-V} [$\times 10^3$]	$u(x_{TBAB}^{H-L-V})$ [$\times 10^3$]
5	283.3	2.417	0.7	0.011	2.208	0.036
5	285.1	3.496	0.88	0.022	2.847	0.044
5	287.1	5.137	1.18	0.003	2.77	0.012
5	289.2	8.58	1.761	0.014	2.884	0.052
5	290.2	11.093	2.037	0.003	2.783	0.024
10	283.2	1.047	0.293	0.007	4.666	0.027
10	285.2	1.652	0.38	0.009	5.365	0.092
10	287.1	2.904	0.7	0.003	5.333	0.032
10	289.3	4.733	0.868	0.006	5.623	0.021
10	291.2	8.136	1.523	0.001	5.38	0.049
20	287.2	1.435	0.296	0.011	11.028	0.037
20	289.1	3.078	0.648	0.004	10.898	0.042
20	291.1	5.434	0.929	0.002	11.075	0.045
20	293.2	8.202	1.378	0.011	11.025	0.051
20	294.2	11.013	1.693	0.005	10.847	0.038

5.6 Conclusion

Equilibrium measurements of three-phase hydrate-liquid-vapour systems containing TBAB, water and either CO_2 or CH_4 were undertaken. Measurements were performed in the temperature range of 281 K to 294 K, pressure range of 0.377 MPa to 11.000 MPa and TBAB composition range of 5 wt% to 40 wt%. The equilibrium data is shown to be consistent through the comparison of the obtained temperature and pressure values with data in the literature where available. In addition the study provides solubility of all components in the liquid phase and is, to the authors' knowledge, the first such report to do so. These solubility data provide critical information to increase the accuracy of thermodynamic and kinetic models of CO_2 and CH_4 TBAB semi-clathrates.

5.7 Acknowledgements

The authors are grateful to the Natural Sciences and Engineering Research Council of Canada (NSERC), McGill University and specifically the McGill Engineering Doctoral Award (MEDA), le Fonds Québécois de la Recherche sur la Nature et les Technologies (FQRNT) and the Canada Research Chair Program (CRC) for financial funding and support.

Chapter 6

Reaction rate constant of CO_2—tetra-n-butylammounium bromide semi-clathrate formation [1]

6.1 Preface

Chapter 5 provides solubility data for the carbon dioxide—water—tetra-n-butyl ammonium bromide system. Using those results, this chapter focuses on characterizing the growth of carbon dioxide semi-clathrate hydrates. A kinetic model is developed in order to obtain estimates of the intrinsic reaction rate at various operating conditions. This model is applied to characterize and contrast semi-clathrate growth with the growth of pure clathrates.

1. Reproduced in part with permission from Verrett, J., and Servio, P., *Reaction rate constant of carbon dioxide—tetra-n-butylammounium bromide semi-clathrate formation*, private communication

6.2 Abstract

Semi-clathrate growth experiments were performed using a carbon dioxide—water—tetra-n-butyl ammonium bromide system. Experiments were conducted in a semi-batch stirred tank crystallizer at temperatures of 287 K, 288 K and 289 K with a 3-K subcooling at each temperature. Gas consumption, temperature, hydrate former mole fraction and particle size were measured throughout growth. Significant differences in gas consumption and heat effects were observed with these systems compared with pure clathrate systems. A kinetic growth model was applied to estimate the intrinsic rate constant. Rate constants did not show a clear trend with temperature at the conditions studied. Intrinsic reaction rate constant values ranged from 7.6×10^{-6} m/s to 13.8×10^{-6} m/s.

6.3 Introduction

Clathrate hydrates are crystalline structures formed of water cages stabilized by guest compounds (Englezos, 1993; Sloan and Koh, 2008). They have garnered industrial interest for their potential use in gas separation and storage as well as phase change materials (Ogoshi and Takao, 2004; Ma *et al.*, 2010; Jerbi *et al.*, 2013). Notably, they have been studied for their use as a carbon sequestration technology due to their ability to separate and store carbon dioxide (CO_2) from flue gas streams (Linga *et al.*, 2008).

An alternative clathrate form, known as semi-clathrate hydrates, incorporates molecules other than water to form the cage structure (Shimada *et al.*, 2005). One family of guest compounds that forms such semi-clathrates is quaternary ammonium salts (Gaponenko *et al.*, 1984). These compounds were initially described by Fowler *et al.* in early 1940 and later analyzed by X-ray crystallography by McMullan and Jeffrey (1959). They act to stabilize the hydrate lattice leading to the formation of hydrates at more favorable thermodynamic conditions, for example higher temperature or lower pressure (Mayoufi *et al.*, 2010; Verrett *et al.*, 2015). One salt

in this family, tetra-n-butylammonium bromide or TBAB, significantly stabilizes the crystal lattice while also maintaining a high gas storage capacity (Lin *et al.*, 2013). These properties have led to a keen interest in utilizing such a compound in industrial settings as a gas hydrate promoter (Eslamimanesh *et al.*, 2012).

Despite this interest, relatively little work has been done to characterize and model the kinetics of semi-clathrate hydrate formation (Trueba *et al.*, 2012; Park *et al.*, 2013). Kinetic models have previously been applied to pure clathrate hydrates in order to estimate reaction parameters such as the rate constant (Bergeron and Servio, 2008). Such parameters are essential to the implementation and scale-up of clathrate technologies in industrial processes. Using a model system of CO_2, TBAB and water, this paper applies kinetic models to evaluate semi-clathrate hydrate growth.

6.4 Theory

A variety of kinetic models have been proposed for stirred hydrate forming systems. This paper will not go over these models in detail, but points the reader to an excellent review by Ribeiro and Lage for a perspective on their development (2008). Mass-transfer models have been widely used to describe hydrate growth because the parameters required for modelling can be readily measured or estimated. Viewing hydrate formation as a mass-transfer problem, previous models describe gas hydrate former transfer across two interfaces: vapour-liquid (IF^{V-L}) and hydrate-liquid (IF^{H-L}), each consisting of two resistances as shown in figure 6.1.

The vapour-liquid interface has a resistance to mass transfer on both the liquid (r_L^{V-L}) and vapour side (r_V^{V-L}) of the interface. A scaling analysis shows that the resistance on the vapour side of the interface is negligible compared to that of the liquid side (Deen, 1998). To avoid the need to characterize mass-transfer at the vapour-liquid interface, Bergeron and Servio measured gas concentration in the bulk liquid during hydrate growth (Bergeron and Servio, 2009). This approach, however, assumes that the majority of crystal growth occurs in the liquid bulk and

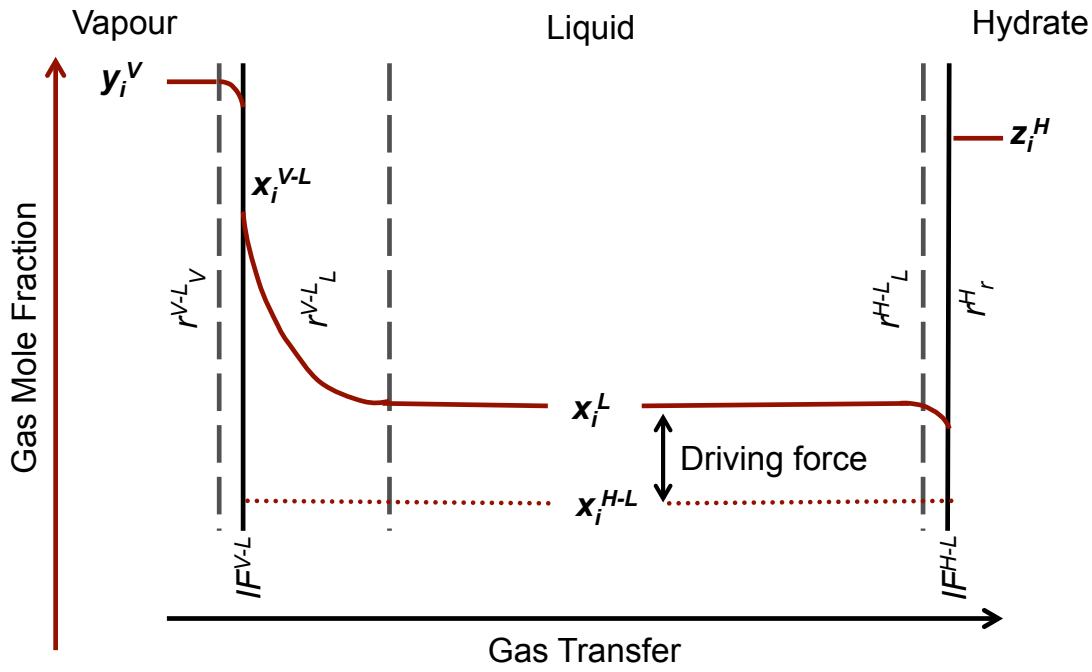

Figure 6.1 – Schematic of gas transfer from vapour to hydrate with resistances (r) present at each interface (IF). Phases are denoted as vapour (V), liquid (L) and hydrate (H) with composition of the hydrate forming component denoted as y_i, x_i and z_i respectively in each phase

contrasts with the approach of two-film theory (Vysniauskas and Bishnoi, 1983). Two-film theory dictates that higher growth will occur in the diffusion layer near the vapour-liquid interface due to higher gas concentrations. The two-film model is quite useful for stagnant systems, however, results by Herri *et al.* (1999) estimate the film thickness to be on the order of tens of micrometres for stirred systems. Given that stirred crystallizers have a depth on the order of centimetres, this volume represents a tiny fraction of the system. Furthermore, the difference in driving force for crystal growth between the two regions is not estimated to be greater than an order of magnitude. We thus assume in this study that the effect of the film is negligible compared to crystal growth occurring in the bulk liquid.

The liquid-hydrate interface consists of a resistance to mass transfer to the hydrate surface (r_L^{H-L}) and a resistance to the formation of hydrate, which we will denote as the resistance of reaction (r_r^H). Since there is no estimate for the reaction resistance, a scaling analysis can only be performed with the experimental results. The mass transfer rate for gas to the hydrate particle (k_{H-L}) can be estimated using equation 6.1, which describes the Sherwood (Sh) number in agitated vessels with particles under 30 μm (Armenante and Kirwan, 1989). Within this equation, L is defined as the characteristic length, in this case particle diameter. Diffusivity (D) of carbon dioxide in water is estimated from the correlation of Wilke and Chang (1955) using the parameters of Hayduke and Laudie (1974). At a temperature of 287 K, the diffusivity is roughly 1.5×10^{-9} m^2/s. The Reynold's number for a particle (Re_p) in an agitated vessel can be found using equation 6.2. ϵ is the power input per mass of fluid calculated from equation 6.3 (Baldi *et al.*, 1978) and ν is the kinematic viscosity. The Schmidt number (Sc) can be calculated from equation 6.4. N_p is the power number of the stirring device, which is taken to be 1 for a four vertical blade impeller. d_s is the stirrer diameter of 3 cm, N is the stirring rate in rounds per second of 10.4 s^{-1}, and V is the liquid volume in the reactor.

$$Sh = \frac{k_{H-L} * L}{D} = 2 + 0.52 * Re_p^{0.52} * Sc^{1/3} \tag{6.1}$$

$$Re_p = \frac{L^{4/3} * \epsilon^{1/3}}{\nu} \tag{6.2}$$

$$\epsilon = \frac{N_p * d_s^5 * N^3}{V} \tag{6.3}$$

$$Sc = \frac{\nu}{D} \tag{6.4}$$

Since no scaling analysis can be performed without the experimental results, the kinetic growth equation developed by Bergeron and Servio (2009) is modified to use an overall rate constant (k) in equation 6.5. This overall rate constant is composed

of the mass transfer coefficient (k_{H-L}) and intrinsic reaction rate constant (k_r) as shown in equation 6.6.

$$\frac{dn_i}{dt} = \frac{v_{0w} a_w(t) \rho_w}{MW_w} \frac{(x_i^l - x_i^{H-L-V})}{1/(\pi \mu_2(t) k)} \tag{6.5}$$

$$k = \frac{1}{\frac{1}{k_{H-L}} + \frac{1}{k_r}} \tag{6.6}$$

Equation 6.5 has a gas consumption term ($\frac{dn_i}{dt}$) on the left-hand side. The right-hand side consists of the initial volume (V_{0w}), density (ρ_w) and molecular weight (MW_w) of water along with a term to account for the volumetric fraction water remaining as a function of time, $a_w(t)$. The next term represents the concentration driving force, being the difference between the bulk liquid mole fraction of CO_2 (x_i^L) and the CO_2 solubility under hydrate-liquid-vapour equilibrium at the experimental temperature and three-phase equilibrium pressure (x_i^{H-L-V}). Ideally the solubility should be calculated at the experimental pressure, which corresponds to a system in the hydrate-liquid region. However, previous results with pure clathrates indicate that solubility values at the three-phase equilibrium pressure will be similar to those in the hydrate-liquid region, since solubility has been shown to be a weak function of pressure (Servio and Englezos, 2002). This model assumes hydrate particles to be spherical, with particle area represented by the second moment of particle size distribution ($\mu_2(t)$).

A particle balance equation is used to model the size and number of particles in the reactor at a given time (Kane *et al.*, 1974). For simplicity, this model assumes that the growth rate (g) of all particles is independent of particle size. Furthermore, assuming all particles are formed at the moment of hydrate nucleation with no agglomeration, breakage or secondary nucleation, we obtain equation 6.7 to describe the system.

$$\frac{\partial \phi}{\partial t} + g \frac{\partial \phi}{\partial L} = 0 \tag{6.7}$$

To estimate particle area, the second moment of particle size distribution is defined in equation 6.8.

$$\mu_2(t) = \int_0^\infty L^2 \phi(L,t) dL \tag{6.8}$$

where $\phi(L,t)$ is the particle density distribution. The initial particle density distribution, $\phi(L,t_0)$ can be calculated from an initial normalized experimental particle size distribution, $\phi^{exp}(L,t_0)$ and initial density of hydrate particles, $\mu_0(t_0)$, using equation 6.9.

$$\phi(L,t_0) = \phi^{exp}(L,t_0)\mu_0(t_0) = \phi^{exp}(L,t_0)\frac{6MW_H(n_{tb}^l - n_i^l)}{\eta V_L \rho_H \pi \int_0^\infty \phi^{exp}(L,t_0)L^3 dL} \tag{6.9}$$

where MW_H and ρ_H are the hydrate molecular weight and density respectively. The amount of hydrate former involved in the formation of particles is calculated as the difference between the gas dissolved at turbidity before particle formation (n_{tb}^l) minus the amount of gas dissolved after turbidity (n_i^l). η is the moles of gas per mole of hydrate in the semi-clathrate structure and V_L is the liquid volume in the reactor system.

6.4.1 Semi-clathrate properties

There are five commonly documented crystal structures of TBAB semi-clathrate formed in systems under 60 wt% TBAB. These are reported to have hydration numbers of roughly 24, 26, 32, 36 and 38, each of which will be denoted 1:24, 1:26, 1:32, 1:36 and 1:38 respectively in this report (Shimada *et al.*, 2005; Gaponenko *et al.*, 1984; Lipkowski *et al.*, 2002). 1:36 and 1:38 show comparable cell parameters and an orthorhombic structure based on X-ray diffraction results (Shimada *et al.*, 2005; Gaponenko *et al.*, 1984). One of the papers reporting these values, by Gaponenko *et al.* (1984), suggests that the 1:36 with TBAB is isostructural with a 1:38 formed

with another quaternary ammonium salt, further showing their similarity. The results published by Shimada *et al.* (2005) suggest that these structures have 3 empty dodecahedral cages for each TBAB molecule. Experimental results with CO_2 semi-clathrates show a composition of roughly 2.51 CO_2 molecules per TBAB molecule (Lin *et al.*, 2008). Considering some cages may be unoccupied, this is consistent with the structure reported by Shimada *et al.* (2005).

X-ray data was reported for 1:32 in the work of McMullan and Jeffrey (1959). This structure is also detailed in the work of Davidson with a unit cell containing 20 large cages and 12 small dodecahedral cages (1973). Five TBAB molecules occupy the large cages and water molecules occupy 2 of the small cages. The other 10 small cages are left empty, leading to a theoretical composition of 2 CO_2 molecules per TBAB molecule. Crystallographic data for 1:24 and 1:26 can be found in literature (Gaponenko *et al.*, 1984); however, the author could find no description of the cage structure of such compounds. It will thus be assumed that these structures have 2 empty cages for each TBAB molecule.

The stability of the various structures of TBAB semi-clathrate have been investigated by examining melting temperature. 1:26 is reported to have the highest melting temperature in all studies performed (Lipkowski *et al.*, 2002; Aladko *et al.*, 2002). Lipkowski *et al.* (2002) examined 1:24, 1:26, 1:32 and 1:36 with results indicating that 1:26 is more stable than other structures in the range of roughly 33 wt% to 43 wt% TBAB. Oyama *et al.* (2005) performed a study examining the stability of 1:26 and 1:38 and found that 1:26 is more stable above 18 wt% TBAB. Due to its stability at its stoichiometric concentration of 40 wt% in water, 1:26 has been chosen as the focus of this study. Given the number of possible crystal structures, liquid phase composition of TBAB is measured throughout growth to verify the semi-clathrate structure present.

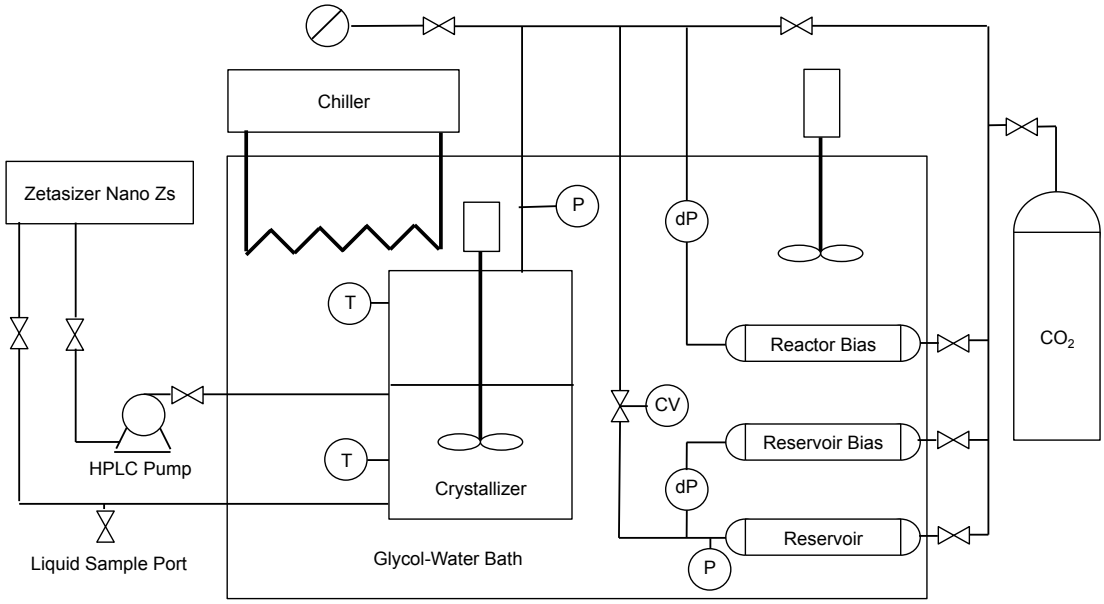

Figure 6.2 – Diagram of experimental setup with pressure transducers (P or dP), temperature transducers (T), and control valve (CV)

6.5 Experimental apparatus

6.5.1 Experimental setup

A detailed description of the experimental setup can be found in previous publications and is shown in figure 6.2 (Bergeron and Servio, 2008; Bergeron *et al.*, 2009). Briefly, it contains a 600-cm^3 stainless steel reactor with a magnetic stirrer inserted from the top. Gas is supplied by a 1000-cm^3 reservoir connected to the reactor by a control valve. Both reactor and reservoir also have 500-cm^3 bias tanks associated with them. Pressure is measured in all vessels using Rosemount pressure transducers with a span of 0-14 MPa for the reactor and reservoir and 0-2 MPa for the bias tanks. Uncertainty in pressure measurements is listed as ±0.065% of the span. Temperature is monitored in the reservoir, reactor gas and liquid using platinum resistance temperature devices (RTDs) with an uncertainty of ±0.1 K. The

entire setup is contained in a chilled glycol water bath.

The liquid in the reactor is connected to an external loop consisting of a sample port, high pressure pump (Lab Alliance 1500) and particle size analyzer. Liquid samples are removed using 20-cm^3 stainless steel cylinders. Depressurization of these cylinders is performed using a Chandler Gasometer with an uncertainty of ±0.4 cm^3. All weighing is performed using a Denver Instruments S-4002 balance with an uncertainty of ±0.01 g. The particle size analyzer is a Zetasizer Nano ZS with a 633-nm laser. It is capable of detecting particles in the size range of 0.6-6000 nm in diameter with a maximum uncertainty of 15% of particle size value. The instrument is fitted with a special stainless steel cuvette with sapphire windows, manufactured by Hellma, to withstand pressures up to 6 MPa. The Zetasizer also contains a temperature control system to maintain a desired temperature ranging from 0-90 °C.

6.5.2 Materials

CO_2 gas was obtained from MEGS Inc. with a purity greater than 99.99%. A solution of 50 wt% TBAB in water was obtained from Sigma Aldrich. Reverse osmosis (RO) water was obtained in house.

6.5.3 Experimental procedure

Experiments were performed at a variety of temperatures and pressures listed in table 6.1. Figure 6.3 shows a partial phase diagram for 40 wt% TBAB solutions. Experimental conditions were chosen in order to remain above the temperature of formation of TBAB-H_2O semi-clathrates, shown by the red dot-dash line, which contain no CO_2. Furthermore, conditions were also chosen to remain at a pressure under the liquefaction pressure of CO_2, shown by the blue dashed line (Oyama *et al.*, 2005; Span and Wagner, 1996).

Solutions of 40 wt% TBAB in water were prepared for all experiments. The

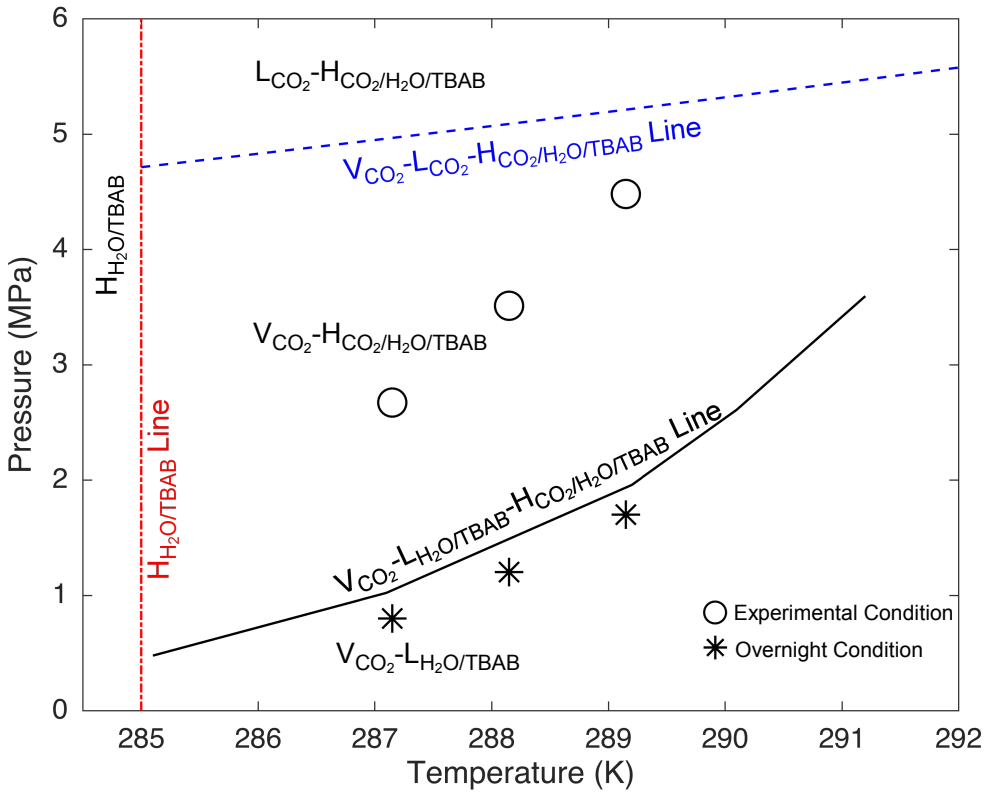

Figure 6.3 – Partial phase diagram for the CO_2-water-TBAB system at 40 wt% TBAB showing experimental temperatures and pressures tested and the pressure in the reactor before a run, denoted as overnight pressure

reactor was first rinsed with 360 mL of the solution three times to remove any impurities and then loaded with 300 mL of test solution with an uncertainty of ±5 mL. Following this, the reactor was purged with CO_2 by pressurizing to 1.1 MPa and depressurizing to 0.15 MPa three times. CO_2 was then loaded to a pressure in the vapour-liquid region, noted in table 6.1, and left overnight to equilibrate under stirring. This was done to ensure that each run was starting with the same concentration of dissolved CO_2. Pressures were chosen near the hydrate-liquid-vapour line to minimize the pressure increase required to get to experimental conditions.

Table 6.1 – Experimental temperatures and pressures and the pressure of the reactor before a run, denoted as overnight pressure

T^{exp} (K)	P^{exp} (MPa)	$P^{overnight}$ (MPa)
287	2.68	0.97
288	3.51	1.40
289	4.49	1.97

Before performing an experiment, the Zetasizer was warmed up to stabilize the laser and temperature controller. Pressure and temperature measurements were recorded using LabVIEW software. To start the experiment, the reactor was pressurized to the desired pressure corresponding to a 3-K subcooling. The reactor stirrer and HPLC pump were turned on with the control valve activated to maintain reactor pressure. Figure 6.4 shows typical trends for gas consumption and temperature from the beginning of an experimental run. Gas initially dissolves into the solution and follows a first-order response (Pasieka *et al.*, 2014). Once the solution is supersaturated, the formation of the semi-clathrate phase can occur. This nucleation, known as the turbidity point, is characterized by a rise in reactor temperature due to the exothermic nature of clathrate formation. The first particle size measurement was taken 150 s after hydrate formation. Particle size measurements were taken every 300 s with 150 s needed for refreshing the sample in the cuvette and 150 s for measurement. At any time during hydrate growth the reaction can be stopped, by halting stirring, and four liquid samples can be removed for analysis. This ends the experimental run due to the amount of liquid removed. Within this study, samples were removed at 100 s, 500 s, 1000 s and 1500 s following turbidity.

Liquid samples were analyzed to determine the molar composition of CO_2, TBAB and water in the sample. This was done by depressurizing samples with a gasometer followed by water evaporation. Details of the full technique used are described in Section 5.4 of this work. Pressure and temperature data were interpreted using the Trebble-Bishnoi equation of state to determine the number of moles of gas

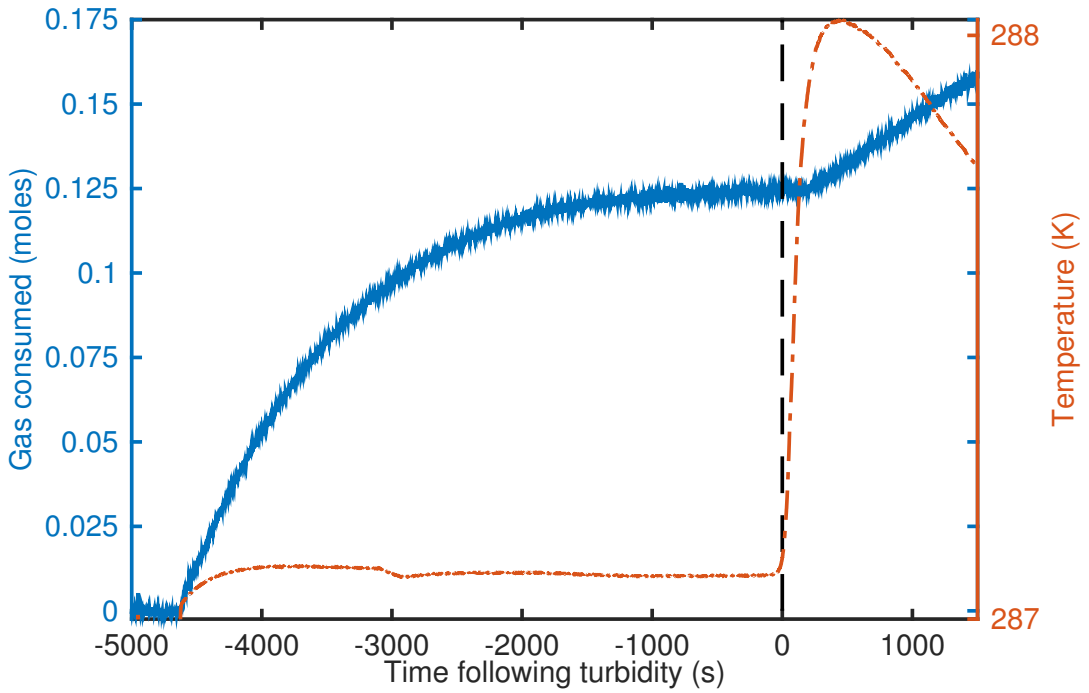

Figure 6.4 – Gas consumption (solid blue line) and reactor liquid temperature (dot-dashed red line) measurements from the start of an experimental run at 287 K

fed to the reactor (Trebble and Bishnoi, 1987). Uncertainty in the molar consumption value was calculated to be $\pm 1.1 \times 10^{-3}$ mol based on the variance in the signal for the molar consumption data. Particle size data were analyzed using optical parameters for carbon dioxide hydrates and ice, since no optical data were available for semi-clathrates. The refractive index was taken to be 1.347, as calculated for sI carbon dioxide hydrates (Bonnefoy *et al.*, 2005). The absorption value was taken from structure Ih ice and was regarded as negligible due to its value in the order of 10^{-8} (Warren and Brandt, 2008).

6.6 Results and discussion

6.6.1 Gas consumption and temperature

Typical curves for gas consumption and temperature following turbidity can be seen in figure 6.5. Both gas consumption and temperature are notably different from previous experiments with pure clathrates. Initially following turbidity, gas consumption in a semi-clathrate system appears to be negligible. This would indicate that the system is using gas dissolved prior to turbidity in the liquid to feed hydrate growth rather than requiring gas transferred after turbidity from the vapour phase. Average gas consumption during the linear portion of the trend can be found in table 6.2 and was calculated using data from 450 s after turbidity onwards. All runs were performed in duplicate and have similar values except those at 288 K, with this difference attributed to experimental error.

In pure clathrate studies performed previously with the setup, heat release following hydrate formation was negligible compared to the heat removal from the system, and thus reactor temperature remained roughly constant (Bergeron and Servio, 2008). With the semi-clathrate system, initial hydrate formation results in a temperature increase of nearly 1 K over a period of 400 s, after which the temperature plateaus. The latent heat of pure and semi CO_2 clathrates are roughly 500 J/g (Marinhas *et al.*, 2006) and 200 J/g (Oyama *et al.*, 2005) respectively, indicating that the increase in temperature in the current semi-clathrate system is not due to an increase in the heat of formation. The increase temperature can thus be attributed to an increased hydrate formation rate.

6.6.2 Driving force

The CO_2 liquid mole fraction was analyzed throughout growth, resulting in the mole fraction curves shown in figure 6.6. Mole fraction at turbidity (0 s) was estimated by combining the amount of CO_2 present in the liquid under vapour-liquid equilibrium before the experimental run and the amount of CO_2 consumed

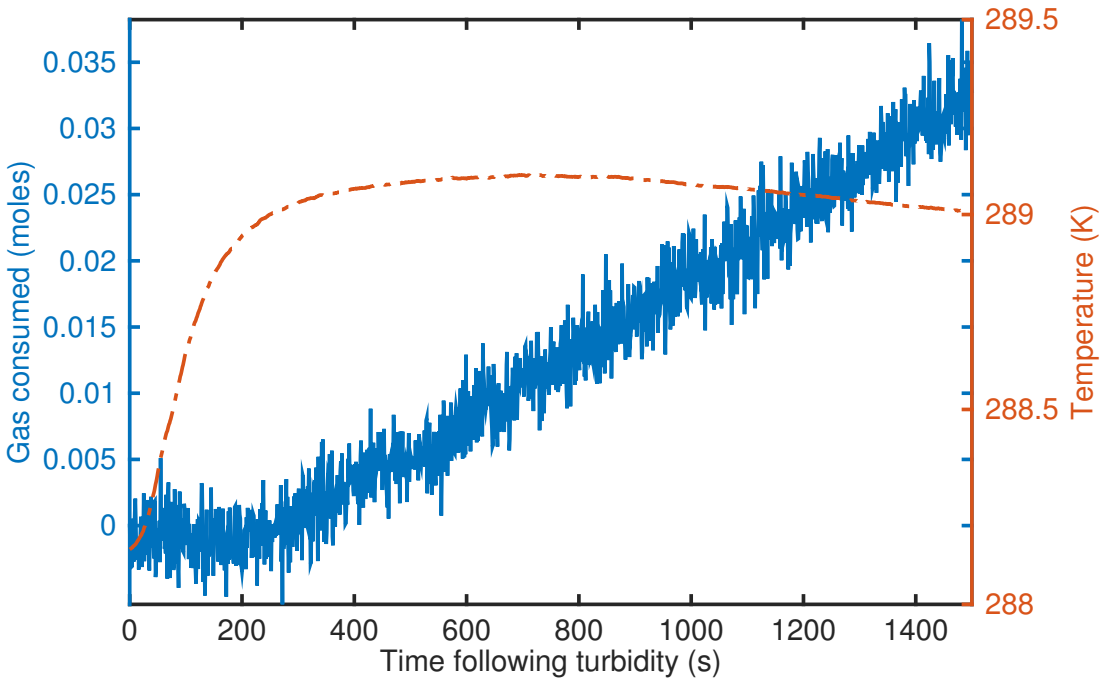

Figure 6.5 – Gas consumption (solid blue line) and reactor liquid temperature (dot-dashed red line) measurements after hydrate formation for an experimental run at 288 K

before turbidity. All data sets show a sharp decrease in mole fraction after turbidity followed by a roughly constant mole fraction from 500 s onwards. This corresponds to the gas consumption data and shows an excess of CO_2 in the liquid being consumed following hydrate formation. We believe the trend of constant mole fraction, from 500 s onwards, is due to a quasi-steady state wherein the CO_2 transfer from the gas phase matches the CO_2 being enclathrated. Mole fraction curves were fitted with a generic first-order response model of the form shown in equation 6.10. In this equation, n_0 and Δn are fitted parameters that represent the initial amount of gas and change in gas dissolved in the liquid respectively; τ, is the time constant and t, the time following turbidity. This equation allows the prediction of bulk mole fraction throughout growth at each experimental temperature studied.

Table 6.2 – Gas consumption and mole fraction driving force (df) at various experimental temperatures

T^{start} (K)	Gas consumption (mol/s) [$\times 10^5$]	df [$\times 10^4$]
287	1.80	13.075
287	1.67	12.927
288	1.90	11.261
288	2.99	11.768
289	1.30	11.095
289	1.33	11.361

$$x_i^l = n_0 + \Delta n * e^{\frac{-t}{\tau}} \tag{6.10}$$

The TBAB liquid mole fraction in all samples collected showed little deviation and was found to have an average composition of 39.3 wt% ± 0.2 wt%. This is similar to the loading composition of 40 wt% and corresponds to a hydration number of 26. The hydrate composition was thus assumed to be 26 H_2O : 1 TBAB : 2 CO_2.

The three-phase solubility was determined using reactor temperature data and was calculated based on a previously developed solubility model (Verrett *et al.*, 2015). Uncertainty in the solubility was obtained using the temperature uncertainty and found to be $\pm 4.5\times10^{-4}$ mol. Driving force for the reaction was assessed over time using the mole fraction and solubility data. Average values for driving forces calculated from 450 s after turbidity onwards can be found in table 6.2.

6.6.3 Particle size distribution

An example of particle size distributions over time can be found in figure 6.7. Particles smaller than 20 nm, which are not shown in the figure, were also present in all distributions. Signals below 20 nm were present in samples analyzed before hydrate nucleation and in the vapour-liquid region where hydrates do not form. We

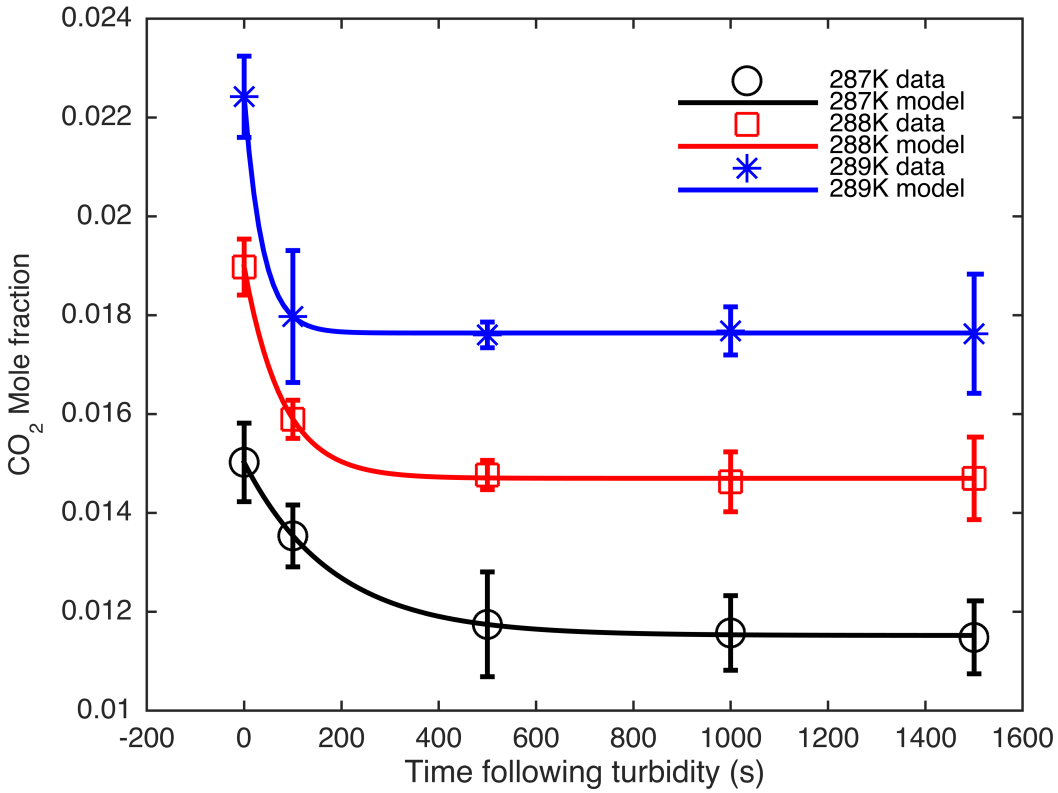

Figure 6.6 – Mole fraction of CO_2 in the bulk liquid with 95% confidence intervals at various times following hydrate formation for the experimental temperatures tested. Values were fit to a first-order model, shown as the solid lines

hypothesize that these signals were the result of TBAB in the system, as similar results were not found in samples of pure water. Furthermore, sizes below 20 nm are near the limit for homogeneous nucleation of hydrate particles (Englezos *et al.*, 1987a). Studies of other crystal systems indicate that nucleation is likely to occur heterogeneously and generate particles larger than those predicted by homogeneous nucleation theory (Mullin, 1997). Previous studies of hydrate crystallization report particles in the micron range, however the equipment used generally could not measure into the nanometre range (Herri *et al.*, 1999; Clarke and Bishnoi, 2005). Within

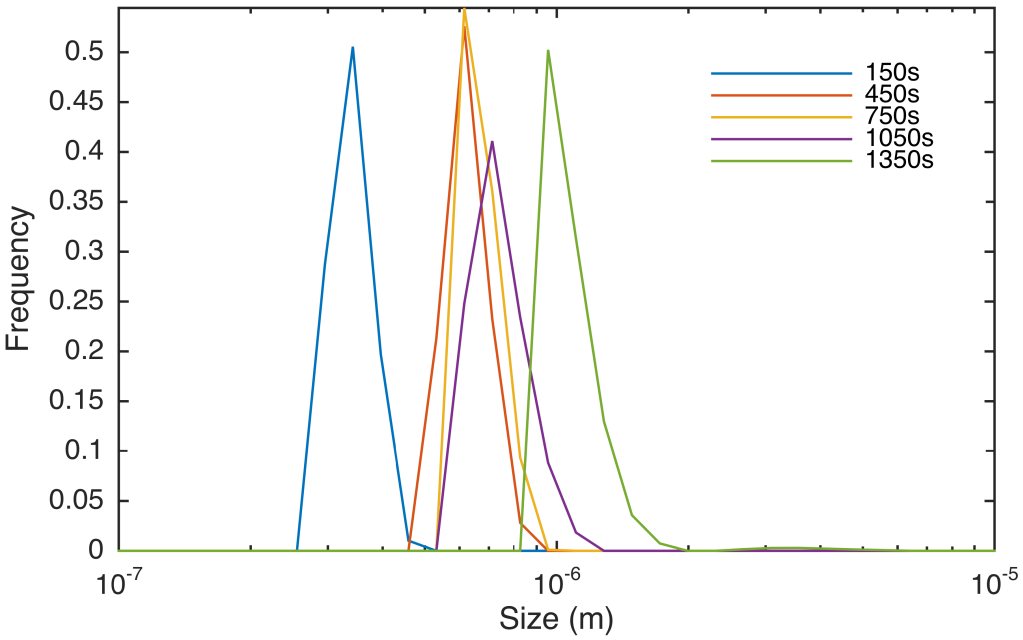

Figure 6.7 – Particle size distributions measured at various times during hydrate growth

this study, particles were found to have sizes ranging from 100 nm to 6 μm with a high variability in the particle sizes recorded. This variability is attributed to difficulties associated with measuring hydrates based on their optical properties and the equipment used. The refractive index of hydrate, at 1.347, is similar to that of water at 1.333 (Bonnefoy *et al.*, 2005). Furthermore, the Zetasizer is typically used to measure particles with much greater absorbance than the near negligible absorbance estimated for the semi-clathrates formed in this study (Warren and Brandt, 2008). In response to these difficulties, particle size results were averaged to get an estimate of particle size at each time of measurement. Using this result, the estimated number of particles initially formed in the system is of the order of 10^{13}. Agglomeration, breakage and secondary nucleation are not taken into account in this model. In order to validate this assumption, the cumulative relative scattering and derived count rate were measured and show similar trends over time. As

with previous studies, this indicates that the number of particles remains roughly constant over the experimental timeframe (Bergeron and Servio, 2008).

6.6.4 Modelling

The large temperature increase following turbidity indicates that the system is heat-transfer limited at early growth stages. Following the temperature plateau at roughly 400 s, the system appears to be in a steadier temperature state where heat transfer is no longer limiting. Modelling was thus performed after this plateau had been reached and used the particle size distribution at 450 s as the initial particle distribution for the model. This ensured that many variables such as temperature, bulk liquid mole fraction and solubility remained roughly constant. The overall rate constant (k) was calculated for each time step of 1 s using equation 6.5. These results were then averaged for each run and are displayed in table 6.3 . Accounting for mass transfer, table 6.3 shows the intrinsic rate constants (k_r) calculated using equation 6.6. Values calculated for the intrinsic rate constant differed by no greater than 0.5% of the value of the overall rate constant. These results indicate that the mass transfer coefficient is not significant compared to the intrinsic rate constant, and the system is reaction limited rather than mass-transfer limited at the liquid-hydrate interface.

Table 6.3 – Rate constants found at various experimental temperatures

T^{start} (K)	T^{avg} (K)	k (m/s) [$\times 10^6$]	k_r (m/s) [$\times 10^6$]
287	287.9	11.8	11.8
287	287.9	11.1	11.1
288	289.1	11.6	11.6
288	289.0	13.7	13.8
289	290.0	7.6	7.7
289	290.0	7.6	7.6

The intrinsic rate constant data show no clear trend, first increasing from runs

starting at 287 K to 288 K and then decreasing for runs starting at 289 K. There are no previous estimates for the rate constant of CO_2 semi-clathrate, but pure CO_2 clathrates systems can be used for comparison. Rate constants are generally expected to increase with temperature, as was found in a previous study spanning temperatures of 275.5 K to 279.3 K (Bergeron and Servio, 2008). However other reports found a minimum reaction rate constant at 277 K, thought to be related to the density of water (Clarke and Bishnoi, 2005; Malegaonkar *et al.*, 1997). These results demonstrate the difficulty in assessing rate constant values for clathrates, likely due to experimental uncertainties. Given that the current study does not demonstrate any strong trend in rate constant for CO_2 semi-clathrates, no attempt to estimate activation energy was undertaken. The Arrhenius relationship developed in a previous study can be extrapolated to estimate the reaction rate constant at the current experimental conditions (Bergeron and Servio, 2008). At 289 K the rate constant is predicted to be in the order of 10^{-5}, which is similar to the results found in this study. Though the systems are not the same, one would imagine comparable crystallization processes to result in similar rate constants.

6.7 Conclusion

The formation of CO_2—TBAB bromide semi-clathrates was investigated at temperatures ranging from 287.9 K to 290 K. Significant differences in reactor temperature and gas consumption were found compared to previous investigations of pure clathrate growth. The intrinsic reaction rate constant was determined at each temperature with values ranging from 7.6×10^{-6} m/s to 13.8×10^{-6} m/s. No significant trend was found between rate constants and temperature in the study.

6.8 Acknowledgements

The authors are grateful to the Natural Sciences and Engineering Research Council of Canada (NSERC), the Canada Research Chair Program (CRC) and McGill University, specifically the McGill Engineering Doctoral Award (MEDA), for financial funding and support. The authors also acknowledge the contributions of Marion Offenstein and Philippe Assaad for their help in setting up the experimental apparatus and data acquisition.

Chapter 7

Conclusion and Future Recommendations

7.1 Comprehensive Conclusion

The current work investigates gas hydrate growth under kinetic and thermodynamic promoters. Chapters 3 and 4 evaluate the effects of anionic surfactants as kinetic promoters on hydrate growth. For both of these studies, methane (CH_4) is chosen as a model gas hydrate former. Chapter 3 uses sodium dodecyl sulphate (SDS) as a model anionic surfactant. This study demonstrates that surfactants, at their promoting concentrations, do not have an appreciable effect on hydrate former thermodynamics and specifically solubility. Results further show that a large portion of surfactant hydrate promotion can be attributed to an increase in gas hydrate former mole fraction during growth. Chapter 4 expands on this study by characterizing the effects of a gemini anionic surfactant, DOWFAX 8390, along with the conventional surfactant, SDS. Similar to SDS, DOWFAX 8390 did not significantly affect system thermodynamics at concentrations promoting hydrate growth. The effect of surfactant concentration on gas hydrate growth rate is assessed and demonstrates a smooth sigmoid increase in hydrate growth rate with surfactant loading. The chap-

ter also proposes a promotion mechanism for surfactants based on their effects at the vapour-liquid and hydrate-liquid interfaces. Surfactants were thought to increase hydrate growth in two ways: first by increasing the driving force for hydrate growth by facilitating CH_4 mass transfer across the vapour-liquid interface, and second by increasing hydrate particle area due to electrostatic or steric effects of surfactants at the liquid-hydrate interface. Chapters 5 and 6 investigate thermodynamic promotion using the tetra-n-butylammonium bromide (TBAB) semi-clathrate system. When studying the thermodynamics of hydrates, solubility data is essential for both thermodynamic and kinetic modelling. Chapter 5 provides these solubility measurements for carbon dioxide (CO_2)— and CH_4—TBAB systems. These results are validated by comparing equilibrium temperature and pressure data to previous literature studies. Solubility data are then applied to study CO_2—TBAB growth in chapter 6. A kinetic model is applied based on a hydrate former bulk liquid concentration driving force. The mole fraction of CO_2 following crystal formation is found to follow a first-order response and remain roughly constant from 500 s to 1500 s after hydrate formation. Hydrate particle area is also measured using dynamic light scattering and incorporated into the kinetic model. The kinetic model is used to estimate the reaction rate constant for CO_2—TBAB semi-clathrates over the temperature range of 288 K to 290 K. Results show no apparent trend in reaction rate constant over the experimental temperature range. These results provide the first known estimate, as far as the author is aware, of the intrinsic semi-clathrate reaction rate constant, which is critical for kinetic modelling and reactor scale-up.

7.2 Future Work Recommendations

The following is a list of recommended future works:

— Further refining of the *in-situ* particle size analysis apparatus such that it can accurately detect hydrates in the range of 100 nm to 100 μm; the explicit goal of this being the improved accuracy of clathrate hydrate modelling as well as the characterization of kinetic hydrate promoters.

— Determination of the reaction rate constant of CH_4—TBAB—H_2O semi-clathrates for their potential use in hydrated natural gas storage systems.

— Investigation into the crystal structure of TBAB semi-clathrates, notably the structures with hydration numbers of 24 and 26. This could be developed further by characterizing the effect of guest compounds in the dodecahedral cages on crystal structure. This study could be undertaken using a Raman spectrometer available in the department.

— Development of a multi-component kinetic semi-clathrate model to determine the effectiveness of such a crystal structure for gas separation. Model gas mixtures should include CO_2—N_2 and CH_4—CO_2 because of their potential industrial uses.

7.3 Other Significant Contributions

In addition to the work presented in this thesis, the author has also made the following significant contributions to other works:

— Jitrwung, R.; Verrett, J. and Yargeau, V., 2013 Optimization of selected salts concentration for improved biohydrogen production from biodiesel-based glycerol using *Enterobacter aerogenes*. *Renewable Energy*, **50**: 222-226.

— Alajek, S.; Ham, A.; Heather, M. and Verrett J., 2013. Blurring the line between for-credit curricular and not-for-credit extracurricular engineering learning environments. *Proceedings of the 2013 Canadian Engineering Education Assocation (CEEA13) Conference, Montreal, Canada*, **001**: 1-5.

— Verrett, J.; Posteraro, D.; Ivall, J.; Brennan, S. and Servio, P., 2014. Understanding the Effect of Kinetic Additives on Gas Hydrate Growth. *Proceedings of the 8th International Conference on Gas Hydrates (ICGH8-2014), Beijing, China*, **T1**: 38.

— Posteraro, D.; Verrett, J.; Maric, M. and Servio, P., 2015. New insights into the effect of polyvinylpyrrolidone (PVP) concentration on methane hydrate growth. 1. Growth rate. *Chemical Engineering Science*, **126**, 99-105.

— Wei, Z.; Kowalska, E. K.; Verrett, J.; Colbeau, C.; Remita, H. and Ohtani, B., 2015. Morphology-dependent photocatalytic activity of octahedral anatase particles prepared by ultrasonication-hydrothermal reaction of titanates. *Nanoscale*, **7**: 12392-12404.

— Verrett, J.; Kietzig, A.-M. and Orjuela-Laverde, M., 2015. I flipped my tutorials: a case study of implementing active learning strategies in engineering. *Proceedings of the 2015 Canadian Engineering Education Association (CEEA15) Conference, Hamilton, Canada*, **125**: 1-5.

Chapter 8

Notation

8.1 List of symbols

$A.A.D.$ = absolute average deviation
a = volumetric fraction
b = general variable
c = concentration ($mg_{solvent}$ kg^{-1}_{solute})
c_{50} = concentration at which growth increases by half of its potential increase ($mg_{solvent}$ kg $^{-1}_{solute}$)
D = Diffusivity (m^2 s^{-1})
df = driving force
d_s = stirrer diameter
g = growth rate (mol s^{-1})
IF = interface
k = overall rate constant (m s^{-1})
k_r = intrinsic reaction rate constant (m s^{-1})
k_{H-L} = hydrate-liquid mass transfer rate (m s^{-1})
L = characteristic length (m)
MW = molar mass

m = mass (g)
N = stirring rate (s^{-1})
N_p = power number of the stirring device
n = number of moles (mol)
P = pressure (Pa)
q = number of trials
R = universal gas constant (8.314 J mol^{-1} K^{-1})
Re = Reynolds number
r = resistance
r^2 = correlation coefficient
Sc = Schmidt number
Sh = Sherwood number
s = surfactant effectiveness ($mg_{solvent}$ $kg_{solute}{}^{-1}$)
T = temperature (K)
t = time (s)
u = standard uncertainty
V = Volume (m^3)
v = molar volume (m^3 mol^{-1})
w = weight fraction
x = liquid mole fraction
y = vapour mole fraction
z = hydrate mole fraction

8.2 List of Greek letters

Δ = change in a value
ϵ = power input per mass of fluid ($m^2\ s^{-3}$)
η = moles of gas per mole of hydrate
μ_0 = zeroeth moment of particle size distribution (m^{-3})
μ_2 = second moment of particle size distribution (m^{-1})
ν = kinematic viscocity ($m^2\ s^{-1}$)
ρ = density ($g\ cm^{-3}$)
ϕ = particle density distribution (m^{-4})
π = mathematical constant (3.14159)
σ = standard deviation
τ = time constant (s)

8.3 List of subscripts and superscripts

8.3.1 Superscripts

avg = average
eqm = equilibrium
exp = experimental
$H - L$ = hydrate-liquid equilibrium
$H - L - V$ = hydrate-liquid-vapour equilibrium
ind = induction
l = bulk liquid
rel = relative
v = bulk vapour

8.3.2 Subscripts

0 = initial
g = guest
H = hydrate
i = gas hydrate former
o = overall
L = liquid
p = particle
s = surfactant
SDS = sodium dodecyl sulphate
$TBAB$ = tetra-n-butylammonium bromide
tb = turbidity
V = vapour
w = water

Chapter 9

Bibliography

Aaron, D. and Tsouris, C., 2005. Separation of CO2 from flue gas: a review. *Separation Science and Technology*, **40**: 321–348.

Aladko, L.S.; Dyadin, Y.A.; Rodionova, T.V. and Terekhova, I.S., 2002. Clathrate hydrates of tetrabutylammonium and tetraisoamylammonium halides. *Journal of Structural Chemistry*, **43**: 990–994.

Arjmandi, M.; Chapoy, A. and Tohidi, B., 2007. Equilibrium Data of Hydrogen, Methane, Nitrogen, Carbon Dioxide, and Natural Gas in Semi-Clathrate Hydrates of Tetrabutyl Ammonium Bromide. *Journal of Chemical & Engineering Data*, **52**: 2153–2158.

Armenante, P.M. and Kirwan, D.J., 1989. Mass transfer to microparticles in agitated systems. *Chemical Engineering Science*, **44**: 2781–2796.

Baldi, G.; Conti, R. and Alaria, E., 1978. Complete suspension of particles in mechanically agitated vessels. *Chemical Engineering Science*, **33**: 21–25.

Bergeron, S.; Beltran, J.G. and Servio, P., 2009. Reaction rate constant of methane clathrate formation. *Fuel*, **89**: 294–301.

Bergeron, S. and Servio, P., 2008. Reaction rate constant of CO2 hydrate formation and verification of old premises pertaining to hydrate growth kinetics. *AIChE Journal*, **54**: 2964–2970.

Bergeron, S. and Servio, P., 2009. CO2 and CH4 mole fraction measurements during hydrate growth in a semi-batch stirred tank reactor and its significance to kinetic modeling. *Fluid Phase Equilibria*, **276**: 150–155.

Bonnefoy, O.; Gruy, F. and Herri, J.M., 2005. *A priori* calculation of the refractive index of some simple gas hydrates of structures I and II. *Materials Chemistry and Physics*, **89**: 336–344.

Boswell, R. and Collett, T.S., 2011. Current perspectives on gas hydrate resources. *Energy & Environmental Science*, **4**: 1206–1215.

Bruusgaard, H.; Beltran, J.G. and Servio, P., 2010. Solubility measurements for the CH4 + CO2 + H2O system under hydrate-liquid-vapor equilibrium. *Fluid Phase Equilibria*, **296**: 106–109.

Callister, W.D. and Rethwisch, D.G., 2007. *Materials science and engineering: an introduction*, volume 7. Wiley, New York, NY.

Chapman, W.G.; Gubbins, K.E.; Jackson, G. and Radosz, M., 1989. SAFT: Equation-of-state solution model for associating fluids. *Fluid Phase Equilibria*, **52**: 31–38.

Chase, M.W.; Davies, C.A.; Downey, J.R.; Frurip, D.J.; McDonald, R.A. and Syverud, A.N., 1985. *NIST-JANAF thermochemical tables*. National Institute of Standards and Technology, Gaithersburg, MD.

Clain, P.; Delahaye, A.; Fournaison, L.; Mayoufi, N.; Dalmazzone, D. and Fürst, W., 2012. Rheological properties of tetra-n-butylphosphonium bromide hydrate slurry flow. *Chemical Engineering Journal*, **193**: 112–122.

Clarke, M.A. and Bishnoi, P.R., 2005. Determination of the intrinsic kinetics of CO2 gas hydrate formation using *in situ* particle size analysis. *Chemical Engineering Science*, **60**: 695–709.

Cotton, F.A.; Wilkinson, G. and Gaus, P.L., 1976. *Basic inorganic chemistry*. Wiley, New York, NY.

Davidson, D., 1973. *Water, a comprehensive treatise*, volume 2. Plenum Press, New York, NY.

Davy, H., 1811. On a combination of oxymuriatic gas and oxygene gas. *Philosophical Transactions of the Royal Society of London*, **101**: 155–162.

Deen, W.M., 1998. *Analysis of transport phenomena*. Topics in Chemical Engineering. Oxford University Press, New York, NY.

Del, V.L. and Kelland, M.A., 2009. Tetrahydrofuran hydrate crystal growth inhibition by hyperbranched poly(ester amide)s. *Chemical Engineering Science*, **64**: 3197–3200.

Deschamps, J. and Dalmazzone, D., 2009. Dissociation enthalpies and phase equilibrium for TBAB semi-clathrate hydrates of N2, CO2, N2 + CO2 and CH4 + CO2. *Journal of Thermal Analysis and Calorimetry*, **98**: 113–118.

Di Profio, P.; Arca, S.; Germani, R. and Savelli, G., 2005. Surfactant promoting effects on clathrate hydrate formation: Are micelles really involved? *Chemical Engineering Science*, **60**: 4141–4145.

Di Profio, P.; Arca, S.; Germani, R. and Savelli, G., 2007. Novel nanostructured media for gas storage and transport: clathrate hydrates of methane and hydrogen. *Journal of Fuel Cell Science and Technology*, **4**: 49–55.

Englezos, P.; Kalogerakis, N.; Dholabhai, P.D. and Bishnoi, P.R., 1987a. Kinetics of formation of methane and ethane gas hydrates. *Chemical Engineering Science*, **42**: 2647–2658.

Englezos, P.; Kalogerakis, N.; Dholabhai, P.D. and Bishnoi, P.R., 1987b. Kinetics of gas hydrate formation from mixtures of methane and ethane. *Chemical Engineering Science*, **42**: 2659–2666.

Englezos, P., 1993. Clathrate hydrates. *Industrial & Engineering Chemistry Research*, **32**: 1251–1274.

Eslamimanesh, A.; Mohammadi, A.H.; Richon, D.; Naidoo, P. and Ramjugernath, D., 2012. Application of gas hydrate formation in separation processes: A review of experimental studies. *Journal of Chemical Thermodynamics*, **46**: 62–71.

Fisicaro, E.; Compari, C.; Rooycka-Roszak, B.; Viscardi, G. and Quagliotto, P.L., 1997. Chemico-physical and biological properties of gemini surfactants. *Current Opinion in Colloid & Interface Science*, **2**: 53–68.

Fowler, D.L.; Loebenstein, W.V.; Pall, D.B. and Kraus, C.A., 1940. Some Unusual Hydrates of Quaternary Ammonium Salts. *Journal of the American Chemical Society*, **62**: 1140–1142.

Frost, E.M.J. and Deaton, W.M., 1946. Gas hydrate composition and equilibrium data. *Oil & Gas Journal*, **45**: 170–178.

Gaponenko, L.A.; Solodovnikov, S.F.; Dyadin, Y.A.; Aladko, L.S. and Polyanskaya, T.M., 1984. Crystallographic study of tetra-n-butylammonium bromide polyhydrates. *Journal of Structural Chemistry*, **25**: 157–159.

Gholinezhad, J.; Chapoy, A. and Tohidi, B., 2011. Thermodynamic Stability and Self-Preservation Properties of Semi-Clathrates in the Methane+Tetra-n- Butyl Ammonium Bromide+Water System. In *Proceedings of 7th International Conference on Gas Hydrates, Edinburgh, U.K.* pp. 17–21.

Glew, D. and Haggett, M., 1968a. Kinetics of formation of ethylene oxide hydrate. Part I. Experimental method and congruent solutions. *Canadian Journal of Chemistry*, **46**: 3857–3865.

Glew, D. and Haggett, M., 1968b. Kinetics of formation of ethylene oxide hydrate. Part II. Incongruent solutions and discussion. *Canadian Journal of Chemistry*, **46**: 3867–3877.

Gudmundsson, J.S. and Borrehaug, A., 1996. Frozen hydrate for transport of natural gas. In *Proceedings of 2nd International Conference on Gas Hydrate, Toulouse, France*. pp. 415–422.

Gudmundsson, J.S.; Parlaktuna, M. and Khokhar, A.A., 1994. Storage of natural gas as frozen hydrate. *SPE Production & Facilities*, **9**: 69–73.

Hammerschmidt, E.G., 1934. Formation of Gas Hydrates in Natural Gas Transmission Lines. *Journal of Industrial and Engineering Chemistry*, **26**: 851–855.

Hayduk, W. and Laudie, H., 1974. Prediction of diffusion coefficients for nonelectrolytes in dilute aqueous solutions. *AIChE Journal*, **20**: 611–615.

Heneghan, A.; Wilson, P.; Wang, G. and Haymet, A., 2001. Liquid-to-crystal nucleation: Automated lag-time apparatus to study supercooled liquids. *The Journal of Chemical Physics*, **115**: 7599–7608.

Herri, J.M.; Pic, J.S.; Gruy, F. and Cournil, M., 1999. Methane hydrate crystallization mechanism from *in-situ* particle sizing. *AIChE Journal*, **45**: 590–602.

Holder, G.; Corbin, G. and Papadopoulos, K., 1980. Thermodynamic and molecular properties of gas hydrates from mixtures containing methane, argon, and krypton. *Industrial & Engineering Chemistry Fundamentals*, **19**: 282–286.

Jeffrey, G. and McMullan, R., 2007. The clathrate hydrates. *Progress in Inorganic Chemistry*, **8**: 43–108.

Jerbi, S.; Delahaye, A.; Oignet, J.; Fournaison, L. and Haberschill, P., 2013. Rheological properties of CO2 hydrate slurry produced in a stirred tank reactor and a secondary refrigeration loop. *International Journal of Refrigeration*, **36**: 1294–1301.

Kalogerakis, N.; Jamaluddin, A.K.M.; Dholabhai, P.D. and Bishnoi, P.R., 1993. Effect of surfactants on hydrate formation kinetics. In *SPE International Symposium on Oilfield Chemistry, New Orleans, Louisiana*. Society of Petroleum Engineers, pp. 375–384.

Kane, S.G.; Evans, T.W.; Brian, P.L.T. and Sarofim, A.F., 1974. Determination of the kinetics of secondary nucleation in batch crystallizers. *AIChE Journal*, **20**: 855–862.

Kang, S.P.; Lee, H.; Lee, C.S. and Sung, W.M., 2001. Hydrate phase equilibria of the guest mixtures containing CO_2, N_2 and tetrahydrofuran. *Fluid Phase Equilibria*, **185**: 101–109.

Karaaslan, U. and Parlaktuna, M., 2000a. Effect of surfactants on hydrate formation rate. *Annals of the New York Academy of Sciences*, **912**: 735–743.

Karaaslan, U. and Parlaktuna, M., 2000b. Surfactants as Hydrate Promoters? *Energy & Fuels*, **14**: 1103–1107.

Kashchiev, D. and Firoozabadi, A., 2002. Nucleation of gas hydrates. *Journal of Crystal Growth*, **243**: 476–489.

Katz, D.L., 1971. Depths to which frozen gas fields (gas hydrates) may be expected. *Journal of Petroleum Technology*, **23**: 419–423.

Kelland, M.A., 2006. History of the development of low dosage hydrate inhibitors. *Energy & Fuels*, **20**: 825–847.

Kumar, A.; Sakpal, T.; Linga, P. and Kumar, R., 2013. Influence of contact medium and surfactants on carbon dioxide clathrate hydrate kinetics. *Fuel*, **105**: 664–671.

Kutergin, O.B.; Mel'nikov, V.P. and Nesterov, A.N., 1992. Effect of surfactants on the mechanism and kinetics of the formation of gas hydrates. *Doklady Akademii Nauk*, **323**: 549–553.

Kwon, Y.A.; Park, J.M.; Jeong, K.E.; Kim, C.U.; Kim, T.W.; Chae, H.J.; Jeong, S.Y.; Yim, J.H.; Park, Y.K. and Lee, J.D., 2011. Synthesis of anionic multichain type surfactant and its effect on methane gas hydrate formation. *Journal of Industrial and Engineering Chemistry*, **17**: 120–124.

Li, D.L.; Du, J.W.; Fan, S.S.; Liang, D.Q.; Li, X.S. and Huang, N.S., 2007. Clathrate Dissociation Conditions for Methane + Tetra-n-butyl Ammonium Bromide (TBAB) + Water. *Journal of Chemical & Engineering Data*, **52**: 1916–1918.

Lin, W.; Delahaye, A. and Fournaison, L., 2008. Phase equilibrium and dissociation enthalpy for semi-clathrate hydrate of CO2 + TBAB. *Fluid Phase Equilibria*, **264**: 220–227.

Lin, W.; Dalmazzone, D.; Fürst, W.; Delahaye, A.; Fournaison, L. and Clain, P., 2013. Thermodynamic studies of CO2 + TBAB + Water system: experimental measurements and correlations. *Journal of Chemical & Engineering Data*, **58**: 2233–2239.

Linga, P.; Adeyemo, A. and Englezos, P., 2008. Medium-pressure clathrate hydrate/membrane hybrid process for postcombustion capture of carbon dioxide. *Environmental Science & Technology*, **42**: 315–320.

Lipkowski, J.; Komarov, V.Y.; Rodionova, T.V.; Dyadin, Y.A. and Aladko, L.S., 2002. The structure of tetrabutylammonium bromide hydrate (C4H9)4NBr21/3H2O. *Journal of Supramolecular Chemistry*, **2**: 435–439.

Lirio, C.F.D.S.; Pessoa, F.L.P. and Uller, A.M.C., 2013. Storage capacity of carbon dioxide hydrates in the presence of sodium dodecyl sulfate (SDS) and tetrahydrofuran (THF). *Chemical Engineering Science*, **96**: 118–123.

Lo, C.; Zhang, J.S.; Couzis, A.; Somasundaran, P. and Lee, J.W., 2010. Adsorption of cationic and anionic surfactants on cyclopentane hydrates. *Journal of Physical Chemistry C*, **114**: 13385–13389.

Long, J. and Sloan, E., 1996. Hydrates in the ocean and evidence for the location of hydrate formation. *International Journal of Thermophysics*, **17**: 1–13.

Ma, Z.W.; Zhang, P.; Wang, R.Z.; Furui, S. and Xi, G.N., 2010. Forced flow and convective melting heat transfer of clathrate hydrate slurry in tubes. *International Journal of Heat and Mass Transfer*, **53**: 3745–3757.

Mak, T.C. and McMullan, R.K., 1965. Polyhedral clathrate hydrates. X. Structure of the double hydrate of tetrahydrofuran and hydrogen sulfide. *The Journal of Chemical Physics*, **42**: 2732–2737.

Makogon, Y.F., 1974. *Hydrates of natural gas*. PennWell Books, Tulsa, Oklahoma, in Russian (1981 in English).

Makogon, Y.F., 1965. Hydrate formation in the gas-bearing beds under permafrost conditions. *Gazovaia Promyshlennost*, **5**: 14–15.

Malegaonkar, M.B.; Dholabhai, P.D. and Bishnoi, P.R., 1997. Kinetics of carbon dioxide and methane hydrate formation. *The Canadian Journal of Chemical Engineering*, **75**: 1090–1099.

Marinhas, S.; Delahaye, A.; Fournaison, L.; Dalmazzone, D.; Fürst, W. and Petitet, J.P., 2006. Modelling of the available latent heat of a CO2 hydrate slurry in an experimental loop applied to secondary refrigeration. *Chemical Engineering and Processing: Process Intensification*, **45**: 184–192.

May, E.F.; Wu, R.; Kelland, M.A.; Aman, Z.M.; Kozielski, K.A.; Hartley, P.G. and Maeda, N., 2014. Quantitative kinetic inhibitor comparisons and memory effect measurements from hydrate formation probability distributions. *Chemical Engineering Science*, **107**: 1–12.

Mayoufi, N.; Dalmazzone, D.; Fürst, W.; Delahaye, A. and Fournaison, L., 2010. CO2 Enclathration in Hydrates of Peralkyl-(Ammonium/Phosphonium) Salts: Stability Conditions and Dissociation Enthalpies. *Journal of Chemical & Engineering Data*, **55**: 1271–1275.

McMullan, R. and Jeffrey, G.A., 1959. Hydrates of the tetra n-butyl and tetra i-amyl quaternary ammonium salts. *The Journal of Chemical Physics*, **31**: 1231–1234.

McMullan, R.K. and Jeffrey, G., 1965. Polyhedral clathrate hydrates. IX. Structure of ethylene oxide hydrate. *The Journal of Chemical Physics*, **42**: 2725–2732.

Mel'nikov, V.P.; Nesterov, A.N. and Feklistov, V.V., 1998. Hydration formation of gases in the presence of surfactant additives. *Khimiya v Interesakh Ustoichivogo Razvitiya*, **6**: 97–102.

Mimachi, H.; Takahashi, M.; Takeya, S.; Gotoh, Y.; Yoneyama, A.; Hyodo, K.; Takeda, T. and Murayama, T., 2015. Effect of Long-Term Storage and Thermal History on the Gas Content of Natural Gas Hydrate Pellets under Ambient Pressure. *Energy & Fuels*, **29**: 4827–4834.

Mitarai, M.; Kishimoto, M.; Suh, D. and Ohmura, R., 2015. Surfactant Effects on the Crystal Growth of Clathrate Hydrate at the Interface of Water and Hydrophobic-Guest Liquid. *Crystal Growth & Design*, **15**: 812–821.

Mohammadi, A.H.; Eslamimanesh, A.; Belandria, V. and Richon, D., 2011. Phase equilibria of semiclathrate hydrates of CO_2, N_2, CH_4, or H_2 + Tetra-n-butylammonium bromide aqueous solution. *Journal of Chemical & Engineering Data*, **56**: 3855–3865.

Montgomery, D.C. and Runger, G.C., 2007. *Applied Statistics and Probability for Engineers, fourth edition*. Wiley, Hoboken, NJ.

Mullin, J., 1997. *Crystallization*. Butterworth-Heinemann, Oxford, U. K., 3rd edition.

Muromachi, S.; Ohmura, R.; Takeya, S. and Mori, Y.H., 2010. Clathrate hydrates for ozone preservation. *The Journal of Physical Chemistry B*, **114**: 11430–11435.

Ogoshi, H. and Takao, S., 2004. Air-conditioning system using clathrate hydrate slurry. *JFE Technical Report*, **3**: 1–5.

Okutani, K.; Kuwabara, Y. and Mori, Y.H., 2008. Surfactant effects on hydrate formation in an unstirred gas/liquid system: An experimental study using methane and sodium alkyl sulfates. *Chemical Engineering Science*, **63**: 183–194.

Oyama, H.; Shimada, W.; Ebinuma, T.; Kamata, Y.; Takeya, S.; Uchida, T.; Nagao, J. and Narita, H., 2005. Phase diagram, latent heat, and specific heat of TBAB semiclathrate hydrate crystals. *Fluid Phase Equilibria*, **234**: 131–135.

Park, K.n.; Hong, S.Y.; Lee, J.W.; Kang, K.C.; Lee, Y.C.; Ha, M.G. and Lee, J.D., 2011. A new apparatus for seawater desalination by gas hydrate process and removal characteristics of dissolved minerals (Na^+, Mg^{2+}, Ca^{2+}, K^+, B^{3+}). *Desalination*, **274**: 91–96.

Park, S.; Lee, S.; Lee, Y. and Seo, Y., 2013. CO2 capture from simulated fuel gas mixtures using semiclathrate hydrates formed by quaternary ammonium salts. *Environmental Science & Technology*, **47**: 7571–7577.

Pasieka, J.; Coulombe, S. and Servio, P., 2014. The effect of hydrophilic and hydrophobic multi-wall carbon nanotubes on methane dissolution rates in water at three phase equilibrium (V-L_w-H) conditions. *Industrial & Engineering Chemistry Research*, **53**: 14519–14525.

Peng, D.Y. and Robinson, D.B., 1976. A new two-constant equation of state. *Industrial & Engineering Chemistry Fundamentals*, **15**: 59–64.

Perrin, A.; Musa, O.M. and Steed, J.W., 2013. The chemistry of low dosage clathrate hydrate inhibitors. *Chemical Society Reviews*, **42**: 1996–2015.

Priestley, J., 1780. Versuche und Beobachtungen über Verrshiedene Gattungen der Luft. *Wien Leipzig*, **3**: 359–362.

Renault-Crispo, J.S.; Lang, F. and Servio, P., 2014. The importance of liquid phase compositions in gas hydrate modeling: Carbon dioxide-methane-water case study. *Journal of Chemical Thermodynamics*, **68**: 153–160.

Renon, H. and Prausnitz, J.M., 1968. Local compositions in thermodynamic excess functions for liquid mixtures. *AIChE Journal*, **14**: 135–144.

Ribeiro Jr., C.P. and Lage, P.L.C., 2008. Modelling of hydrate formation kinetics: state-of-the-art and future directions. *Chemical Engineering Science*, **63**: 2007–2034.

Ricaurte, M.; Dicharry, C.; Broseta, D.; Renaud, X. and Torré, J.P., 2013. CO2 removal from a CO2-CH4 gas mixture by clathrate hydrate formation using THF and SDS as water-soluble hydrate promoters. *Industrial & Engineering Chemistry Research*, **52**: 899–910.

Ripmeester, J.A.; John, S.T.; Ratcliffe, C.I. and Powell, B.M., 1987. A new clathrate hydrate structure. *Nature*, **325**: 135–136.

Rogers, R.E. and Zhong, Y., 2000. Feasibility of storing natural gas in hydrates commercially. *Annals of the New York Academy of Sciences*, **912**: 843–850.

Sekhon, B.S., 2004. Gemini (dimeric) surfactants: The two-faced molecules. *Resonance*, **9**: 42–49.

Servio, P. and Englezos, P., 2002. Measurement of dissolved methane in water in equilibrium with its hydrate. *Journal of Chemical & Engineering Data*, **47**: 87–90.

Shimada, W.; Shiro, M.; Kondo, H.; Takeya, S.; Oyama, H.; Ebinuma, T. and Narita, H., 2005. Tetra-n-butylammonium bromide-water (1/38). *Acta Crystallographica. Section C, Crystal Structure Communications*, **61**: o65–66.

Skovborg, P. and Rasmussen, P., 1994. A mass transport limited model for the growth of methane and ethane gas hydrates. *Chemical Engineering Science*, **49**: 1131–1143.

Sloan, E.D., 2003. Fundamental principles and applications of natural gas hydrates. *Nature*, **426**: 353–363.

Sloan, E.D. and Koh, C.A., 2008. *Clathrate hydrates of natural gases*. CRC Press, Boca Raton, FL.

Sloan, E.D.; Koh, C.A. and Sum, A., 2010. *Natural gas hydrates in flow assurance*. Gulf Professional Publishing, Houston, TX.

Span, R. and Wagner, W., 1996. A new equation of state for carbon dioxide covering the fluid region from the triple-point temperature to 1100 K at pressures up to 800 MPa. *Journal of Physical and Chemical Reference Data*, **25**: 1509–1596.

Suess, E.; Bohrmann, G.; Greinert, J. and Lausch, E., 1999. Flammable ice. *Scientific American*, **281**: 76–83.

Sun, Z.G. and Sun, L., 2010. Equilibrium conditions of semi-clathrate hydrate dissociation for methane + tetra-n-butyl ammonium bromide. *Journal of Chemical & Engineering Data*, **55**: 3538–3541.

Sun, Z.; Wang, R.; Ma, R.; Guo, K. and Fan, S., 2003. Effect of surfactants and liquid hydrocarbons on gas hydrate formation rate and storage capacity. *International Journal of Energy Research*, **27**: 747–756.

Taylor, C.J.; Dieker, L.E.; Miller, K.T.; Koh, C.A. and Sloan, E.D., 2007. Micromechanical adhesion force measurements between tetrahydrofuran hydrate particles. *Journal of Colloid and Interface Science*, **306**: 255–261.

Torré, J.P.; Ricaurte, M.; Dicharry, C. and Broseta, D., 2012. CO2 enclathration in the presence of water-soluble hydrate promoters: Hydrate phase equilibria and kinetic studies in quiescent conditions. *Chemical Engineering Science*, **82**: 1–13.

Trebble, M.A. and Bishnoi, P.R., 1987. Development of a new four-parameter cubic equation of state. *Fluid Phase Equilibria*, **35**: 1–18.

Trueba, A.T.; Radović, I.R.; Zevenbergen, J.F.; Kroon, M.C. and Peters, C.J., 2012. Kinetics measurements and *in situ* Raman spectroscopy of formation of hydrogen-

tetrabutylammonium bromide semi-hydrates. *International Journal of Hydrogen Energy*, **37**: 5790–5797.

Tulk, C.; Ripmeester, J. and Klug, D., 2000. The application of Raman spectroscopy to the study of gas hydrates. *Annals of the New York Academy of Sciences*, **912**: 859–872.

Tyagi, P. and Tyagi, R., 2009. Synthesis, structural properties and applications of gemini surfactants: a review. *Tenside Surfactants Detergents Journal*, **46**: 373–382.

Van der Waals, J. and Platteeuw, J., 1959. Clathrate solutions. *Advances in Chemical Physics*, **2**: 1–57.

Verrett, J.; Posteraro, D. and Servio, P., 2012. Surfactant effects on methane solubility and mole fraction during hydrate growth. *Chemical Engineering Science*, **84**: 80–84.

Verrett, J.; Renault-Crispo, J.S. and Servio, P., 2015. Phase equilibria, solubility and modeling study of CO2/CH4 + tetra-n-butylammonium bromide aqueous semi-clathrate systems. *Fluid Phase Equilibria*, **388**: 160–168.

Vysniauskas, A. and Bishnoi, P.R., 1983. A kinetic study of methane hydrate formation. *Chemical Engineering Science*, **38**: 1061–1072.

Warren, S.G. and Brandt, R.E., 2008. Optical constants of ice from the ultraviolet to the microwave: A revised compilation. *Journal of Geophysical Research: Atmospheres*, **113**: D14220.

Watanabe, K.; Niwa, S. and Mori, Y.H., 2005. Surface tensions of aqueous solutions of sodium alkyl sulfates in contact with methane under hydrate-forming conditions. *Journal of Chemical & Engineering Data*, **50**: 1672–1676.

Wilke, C.R. and Chang, P., 1955. Correlation of diffusion coefficients in dilute solutions. *AIChE Journal*, **1**: 264–270.

Wilson, P. and Haymet, A., 2010. Hydrate formation and re-formation in nucleating THF/water mixtures show no evidence to support a "memory" effect. *Chemical Engineering Journal*, **161**: 146–150.

Yang, J. and Tohidi, B., 2011. Characterization of inhibition mechanisms of kinetic hydrate inhibitors using ultrasonic test technique. *Chemical Engineering Science*, **66**: 278–283.

Ye, N. and Zhang, P., 2012. Equilibrium data and morphology of tetra-n-butyl ammonium bromide semiclathrate hydrate with carbon dioxide. *Journal of Chemical and Engineering Data*, **57**: 1557–1562.

Zana, R. and Xia, J., 2004. *Gemini surfactants: Synthesis, interfacial and solution-phase behavior, and applications*. Surfactant Science Series. Marcel Decker, Inc., New York, NY.

Zhang, B. and Wu, Q., 2010. Thermodynamic promotion of tetrahydrofuran on methane separation from low-concentration coal mine methane based on hydrate. *Energy & Fuels*, **24**: 2530–2535.

Zhang, J.S.; Lee, S. and Lee, J.W., 2007. Does SDS micellize under methane hydrate-forming conditions below the normal Krafft point? *Journal of Colloid and Interface Science*, **315**: 313–318.

Zhang, J.S.; Lo, C.; Somasundaran, P. and Lee, J.W., 2010. Competitive adsorption between SDS and carbonate on tetrahydrofuran hydrates. *Journal of Colloid and Interface Science*, **341**: 286–288.

Zhang, J.S.; Lo, C.; Somasundaran, P.; Lu, S.; Couzis, A. and Lee, J.W., 2008. Adsorption of sodium dodecyl sulfate at THF hydrate/liquid interface. *Journal of Physical Chemistry C*, **112**: 12381–12385.

Zhong, D.L.; Ding, K.; Yan, J.; Yang, C. and Sun, D.J., 2013. Influence of cyclopentane and SDS on methane separation from coal mine gas by hydrate crystallization. *Energy and Fuels*, **27**: 7252–7258.

Zhong, Y. and Rogers, R.E., 2000. Surfactant effects on gas hydrate formation. *Chemical Engineering Science*, **55**: 4175–4187.